Imperial College London

Ultrafast Multi-Pulse Spectroscopy of Hot Carrier Dynamics in Lead Halide Perovskites

Ben Peter Carwithen

Department of Chemistry

Faculty of Natural Sciences

Submitted for the degree of Doctor of Philosophy

October 2023

Declaration

I hereby declare that the contents of this thesis are my own work, except where specific reference is made to the contribution of work by others. This thesis has not been submitted in whole or in part for consideration for any other degree or qualification at this, or any other university.

The copyright of this thesis rests with the author. Unless otherwise indicated, its contents are licensed under a Creative Commons Attribution-Non Commercial 4.0 International Licence (CC BY-NC). Under this licence, you may copy and redistribute the material in any medium or format. You may also create and distribute modified versions of the work. This is on the condition that: you credit the author and do not use it, or any derivative works, for a commercial purpose. When reusing or sharing this work, ensure you make the licence terms clear to others by naming the licence and linking to the licence text. Where a work has been adapted, you should indicate that the work has been changed and describe those changes. Please seek permission from the copyright holder for uses of this work that are not included in this licence or permitted under UK Copyright Law.

Ben Peter Carwithen

Acknowledgements

Firstly, I would like to give enormous thanks to my supervisor, **Dr. Artem Bakulin**, for presenting me this opportunity. In my interview all those years ago, I remember discussing "singlet fission in perovskites" and accidentally ending the video call before saying goodbye... For some reason, you hired me anyway and I'm incredibly grateful that you did. Since then, your guidance and patience has led to my transformation from chemist to spectroscopist. I am sad to be leaving just as the next chapter for your group begins, but I look forward to the beautiful work that is undoubtedly coming soon.

I would like to thank the **Department of Chemistry** for awarding me a **UKRI Scholarship**. As a result, I have been lucky enough to embark on this journey with the other members of the **Ultrafast Optoelectronics Group**:

Tom, thank you for guiding me through the first portion of my PhD. It was a blessing to be taught by someone so knowledgeable in the dark arts of spectroscopy; and a curse to think I wouldn't be able to live up to the precedent you set. Unfortunately for me, I was right.

Neath, I opted to include you here despite my omission in your own thesis, because I'm not bitter... at all, honestly. Thank you for granting me my first PhD project – 3D printing the device holder for your Viper experiments. Ich wünsche dir alles gute in Deutschland!

Yifan, thank you for patiently repeating TCSPC explanations during my early days, and bringing a positive atmosphere wherever you went. It was nice to see you again at HOPV recently, which is apt considering I got the bursary by name-dropping you!

Rhea, thank you for always being on hand to reminisce about Bristol. I'm so happy I followed you to Imperial, and I'm sorry for not fulfilling the prophecy by moving to Italy with you. At least I'm also going somewhere sunny – I hope that counts!

Polly, thank you for your patient ear and kind words during a particularly turbulent period of my life. The office was never the same after you left (the second time), and not just because I had further to walk when I ran out of migraine tablets.

Alice, thank you for bringing so much cheer to the office, though I could have lived without your disapproval of my haircuts. I hope someday I am able to match your enthusiasm for life.

Jiaxin, thank you for infecting everyone in the office with bouts of laughter, and for often being so complimentary (unlike Alice!) about my fashion choices.

Shawn, thank you for your wizardry with the THz setup. Never again will I lower myself to working out the delay stage time-zero position by hand.

Marios, thank you for being the best office neighbour I could have asked for. Your unfazed and pragmatic approach to life and the lab was a constant source of reassurance. Thank you for indulging my monologues about Argyle – I'm so proud we've gained another fan!

Dima, thank you for bringing in the perovskite single crystals so that we could actually do something useful with the THz setup. That said, I'll never be able to listen to the Bee Gees again without thinking about the Linkam stage.

Haoqing, thank you for bringing your kind heart and soul to the group (and that's not just the singing!). You have always used your knowledge so generously to help others, so I'm very glad the nanojunctions finally worked out for you. Most of all, thank you for the GPU!

Tong, sorry for stealing your phone charger so often, and thank you for asking Santa to bring me one so that I stopped.

Ziyuan, thank you for providing the final piece of the puzzle in the hot carrier confinement project, and for always indulging my silly behaviour with seemingly heartfelt laughter.

Navendu, I feel you joined us at a particularly vital part of my PhD. Thank you for sharing a small portion of your unparalleled wisdom on nanomaterials; and being a calm, reassuring presence for me and everyone else in the group.

Ziming, thank you for the insightful discussions around my results. While I wasn't fortunate enough to work with you directly, I know those who did benefited immensely.

Beier, while we only crossed paths towards the end, it is very clear that the future of the group

is in safe hands. Have fun in the new lab!

I would also like to thank the project students I have supervised, **Anna**, **Hari** and **Rozana**, for their assistance and enduring my botched explanations. Thank you to **Li** and **Pabitra** for expertly guiding the operation of the wet labs; and to the admin teams, particularly **Mike** and **Doris**, who made sure the department ran smoothly.

I would like to extend my gratitude to the many collaborators who have supplied materials for my experiments, particularly **Dr. Franziska Krieg**, **Dr. Federico Montanarella**, **Dr. Maryna Bodnarchuk** and **Prof. Maksym Kovalenko** (ETH Zürich); **Dr. Martin Kroll**, **Prof. Yana Vaynzof** and **Prof. Karl Leo** (TU Dresden); **Dr. Junzhi Ye** and **Prof. Robert Hoye** (University of Cambridge); and **Dr. Vladimir Bruevich** (Rutgers University). I thank **Dr. Jarvist Frost** for his theoretical insights and interesting discussions; as well as members of the **Durrant group** and the wider **Centre for Processable Electronics** for providing such a stimulating research environment.

I could not have made it through this time without the support of my friends and family. To **Tom** and **Dec**, thank you for the endless laughs, love and leftovers... *et al*! I couldn't have asked for better (flat)mates to have shared my time in London with – on the short list of things I'm not looking forward to about this all being done is that, for a while at least, that won't be the case. Thank you to **Lewis**, **Emma**, **Kate**, **Rose**, the '**Bristol lot**' and '**Treen Team**' for their constant reminders that life is there to be enjoyed; to **Hannah**, **Felix**, **Colin** and **Matt** for brightening up MSRH, GTA days, and several of the finest pubs in Shepherd's Bush. And to **Emily**, thank you for everything and more.

To my sister, **Emma**, congratulations for everything you've achieved so far. I only wish I'd had a teacher like you in Year 3. To **Nan** and **Grandad**, I still remember you teaching me my first 'big word' (*consume*!) during a game of Scrabble while babysitting. Since then, I've learned a few more big words, most of which are in this thesis. And, finally, **Mum** and **Dad**, to whom I owe the most. You've never forced me to follow any particular path, only asking that I work hard and not get into too much trouble (a few of my schoolteachers might say I should have listened harder to the latter), but I hope you're happy with where I've ended up. That said, I definitely should have stayed in goal.

Abstract

Efficient and low-cost solutions to green energy production are vital to alleviate the damaging effects of climate change. To this end, lead halide perovskites have recently been highlighted as a novel class of materials with remarkable optoelectronic properties arising from relatively simple and cheap synthesis routes. In order to further optimise perovskite-based devices, a better understanding of their underlying photophysics is required.

Herein, the intraband relaxation of above-gap charge-carriers ("hot carrier cooling") is used as a probe of the fundamental interactions operating in bulk and nanoscale perovskites. This is achieved by employing a novel ultrafast optical approach, "pump-push-probe" spectroscopy, to isolate carrier cooling from the various other dynamics occurring on similar timescales, and separate cooling pathways mediated by carrier, phonon and trap scattering.

A long-standing debate exists over the effect of quantum confinement on hot carrier dynamics in low-dimensional perovskites. The results herein, obtained via a near-infrared probe, reveal the significant role of carrier-carrier scattering, which becomes increasingly dominant with greater excitonic character of the excited state. The defect tolerance of perovskite nanocrystals is then extended to its effect on hot carrier dynamics using a visible light probe. Here, it is shown that hot carriers are not impervious to trap states in bromide-based systems, but retain this beneficial property in their iodide analogues. Finally, hot carrier mobility in a bulk perovskite single-crystal is assessed via a terahertz probe. It is shown that the response is dominated by localised lattice heating, which suppresses carrier mobility for a time period after intraband relaxation has occurred.

The presented research clarifies the spectroscopic response of an important and broadly studied material class across a wide range of the electromagnetic spectrum. This will contribute to the rational design of next-generation optoelectronic devices, while aiding interpretation of overlapping photophysical processes that are otherwise difficult to disentangle.

Contents

Abstract viii

List of Publications xii

List of Figures xiii

List of Tables xv

Nomenclature xvi

1 Introduction 1

1.1 Solar energy 1

1.2 Perovskites 3

1.3 Nanomaterials 5

1.4 Ultrafast spectroscopy 8

1.5 Aims and motivations for the thesis 10

2 Perovskite photophysics – from the ground, up 12

2.1 Electronic structure of solids 12

2.2 Light absorption 15

2.3 Thermalisation and hot carrier cooling 17

2.4 Recombination 21

2.5 Defects and trapping 22

3 Methods 25

3.1 Basic principles of a laser 25

3.2 Steady-state methods 28

3.2.1 Ultraviolet-visible absorption spectroscopy . . . 28
3.2.2 Photoluminescence spectroscopy . . . 29
3.3 Pump-push-probe (PPP) spectroscopy . . . 30
3.3.1 Pump–push–NIR-probe (PPP-NIR) spectroscopy . . . 33
3.3.2 Pump–push–Visible-probe (PPP-Vis) spectroscopy . . . 34
3.3.3 Pump–push–THz-probe (PPP-THz) spectroscopy . . . 36
3.4 Kinetic modelling . . . 40
3.5 Exciton binding energy via Elliott model . . . 42

4 Hot Carrier Confinement in Lead Halide Perovskite Nanomaterials 44
4.1 Background and motivation . . . 44
4.2 Specific experimental details . . . 46
4.2.1 Sample preparation and characterisation . . . 46
4.2.2 PPP-NIR . . . 49
4.3 Results and discussion . . . 49
4.4 Kinetic modelling . . . 57
4.5 Conclusions . . . 62

5 Hot Carrier Trapping in Lead Halide Perovskite Nanocrystals 64
5.1 Background and motivation . . . 64
5.2 Specific experimental details . . . 66
5.2.1 Sample preparation and characterisation . . . 66
5.2.2 PPP-Vis . . . 66
5.3 Results and discussion . . . 67
5.4 Kinetic modelling . . . 71
5.5 Conclusions . . . 75

6 Hot Carrier Mobility in Lead Halide Perovskite Single-Crystals 77
6.1 Background and motivation . . . 77
6.2 Specific experimental details . . . 81
6.2.1 Sample preparation and characterisation . . . 81

6.2.2 PPP-THz 82
6.3 Results and discussion 83
6.4 Kinetic modelling 88
6.5 Conclusions 91

7 Summary and Outlook **93**

References **96**

List of Publications

- **B. P. Carwithen**, T. R. Hopper, Z. Ge, N. Mondal, T. Wang, R. Mazlumian, X. Zheng, F. Krieg, F. Montanarella, G. Nedelcu, M. Kroll, M. Albaladejo-Siguan, J. M. Frost, K. Leo, Y. Vaynzof, M. I. Bodnarchuk, M. V. Kovalenko, A. A. Bakulin, Confinement and Exciton Binding Energy Effects on Hot Carrier Cooling in Lead Halide Perovskite Nanomaterials, *ACS Nano*, **2023**, *17*, 6638–6648

- M. Albaladejo-Siguan, D. Becker-Koch, E. C. Baird, Y. J. Hofstetter, **B. P. Carwithen**, A. Kirch, S. Reineke, A. A. Bakulin, F. Paulus, Y. Vaynzof, Interdot Lead Halide Excess Management in PbS Quantum Dot Solar Cells, *Adv. Energy Mater.*, **2022**, *12*, 2202994

- J. Ye*, N. Mondal*, **B. P. Carwithen**, Y. Zhang, L. Dai, X. Fan, P. Ghosh, C. Otero-Martínez, Z. Yu, Z. Chen, N. C. Greenham, S. D. Stranks, L. Polavarapu, A. Rao, A. A. Bakulin, R. L. Z. Hoye, Extending the Defect Tolerance of Halide Perovskite Nanocrystals to Hot Carrier Cooling Dynamics (in preparation, *authors contributed equally)

List of Figures

1.1 Global energy supply by source 1
1.2 Perovskite crystal structure 3
1.3 Perovskite vs silicon solar cell power conversion efficiency 5
1.4 Semiconductor nanomaterials 6
1.5 Light-matter interactions across the electromagnetic spectrum 9

2.1 Band population distribution of solids 14
2.2 Size effects in colloidal nanocrystals 16
2.3 Polaron 17
2.4 Hot carrier cooling in LHPs 18
2.5 Hot phonon bottleneck vs phonon bottleneck 19
2.6 Recombination pathways 21
2.7 Defects in solids 23
2.8 Defect tolerance of perovskites 24

3.1 Population inversion 26
3.2 Ultrashort laser pulse generation 27
3.3 Basics of UV-vis spectroscopy 28
3.4 Basics of PL spectroscopy 29
3.5 PPP-NIR optical setup 33
3.6 PPP-Vis optical setup 34
3.7 PPP-THz optical setup 37
3.8 THz probe Fourier transformation 38
3.9 Push spectra for PPP-THz 40
3.10 Numerical approximation methods 41

3.11 Elliott model 43

4.1 5 nm $CsPbBr_3$ NCs STEM images 47
4.2 $CsPbBr_3$ NPLs TEM images 48
4.3 Optical microscope images of $(PEA)_2PbI_4$ films 49
4.4 Nanomaterial absorption and photoluminescence spectra 50
4.5 Pulse action on PPP-NIR transients; Push IRF; Monte Carlo simulation . . . 51
4.6 Hot carrier dynamics of 5 nm $CsPbBr_3$ NCs 53
4.7 Hot carrier dynamics of $CsPbBr_3$ NPLs 54
4.8 Hot phonon bottleneck in $(PEA)_2PbI_4$ 55
4.9 Hot carrier relaxation pathways in confined LHPs 58
4.10 Elliott model fits to LHP nanomaterial UV-vis spectra 59
4.11 Kinetic model of hot phonon bottleneck behaviour in LHP nanomaterials . . . 61

5.1 TEM images for $CsPbX_3$ NCs 66
5.2 UV-vis absorption and PL spectra, and compositional analysis of $CsPbX_3$ NCs 67
5.3 Excitation energy-dependent PLQY of $CsPbX_3$ NCs 69
5.4 Choice of spectral window for hot carrier trapping dynamics 70
5.5 Density-dependent hot carrier lifetimes in $CsPbX_3$ NCs 71
5.6 Schematic diagram of hot carrier trapping kinetic model in $CsPbX_3$ NCs . . . 72
5.7 Kinetic model of effect of defects on hot carrier dynamics 74

6.1 Energy state diagram for PPP-THz 81
6.2 OPTP kinetics for $CsPbBr_3$ single-crystals 83
6.3 PPP-THz transients for $CsPbBr_3$ single-crystals 84
6.4 PPP-THz bleach recovery timescales 85
6.5 Temperature-dependence of the PP-THz dynamics 87
6.6 Temperature-dependence of the PPP-THz bleach recovery timescales 88
6.7 Schematic diagram of kinetic model for PPP-THz 89
6.8 Simulated temperature-dependent photoconductivity kinetics 90

List of Tables

4.1 Elliott fitting parameters for UV-vis absorption spectra 60

4.2 Kinetic model fitting parameters for hot carrier confinement in LHPs 62

5.1 Kinetic model fitting parameters for hot carrier trapping in $CsPbX_3$ NCs. . . 74

6.1 Kinetic model parameters for temperature-dependent PPP-THz 91

Nomenclature

Frequently used abbreviations

AO	Atomic orbital	**OPTP**	Optical-pump–THz-probe
BBO	β-barium borate	**PCA**	Photoconductive antenna
CB	Conduction band	**PCE**	Power conversion efficiency
CBM	Conduction band minimum	**PD**	Photodiode
c-Si	Crystalline silicon	**PIA**	Photoinduced absorption
DC	Direct-current	**PL**	Photoluminescence
DOS	Density of states	**PLQY**	Photoluminescence quantum yield
ES	Excited state	**PP**	Pump-probe
FET	Field-effect transistor	**PPP**	Pump-push-probe
GS	Ground state	**PPP-NIR**	Pump–push–NIR-probe
GSB	Ground state bleach	**PPP-THz**	Pump–push–THz-probe
HOMO	Highest occupied MO	**PPP-Vis**	Pump–push–Visible-probe
LED	Light-emitting diode	**PV**	Photovoltaic
LHP	Lead halide perovskite	**QD**	Quantum dot
LO	Longitudinal optical	**QW**	Quantum well
LUMO	Lowest unoccupied MO	**RP**	Ruddlesden-Popper
ML	Monolayer	**SC**	Solar cell
MO	Molecular orbital	**SE**	Stimulated emission
NC	Nanocrystal	**TA(S)**	Transient absorption (spectroscopy)
ND	Neutral density	**TEM**	Transmission electron microscopy
NIR	Near-infrared	**UV-vis**	Ultraviolet-visible
NPL	Nanoplatelet	**VB**	Valence band
OD	Optical density	**VBM**	Valence band maximum
OPA	Optical parametric amplifier	**XPS**	X-ray photoelectron spectroscopy

Chemical abbreviations

ASC18	3-N,N-(dimethyloctadecyl-ammonio)propansulphonate	OA	Oleate
		OAm	Oleylammonium
FA	Formamidinium	ODE	1-Octadecene
MA	Methylammonium	PEA	Phenylethylammonium
MeOAc	Methyl acetate	TOP	Trioctylphosphine

Frequently used symbols

Δ, δ	Change	F	Fluence
ϵ	Dielectric constant	f, ν, ω	Frequency
λ	Wavelength	I	Intensity
μ	Mobility, Reduced mass	k	Rate constant
τ	Lifetime	m	Mass
ϕ	Quantum yield	m^*	Effective mass
A	Absorbance, Area	n	Carrier density, Refractive index
E	Energy, Field strength	R	Radius
E_b	Exciton binding energy	T	Temperature, Transmittance
E_g	Band gap energy	t	Time

Physical constants

c	2.998×10^{8} m s^{-1}	Speed of light in vacuum
e	1.602×10^{-19} C	Elementary charge
h	6.626×10^{-34} J s	Planck constant
k_B	1.381×10^{-23} J K^{-1}	Boltzmann constant
m_e	9.109×10^{-31} kg	Mass of stationary electron
ϵ_0	8.854×10^{-12} F m^{-1}	Permittivity of vacuum

1 Introduction

1.1 Solar energy

Scientists and policy-makers have long understood the link between burning fossil fuels and global climate change which, if left unchecked, will continue to have ever more devastating ecological and societal consequences.[1–6] Despite this, fossil fuels still represent more than 75% of world energy production (Figure 1.1a).[7–9] Record temperatures hit the United Kingdom in 2022, strongly linked with climate change that currently sees global average temperatures 1.1 °C higher than pre-industrial times. The United Nations predicts this will rise to 2.8 °C under current government policies – far in excess of the 1.5 °C pledge under the 2015 Paris Agreement aimed at limiting catastrophic impacts on the environment.[10]

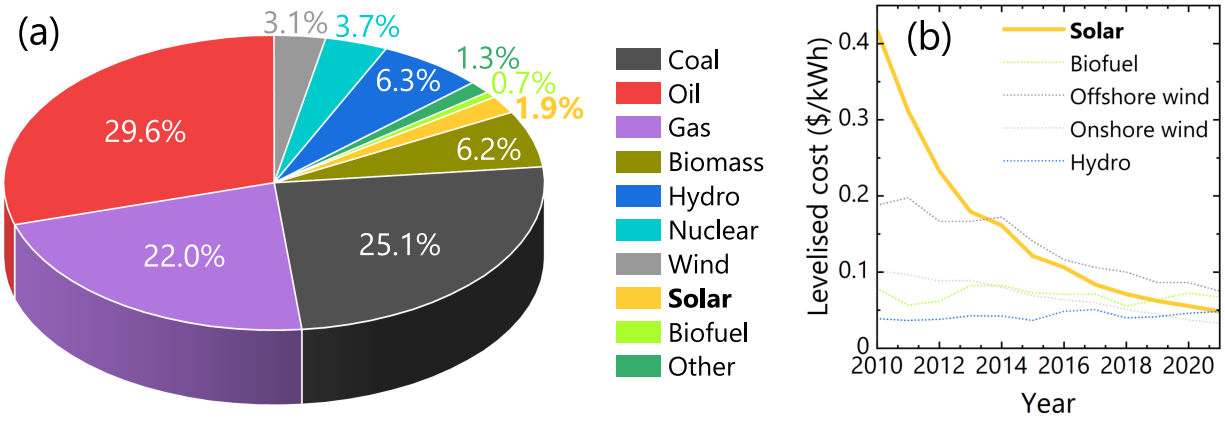


Figure 1.1 – (a) Global primary energy share by source, adapted from Ref. [9]. (b) Levelised cost of renewable energy production, adapted from Ref. [11].

Low-carbon, renewable energy sources are needed in order to alleviate reliance on fossil fuels such as oil, coal and gas. For example, efforts have been made to harness wind, tidal,

hydroelectric, geothermal and biofuel energy. However, perhaps the most promising is solar energy: ∼3 million exajoules reaches the Earth's surface from the Sun per year, enough to meet global energy demand several thousand times over.[12] While it is not, as described later, even theoretically possible to harness all of the Sun's energy, it is certainly a plentiful resource that demands further utilisation. Crystalline silicon (c-Si) currently occupies 95% of the photovoltaic (PV) market, largely owing to its abundance and low toxicity while also benefiting from parallel advances in the electronics industry.[13] However, to attain the typical commercial power conversion efficiency (PCE) of ∼20%, the feedstock silicon needs to undergo cost- and energy-intensive processing at high temperatures that remove chemical and structural impurities.[14,15] Paradoxically, c-Si is a relatively poor absorber of light and so thick wafers need to be produced to compensate for this, resulting in solar cells (SCs) which are heavy and inflexible and further adding to the cost of production and associated infrastructure.[16] In spite of all this, utility-scale PV is among the cheapest (∼0.05 US$/kWh) of all major energy sources (Figure 1.1b), particularly in light of the recent fossil fuel price crisis.[11] However, this clearly has not yet translated to its market share and so "next-generation" PV technologies require a paradigm shift to promote wider roll-out through lower costs and higher efficiencies.[17,18]

In recent years, "soft" optoelectronic materials – characterised by charge transport accompanied by significant nuclear rearrangements about their equilibrium position[19] – have garnered intense research interest towards filling the limitations of c-Si. These include organic molecular semiconductors which have already found applications in displays as *organic light-emitting diodes* (OLEDs),[20,21] with promising results also for PV devices.[22] These materials are solution-processable at moderate temperatures, and thus hold promise as cheap and scalable alternatives to c-Si-based devices. Furthermore, they can be deposited as lightweight flexible thin-films which further extends their possible use cases into markets previously inaccessible to wafer c-Si, such as wearable electronics or semi-transparent windows.[23] Hybrid organic-inorganic materials, introduced in the following section, are another example of soft electronics and are the central focus of this thesis.

1.2 Perovskites

A *perovskite* is a material with a stoichiometry of ABX_3 and a crystal structure comprised of corner-sharing $[BX_6]$ octahedra with A filling the cuboctahedral voids (Figure 1.2). The term was first coined by mineralogist Gustav Rose in 1839[24] (in homage to a Count Lev *Perovskiy*[25]) to describe calcium titanate, $CaTiO_3$. To a first approximation, any choice of A, B and X can form a stable perovskite structure provided the combination of their ionic radii falls within a tolerance factor set out by Goldschmidt:[26]

$$0.8 < \frac{R_A + R_X}{\sqrt{2}\,(R_B + R_X)} < 1.1 \tag{1.1}$$

Indeed, $CaSiO_3$ ('davemaoite') was recently discovered in the Earth's lower mantle,[27] while other oxide perovskite variants have found applications as ferroelectrics and are the central motifs of current record "high-temperature" superconductors.[28] Synthetic $LaWN_3$[29] and 'all-organic'[30] perovskites are other more exotic examples that have been reported in recent years. However, the remainder of this thesis will focus on *lead halide perovskites* (LHPs). As depicted in Figure 1.2, A is typically a large monovalent cation such as Cs^+, methylammonium ($CH_3NH_3^+$, or MA^+) or formamidinium ($CH(NH_2)_2^+$, or FA^+); B is Pb^{2+}; and X is a halide such as Cl^-, Br^- or I^-.

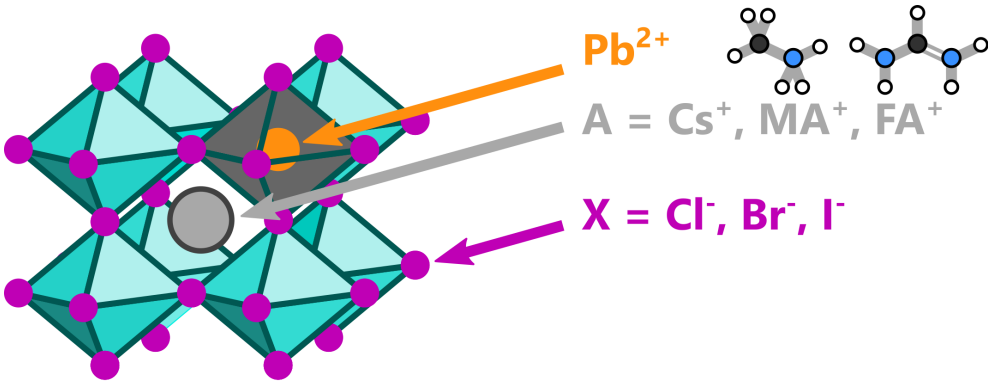


Figure 1.2 – Lead halide perovskites have $APbX_3$ (X = Cl, Br, I) stoichiometry and a crystal structure comprised of corner-sharing PbX_6 octahedra, with the A-site cation (typically Cs, MA or FA) filling the cuboctahedral void.

In 1893, Wells[31] reported the first solution-based synthesis of $CsPbX_3$ (X = Cl, Br, I), with Møller[32] confirming these "cesium plumbohalides" had the perovskite crystal structure in 1958.

It was further noted that the materials were intensely coloured and had a photoconductivity which peaked at a wavelength of visible light that depended on the choice of halide. The electronic properties of halide perovskites then went largely unexplored before the work of Mitzi *et al.* in 1994,[33,34] and it would not be until 2009 that Miyasaka *et al.*[35] published the first example of a PV device incorporating a halide perovskite as its absorber, achieving a PCE of 3.5%. This device was based on a dye-sensitised solar cell (DSSC) architecture consisting of a mesoporous titania charge extraction layer[36] coated with $MAPbI_3$, surrounded by a I_2/I^- redox solution, and was further optimised to 6.5% PCE in 2011 by Park *et al.*[37] The main issue with the DSSCs was that the perovskite would rapidly degrade in the electrolyte solution. With the introduction of all solid-state SCs in 2012 from groups led by Snaith, Murakami and Miyasaka;[38] and Grätzel and Park[39] simultaneously, not only was this stability issue solved but device efficiencies were pushed above 10% for the first time.

These high efficiencies are the result of large visible light absorption cross-sections[40,41] and low exciton binding energies,[42,43] giving rise to efficient free charge-carrier generation; while their long carrier lifetimes and reasonable carrier mobilities[44,45] result in long diffusion lengths[46,47] which, combined with their solution processability, allow the facile fabrication of printed SCs. The low temperatures involved in fabrication result in a much higher defect density than c-Si, but the alleged *defect tolerance* of perovskites (elaborated upon in Section 2.5) minimises their impact on carrier dynamics. The remarkable optoelectronic properties of halide perovskites have since galvanised the research community, with the rate of publications and device improvements increasing rapidly in the last decade (Figure 1.3). The current record PCE for a single-junction LHP SC now stands at 26.1%.[48]

Four main challenges need to be overcome for LHPs to become a key PV market player: cost, scalability, stability and toxicity. The first two are intertwined to some extent – the promise of solution-processed printable electronics ought to make perovskites cheaper to produce than c-Si, but controlled laboratory-measured properties need to be tested in mass-manufacture. If this is achieved, economies of scale should bring the cost down further. LHP devices also need to display the same 'real-world' product lifetimes as those of c-Si competitors ($\sim$25 years),

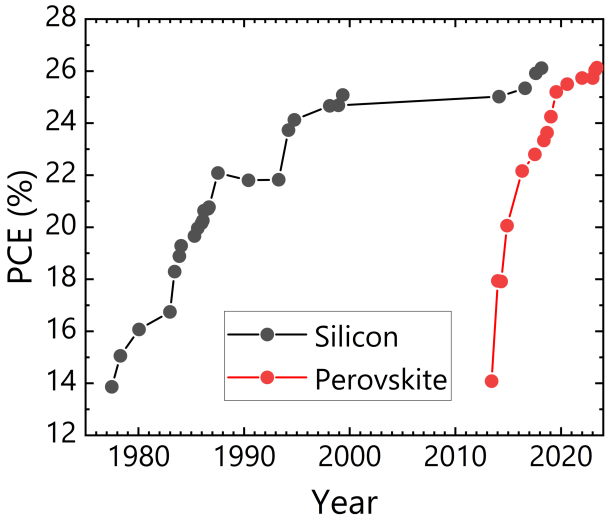


Figure 1.3 – Record power conversion efficiencies for c-Si and perovskite SCs over time. Perovskite-based devices have experienced a rapid rise in laboratory-tested efficiency. Adapted from Ref. [48].

likely with scrupulous encapsulation of the active layer to protect it from moisture and oxygen. However, perhaps the foremost concern with the wide-scale deployment of LHP devices is the toxicity of Pb and the issues this may cause if it leaches into biological ecosystems via rivers and fields.[49–51] That said, a full-stack device may need only contain a small amount of perovskite and so could remain below regulatory thresholds for Pb content;[52] and the precise transport mechanisms and bioavailability of Pb are non-trivial, demanding extensive further research.[53]

Another strategy to evade the issue is substituting Pb entirely, for example with Sn or Ge.[54] However, to date these devices have not reached the same performance as their Pb-based counterparts and suffer from low stability under ambient conditions.[55] Ag/Bi-based *double perovskites* (with formula A_2AgBiX_6) offer better stability but their indirect band gaps and low-dimensional structure inhibit free carrier generation, limiting SC performance.[56,57]

1.3 Nanomaterials

Nanomaterials are those with characteristic length scales that fall between ∼1 and ∼100 nm (1 nm = 10^{-9} m). When Ekimov & Onushchenko[58] first reported the nucleation of CuCl "microcrystals" in a glass medium in 1982, they showed that their optical spectra depended on the growth temperature, and therefore the *size* of the inclusions: the absorption lines were blue-

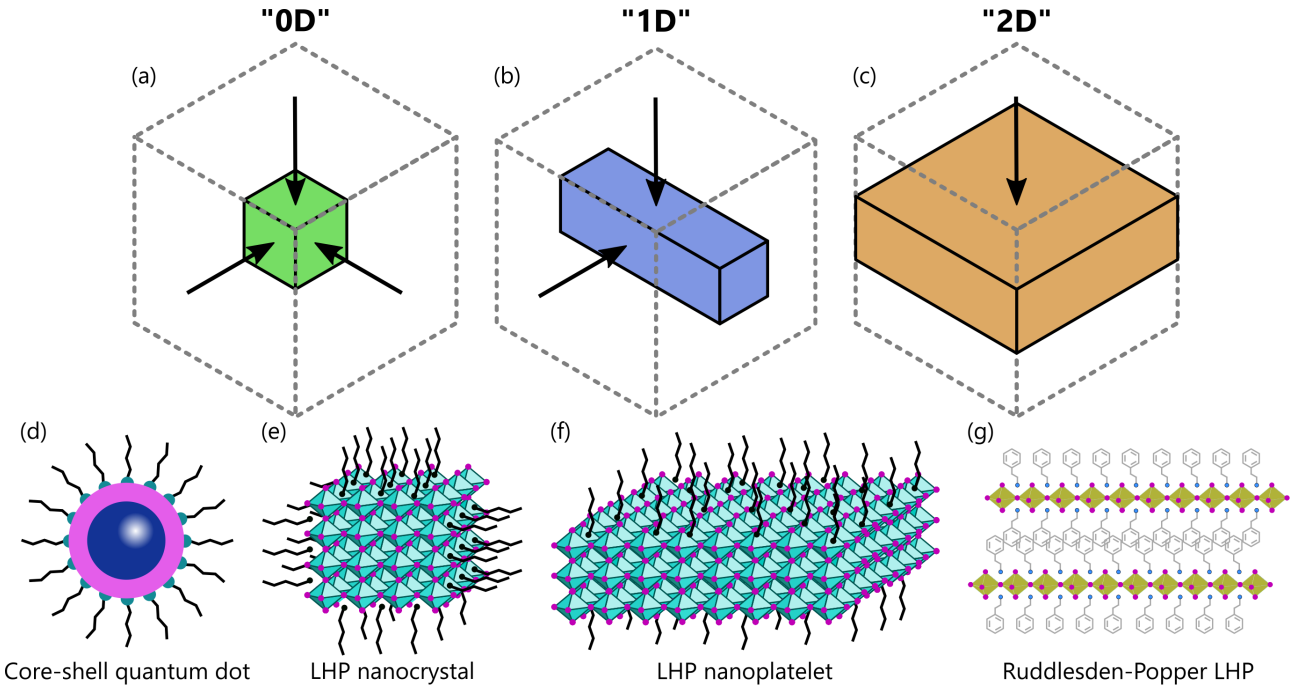


Figure 1.4 – Schematic diagrams of confinement in (a) 0D, (b) 1D and (c) 2D semiconductors. (d-g) Schematic diagrams of selected semiconductor nanomaterial architectures.

shifted with respect to the bulk for smaller crystallites. Efros & Efros[59] then showed how the optical gap depended quantitatively on the extent of this *quantum confinement*. Simultaneously, Brus *et al.*[60] were developing the solution-based synthesis of *colloidal* CdS nanocrystals (NCs), noting that the absorption onset could be tuned across the entire visible light spectrum altering only the size of the few-nm crystallites. This recipe was later improved with the use of 'arrested precipitation' through molecular additives that not only passivated the NC surface (lowering non-radiative losses through mid-gap states caused by dangling bonds), but also allowed functionalisation of the NC.[61,62] If a NC is much smaller than the bulk Bohr radius of the material ($R \ll a_B$), a 'strong confinement' regime is established and the three-dimensionally confined system is referred to as a *quantum dot* (QD, Figure 1.4a).[63]

The 'hot-injection method' first formulated by Bawendi *et al.*,[64] wherein a cold precursor solution is rapidly added to a hot solvent to produce highly monodisperse NCs, proliferated their use and has since become a mainstay in the synthesis of many other NC classes.[65] Later, *core-shell* NCs (Figure 1.4d) were reported[66,67] which involved passivation of the core NC material with another inorganic semiconductor, further improving stability and expanding their functionality.[68] Colloidal NCs now pervade many technologies, in particular as light-

emitting diodes (LEDs) due to their high electro/photoluminescence efficiencies, tunability and colour purity from scalable solution-based fabrication routes.[69] NCs also have applications in photocatalysis owing to their large and functionalisable surface,[70] as well as bio-imaging.[71–73]

By 2015, reports on the synthesis of colloidal LHP NCs (Figure 1.4e) were beginning to emerge.[74–78] From relatively simple procedures, the NCs formed were monodisperse and highly emissive; and their band gap could be tuned over the entire visible region through control over their size and composition – immediately offering promise as cheap and scalable LEDs, while efficient optical gain was also reported in LHP NC lasers.[79,80] Although NCs have traditionally not been a viable option as SC absorbers due to the poor charge transport that arises from the organic passivation layers, early work by Swarnkar *et al.* achieved >10% PCE in a $CsPbI_3$ NC device.[81] While the soft ionic bonding present in LHPs means syntheses can be carried out at lower temperatures than their inorganic counterparts, this can also present other challenges.[82] For example, the ligand-surface binding is highly dynamic and can affect long-term stability.[83] The departure from ideal tolerance factor found in iodide LHPs makes them unstable to phase transitions,[84] initially limiting the use of NCs as infrared emitters.[85] Since their inception, improvements to the stability and utility of LHP NCs have been extensive[86–90] due to fine-tuned post-synthetic treatments[91,92] and better choice of ligand.[93,94]

Confinement may instead only be imposed in two dimensions (Figure 1.4b), as in the case of *nanorods*;[95] or one dimension (Figure 1.4c), as in the case of *quantum wells* (QWs). Indeed, QWs were first proposed by Esaki & Tsu[96] in 1970 (thus pre-dating QDs), suggesting that excitations could be strongly quantum-confined within few-atom-thick, epitaxially grown layers of GaAs inter-digitated with $Al_{1-x}Ga_xAs$, whose wider gap would provide the energetic barrier to delocalisation. While this necessitates the use of bulky, high-vacuum deposition chambers, pseudo-2D colloidal semiconductor *nanoplatelets* (NPLs) can also now routinely be synthesised in solution (Figure 1.4f). Schmidt *et al.*[97] are credited with the first method to successively grow colloidal perovskite NPLs; with Tyagi *et al.*[98] showing the extent of blue-shifting in the absorption and emission spectra depended on the thickness of the NPL. Here, the $MAPbBr_3$ precursor was grown in a solution containing long-chain octylammonium ligands, which termi-

nated the growth of the NPLs by being too large to fit within the bulk A-site cavity, breaching the Goldschmidt tolerance factor described in Equation 1.1.

'Layered' 2D Ruddlesden-Popper (RP) perovskites represent a subtly distinct class of materials with the nominal formula $L_2[ABX_3]_{n\text{-}1}PbX_4$ (L = ligand). The inorganic Pb-X sub-lattice effectively becomes confined by the organic spacer layer, and are therefore deemed the closest analogue of the traditional QW structures (Figure 1.4g).[99–101] By removing the A-containing precursor, $n = 1$ RP LHPs (where n refers to the number of monolayers, MLs, of lead halide octahedra) are somewhat more facile to isolate than their low-n counterparts, which undergo rapid growth and result in greater thickness heterogeneity.[102] The $n = 1$ RP perovskites exhibit a very high degree of spatial confinement, and carriers are also restricted by the dielectric confinement imparted by the exact choice of ligand for a given n thickness. Higher-dielectric spacers such as aromatic molecules reduce confinement over lower-dielectric aliphatic spacers.[103] It might be expected that the excitonic character of RP LHPs would limit their use in SCs where free charge generation is paramount. However, their addition to bulk polycrystalline LHP[104–107] and PbS QD[108] films has been shown to dramatically improve device stability without forfeiting efficiency. The consensus here is that the hydrophobicity of the spacer ligands minimises moisture ingress that would otherwise lead to degradation.

All in all, the properties of LHPs and their nanoscale derivatives are thus highly tunable through control over composition, size and dimensionality. Combined with their promising optoelectronic properties from facile synthesis routes, they are excellent candidates for next-generation devices and their photophysics demand further interrogation.

1.4 Ultrafast spectroscopy

The LHP properties described thus far are largely predicated on the behaviour of its electrons following absorption (or preceding emission) of light. These behaviours, in turn, are brought about by a balance of *dynamical* processes, a subset of which will be more thoroughly described in Chapter 2.

The ability to take a snapshot of any process *within* its duration is invariably key to understanding it. The earliest example of this endeavour is usually attributed to Eadweard Muybridge's 1878 use of high-speed photography to *time-resolve* the mechanics of a running horse that were otherwise imperceptible to the naked eye. While this relied on the generation of short bursts of light to illuminate the subject at distinct periods of time, modern video cameras are equipped with sufficiently high-speed electronics so as to keep track of fast-moving objects. However, the dynamics of photophysical phenomena in LHPs are considerably faster, usually necessitating the return to optical detection. The universally adopted method of time-resolving these processes is *pump-probe* (PP) spectroscopy. Here, one brief pulse of light (the 'pump') initiates a dynamical process, before its evolution is tracked using a second delayed pulse (the 'probe'). An early example of this was the 'flash photolysis' method employed by Norrish and Porter in 1950[109,110] to measure the absorption spectra of *intermediates* in photochemical reactions. Since then, the advent of few-femtosecond (1 fs = 10^{-15} s) light sources has permitted the study of a rich array of '*ultrafast*' processes occurring on sub-picosecond (1 ps = 10^{-12} s) timescales, beginning with the work by Zewail and co-workers in the 1980s.[111–113]

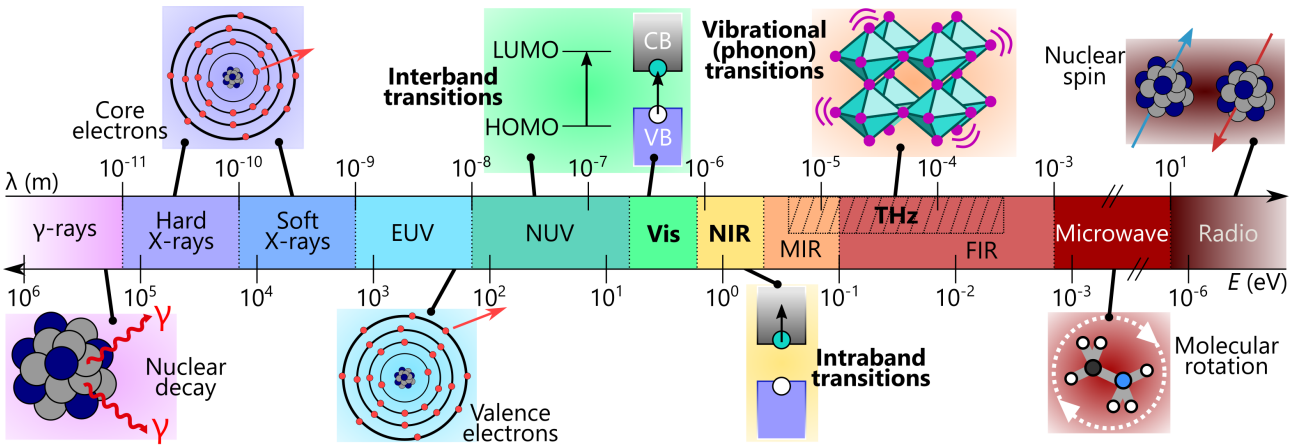


Figure 1.5 – Light-matter interactions across the electromagnetic spectrum. EUV: extreme ultraviolet; NUV: near-ultraviolet; Vis: visible; NIR: near-infrared; MIR: mid-infrared; FIR: far-infrared; 1 eV = 1.602×10^{-19} J.

The power of ultrafast spectroscopy lies in being able to control the precise nature of the optical excitation, and interrogate its evolution on timescales relevant to the mechanisms that decide its fate.[114] As shown in Figure 1.5, this can be achieved by tuning the wavelength/energy of light used to induce or observe a particular energy transition. Furthermore, the materials' intrinsic

properties can be divulged without needing to build full working devices. The electromagnetic spectrum spanning the visible (Vis), near-infrared (NIR) and terahertz (THz) regions will be of particular relevance for this thesis and used, respectively, to study interband and intraband electronic dynamics; as well as lattice vibrations in response to electronic excitation.

1.5 Aims and motivations for the thesis

LHPs are a class of highly promising optoelectronic materials, particularly as regard to their potential for supplanting the market dominance of c-Si in PVs devices. Their relatively simple fabrication routes and favourable immunity to defects have permitted a rapid rise in device efficiencies, which are now approaching the single-junction limit that largely originates from the relaxation of above-gap photocarriers (i.e. "hot carrier cooling", described in Section 2.3). Therefore, a fundamental understanding of the properties and dynamics governing this process is required in order to push efficiency towards, and even above, this threshold. Herein, hot carrier cooling dynamics in a range of emerging material systems are isolated and studied through the lens of their density-dependent response to a novel spectroscopic approach.

Chapter 2 provides an overview of the key photophysical mechanisms operating within LHPs and other optoelectronics. Together, these govern the production and potential utilisation of charge-carriers.

Chapter 3 presents the key steady-state and time-resolved methods employed in order to investigate hot carrier cooling dynamics in a range of LHP systems. Three variants of ultrafast 'pump-push-probe' spectroscopy are described, each tailored to understanding a particular aspect of hot carrier dynamics.

Chapter 4 tackles the disputed effect of quantum confinement on hot carrier dynamics in LHP nanomaterials. This is achieved by studying a large span of confinement regimes with a NIR probe, and kinetic modelling of the results points to the dominant role of a previously unaddressed carrier-carrier coupling mechanism.

In **Chapter 5**, the study of trap states in LHP NCs is extended to their effect on hot carrier

dynamics via a visible light probe. By systematically introducing defects to the surface of LHP NCs, the hot carrier lifetime is suppressed in Br-based NCs, but no effect is observed in I-based analogues.

Chapter 6 then shifts the focus to single-crystalline LHPs. Using a THz probe, the mobility dynamics of hot carriers are assessed. The results suggest that the removal of excess energy held within hot phonons dominates the transient response, momentarily suppressing the mobility of carriers after intraband relaxation.

Finally, the main findings from this thesis are summarised in **Chapter 7**, before potential further research avenues are suggested to address unanswered questions.

2 Perovskite photophysics – from the ground, up

Myriad dynamical processes govern the generation, loss and extraction of charge-carriers following light absorption in optoelectronic materials. Ultimately, the rational design of paradigm-shifting materials will only be possible through a fundamental understanding of how factors such as composition, process engineering, and load conditions impact these processes on microscopic time- and length-scales. In this Chapter, a review of these physical processes is presented which can be applied generally to all semiconductors, but with a particular focus on LHPs which form the cornerstone of this thesis.

2.1 Electronic structure of solids

The time-independent Schrödinger equation is $\hat{H}\Psi = E\Psi$. For the simplest atom, hydrogen, the Hamiltonian operator is $\hat{H} = -\frac{\hbar^2}{2m_\mathrm{e}}\nabla^2_\mathrm{e} - \frac{\hbar^2}{2m_\mathrm{N}}\nabla^2_\mathrm{N} - \frac{e^2}{4\pi\epsilon_0 r}$ where each succesive term accounts for the kinetic energy of the electron, the nucleus (proton), and the Coulomb potential between them, respectively. Solving the Schrödinger equation – i.e. finding the wavefunctions $\Psi(r)$ that satisfy the Hamiltonian – gives the series of allowed hydrogen atomic orbitals (AOs).

With consideration to the simplest molecule – two protons bonded by one electron – $H_2{}^+$, the Hamiltonian then becomes $\hat{H} = -\frac{\hbar^2}{2m_\mathrm{e}}\nabla^2 - \frac{e^2}{4\pi\epsilon_0}\left(\frac{1}{r_\mathrm{A}} + \frac{1}{r_\mathrm{B}} - \frac{1}{R}\right)$, where $r_\mathrm{A/B}$ is the distance of the electron from each nucleus, and R the internuclear separation. This Schrödinger equation can be solved analytically to give the $H_2{}^+$ molecular orbitals (MOs). However, for any system more

complex, there are no exact solutions to the Schrödinger equation and thus an approximation must be used. One such approximation is that a MO is a linear combination of AOs (LCAO-MO): $\psi_{\pm} = N(\psi_{\mathrm{A}} \pm \psi_{\mathrm{B}})$ where N is a normalisation factor, and ψ_{A} and ψ_{B} are the 1s AOs of the two hydrogen atoms. The $\pm$ operator arises because the two AOs may interfere constructively or destructively.

Constructive interference of the two AOs gives rise to a ψ_{+} MO with probability density $|\psi_{+}|^2 = N^2\,(\psi_{\mathrm{A}}^2 + \psi_{\mathrm{B}}^2 + 2\psi_{\mathrm{A}}\psi_{\mathrm{B}})$. That the last term – arising from the *overlap* of the orbitals on different H atoms – is positive, means that there is a greater electron density between them, and a *bonding* MO is formed. Conversely, an *antibonding* MO with probability density $|\psi_{-}|^2 = N^2\,(\psi_{\mathrm{A}}^2 + \psi_{\mathrm{B}}^2 - 2\psi_{\mathrm{A}}\psi_{\mathrm{B}})$ is formed due to destructive interference. It follows that the energies of the bonding and antibonding MOs are lower and higher than an isolated H 1s orbital, respectively, with a (de-)stabilisation energy that depends on their separation, R.

While simple, LCAO-MO theory can help explain the electronic structure of solids. Hypothetically, by adding n atoms successively in a line, each interacts with its immediate and distant neighbours to different extents and so the (de-)stabilisation energies of the resulting (anti)bonding MOs also vary. As a result, the emerging picture is that of filling in the range of allowed energies with orbitals that become closer and closer in energy such that, in the limit of $n \to \infty$, the difference in energy between adjacent orbitals is zero. In other words, individual orbitals become indistinguishable from the next and a continuous *band* of electronic states is formed in solids.[115]

The probability of an electron residing in a state follows the Fermi-Dirac distribution, which is analogous to the Maxwell-Boltzmann distribution but accounting for the fact that only one electron (fermion) may occupy each state:

$$F(E) = \frac{1}{\exp\left[(E - E_{\mathrm{F}})/k_{\mathrm{B}}T\right] + 1} \tag{2.1}$$

where E_{F} is the Fermi level, corresponding to a hypothetical state with $F(E) = 50\%$. The product of the Fermi-Dirac distribution and the density of states (DOS, g) gives the population

distribution (n):

$$n(E)\,\mathrm{d}E = F(E)\,g(E)\,\mathrm{d}E \tag{2.2}$$

This is a vital parameter in categorising the conductivity of a solid. For metals, the Fermi level lies *within* a band and so electrons are delocalised in a large number of thermally accessible states at room temperature and are thus able to conduct electricity. For insulators and semiconductors, the Fermi level lies *between* bands – i.e. in the *band gap* – localising valence electrons which results in low (dark) conductivity (Figure 2.1). The highest occupied band is termed the valence band (VB); and the lowest unoccupied band the conduction band (CB); the smallest difference in energy between them is termed E_g. In LHPs, the band gap becomes larger for smaller A-cations[116–118] and halides[119–122] due to changes in lattice parameter and octahedral tilting.

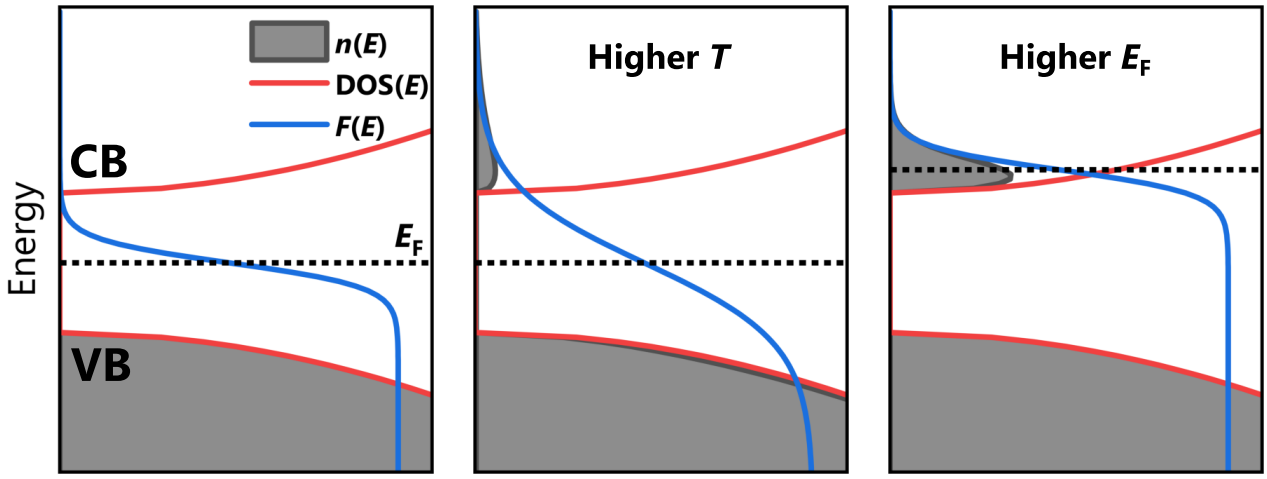


Figure 2.1 – Modelled effect of temperature and Fermi level (E_F) on band population distribution. When E_F lies between bands, the VB is fully occupied. Increasing either temperature or the E_F results in a partially occupied CB and higher conductivity.

While pure semiconductors have no intrinsic electrical conductivity at absolute zero, and generally have low conductivities at room temperature, they can be made to conduct by *doping*. For example, if an impurity atom with an extra valence electron is added to the crystal structure, this can delocalise into the CB and increase conductivity.[123] Charge-carriers can also be injected into the CB via an external electrical bias. Of most relevance for this thesis, the band gap can instead be surmounted by transferring sufficient energy to a VB electron via a *photon*. The physics of charge-carrier generation, and their ensuing loss processes, upon light

absorption are explored in the following sections.

2.2 Light absorption

The net rate of transition ($r_{i\to f}$) between any two electronic states (i and f) separated by E is described by *Fermi's Golden Rule*, given in Equation 2.3, under first-order time-dependent perturbation theory.[124] The transition matrix element describes the selection rules for coupling between the two states: for example, optical excitation must be *direct*, i.e. not involve a change in momentum ($\mathbf{k}_i = \mathbf{k}_f$). That LHPs generally have a nearly direct band gap[125–127] gives rise to their superior light absorption properties over the indirect-gap c-Si.[128–130] The second group of terms accounts for the population of i and f: the transition rate is greater when there is a high density of occupied states around i, and high density of vacant states around f.

$$r_{i\to f} = \frac{1}{h}\int \underbrace{|\langle i|\,\hat{H}'\,|f\rangle|^2}_{\substack{\text{matrix}\\ \text{element}}} \underbrace{[F(E_i) - F(E_f)]\; g_i(E_i) g_f(E_f)}_{\substack{\text{population density of}\\ \text{initial and final states}}} \,\mathrm{d}E_i \tag{2.3}$$

When a photon with energy $h\nu \geq E_\mathrm{g}$ is absorbed by the material, an electron is excited into the CB and a hole left in the VB. The electron and hole are then coupled by an essentially Coulombic interaction, whose strength depends on the charge screening properties of the lattice. For materials with a low dielectric constant (ϵ), this coupling is large and thus the electron-hole pair are bound as an *exciton* quasi-particle with a characteristically large *exciton binding energy* ($E_\mathrm{b} \gg k_\mathrm{B}T$). Conversely, high ϵ materials generally have a low E_b ($\sim k_\mathrm{B}T$) and the electron and hole readily dissociate as free charge-carriers at room temperature.

As described in Section 1.3 and depicted in Figure 2.2, spatial confinement in NCs also leads to increased E_b. Equation 2.5 describes how quantum confinement alters the optical gap of a NC (of radius R) relative to the bulk.

$$E_\mathrm{opt} \approx E_\mathrm{g,bulk} + E_\mathrm{conf} - E_\mathrm{b} \tag{2.4}$$

$$\approx E_\mathrm{g,bulk} + \frac{h^2}{8\mu^*_\mathrm{eh}R^2} - 1.8\frac{e^2}{\epsilon R} \tag{2.5}$$

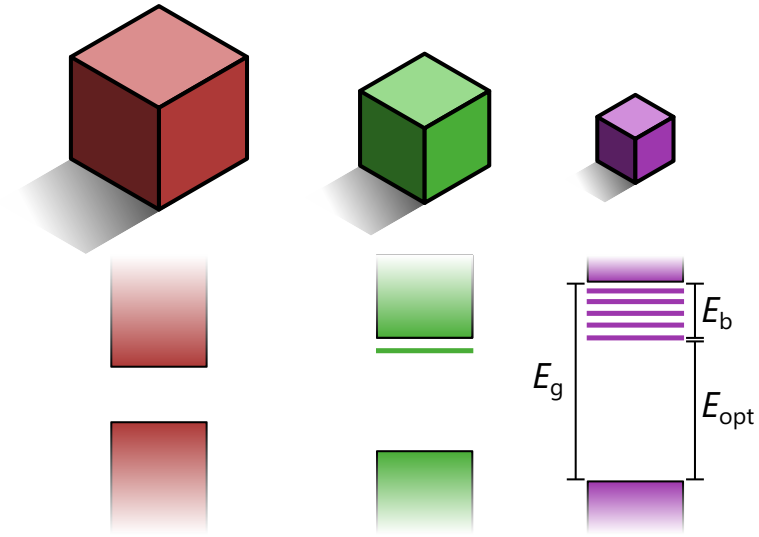


Figure 2.2 – With decreasing NC size, the band gap (E_g), exciton binding energy (E_b) and optical gap (E_{opt}) increase due to quantum confinement.

The second term assumes a spherical 'particle-in-a-box' model to calculate the confinement energy, where μ^*_{eh} is the electron-hole reduced effective mass; and the third term accounts for E_b.[131] That these terms scale differently with R predicts that the optical gap becomes larger for smaller NCs. The partitioning of excited states (ESs) between free carriers and excitons can be quantified under the assumptions of the *Saha model*,[132,133] as will be elaborated upon in Chapter 4.

In materials such as LHPs, characterised by soft bonding between the constituent atoms, the lattice can undergo significant structural distortion in the presence of a charge. The charge and the lattice distortion become coupled to the extent that they may be described by a distinct quasi-particle, the *polaron*, depicted in Figure 2.3.[134,135] This lattice 'dressing' inevitably impacts – and most likely enhances[136] – the charge transport properties of LHPs. Polaron existence has generally been inferred from optical spectroscopy,[137,138] before direct evidence of charge-coupled lattice distortion was recently found through ultrafast structural probes.[139] Among other facets, polaron protection has been touted as a possible cause for the reasonably high carrier mobilities observed in LHPs.[140] As will be described in more detail in Chapter 6, carrier mobility depends inversely on both its effective mass (m^*) and phonon scattering rate. While a polaron has a larger m^* than a bare charge, this is compensated for by screening carrier-phonon scattering.[141]

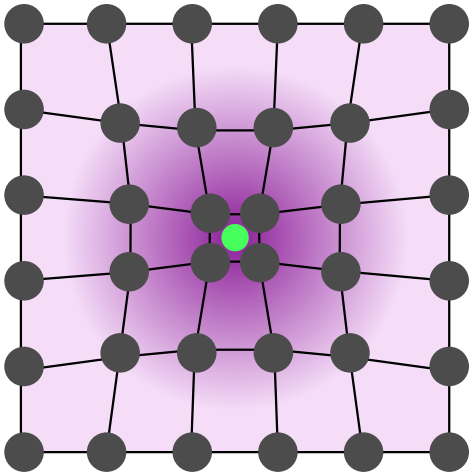


Figure 2.3 – Polarons are formed in LHPs by the distortion of the lattice (black circles) around the charge (green circle).

2.3 Thermalisation and hot carrier cooling

Following above-gap ($h\nu > E_g$) excitation, photocarriers are initially formed with a non-thermal distribution of energies determined by the spectra of the light source (e.g. the Sun or a laser) and the material absorption (Figure 2.4). The electrons and holes then thermalise rapidly (<100 fs[142]) via inelastic carrier-carrier scattering to yield a Fermi-Dirac distribution with a characteristic temperature greater than that of the surrounding lattice ($T_{e/h} > T_l$). This '*hot carrier*' distribution then cools to the band edge on ∼1 ps timescales – conventionally understood to proceed through longitudinal-optical (LO) phonon emission via Fröhlich coupling[143–145] – until $T_{e/h} = T_l$.[146] This has important practical ramifications: the finite band gap of the absorber layer means any photon impinging on a PV device with (i) $h\nu > E_g$ produces above-gap carriers whose excess energy is ultimately lost as heat prior to extraction; while any photon with (ii) $h\nu < E_g$ will not be absorbed. The compromise between these losses under solar illumination leads to an ideal band gap of ∼1.1 eV, corresponding to a theoretical limit of ∼33% PCE for any single-junction SC.[147]

Methods of utilising more of the solar spectrum to improve PCEs include development of tandem SCs. Here, two or more absorbers with differing band gaps are stacked in the device, meaning low-energy photons are absorbed efficiently by the narrow-gap material; and high-energy photons by the wide-gap material. While this presents engineering challenges that can

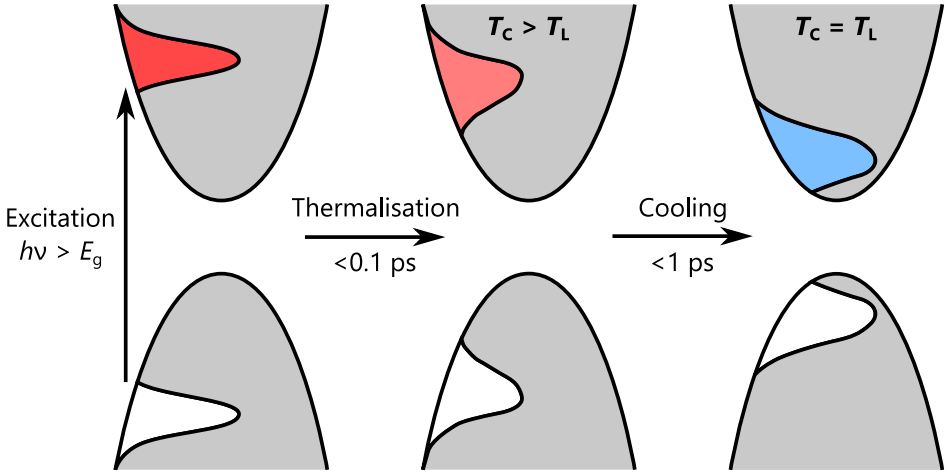


Figure 2.4 – Hot carrier cooling in LHPs proceeds by a three step mechanism: (i) Above-gap light absorption produces non-thermal distribution; (ii) Thermalisation via carrier-carrier scattering forms hot thermal distribution; (iii) Intraband relaxation to form band-edge distribution.

ultimately make tandem devices more expensive, perovskite-Si tandem cells have recently been reported with PCEs greater than that possible in a single-junction c-Si SC.[148,149]

Light absorbers may instead be coated with an organic sensitiser-emitter system which undergoes upconversion of two sub-gap photons to one of sufficient energy to excite the absorber layer, typically via *triplet-triplet annihilation*.[150] Alternatively, if hot carriers could be extracted prior to cooling, more of the initial above-gap photon energy could be harvested to improve open-circuit voltage (V_{oc});[151] or the excess energy may be used to excite a second carrier across the band gap in a process called *carrier multiplication* or *multiple exciton generation*, thereby improving short-circuit current (J_{sc}).[152–156] This latter process is akin to *singlet fission* reported in some organic materials, which yields two triplet states from an initial excitation to a singlet.[157,158]

To realise a working hot carrier SC, the absorber needs to exhibit long cooling times to allow the excess energy to be harvested; and suitable energy-selective contacts must be used to minimise energy dissipation after extraction.[159,160] Indeed, it has been proposed that under 1-Sun illumination with a contact bandwidth of 0.1 eV, cooling times would need to be slowed to 1 ns to see any improvement over the single-junction limit;[161] while rapid carrier thermalisation would also be necessary in order to efficiently re-populate the vacant levels after extraction.[162] Such a device would also require all the 'typical' optoelectronic performance parameters such

as a suitable band gap, high absorption coefficient, long carrier lifetime and good stability. For these reasons, a working example of a hot carrier SC has thus far remained elusive. Practical limitations aside, studying hot carrier cooling dynamics provides fundamental insight into the carrier-phonon and carrier-carrier coupling at play in optoelectronic materials,[163] which forms the main motivation for this thesis.

The first results from optical measurements of hot carriers were published by Shah & Leite in 1969[164] studying the steady-state hot photoluminescence (PL) spectra of GaAs. With the advent of sub-picosecond laser sources,[165] Shank *et al.*[166] published the first time-resolved measurement of hot carrier cooling in GaAs in 1978, with multiple further examples from various groups in the following years.[167–175] A key observation was that hot carrier cooling was slower for higher excitation densities, with Shah *et al.*[176,177] the first to ascribe this to a 'large non-equilibrium phonon population', in agreement also with early calculations for CdSe.[178] This *hot phonon bottleneck effect* is now understood to result from the continuous emission and re-absorption of phonons at higher excitation densities,[179] sustaining the population of hot carriers over longer timescales (Figure 2.5a).

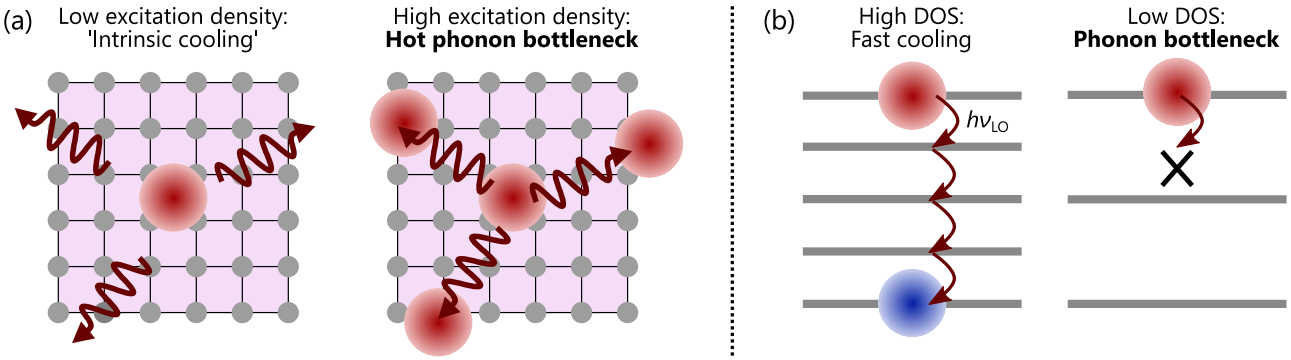


Figure 2.5 – (a) A hot phonon bottleneck is formed at high excitation densities due to continuous emission and re-absorption of hot LO phonons. (b) A phonon bottleneck is formed when the spacing between successive electronic states is greater than the energy of the coupled phonon.

Hot carrier cooling dynamics have now been studied extensively in LHPs. In the first dedicated works, a pronounced hot phonon bottleneck was observed in $MAPbI_3$ by Price *et al.*[180] and Yang *et al.*[181] To explain this, multiple mechanisms have been invoked, such as polaron screening which partially decouples the carriers from LO phonons;[182] inefficient Klemens[183] decay (the conversion of a LO phonon into a pair of counter-propagating longitudinal acoustic

phonons);[184] and acoustic phonon upconversion,[185] both of which would prolong the population of hot LO phonons, and therefore hot carriers. Sekiguchi *et al.*[186] showed that 'pre-heating' phonons using a THz pulse prior to optical excitation magnified the hot phonon bottleneck in time-resolved photoluminescence (TRPL) experiments. There have been some reports in Sn-based LHPs of extremely long (few-ns) hot carrier lifetimes,[187] although this may be an effect of state filling at high carrier densities.

As described in Section 2.2, quantum-confined systems such as NCs often acquire fine structure or discrete regions in their band continua, which ought to also impact their hot carrier dynamics. In 1980, Nozik *et al.*[188] postulated that if the separation between electronic states becomes greater than the energy of the coupled phonon, a multiphonon cooling mechanism is required which should prolong the lifetime of an injected hot carrier – ergo, a *phonon bottleneck* is formed (Figure 2.5b). Simulations by Bockelmann & Bastard[189] predicted the same effect when comparing InGaAs QWs and QDs. However, later experimental investigations by Efros *et al.*[190] showed that cooling is in fact faster in CdSe QDs due to the stronger electron-hole overlap: the low CB DOS of the hot electron is circumvented by Auger-type energy transfer to its coupled hole, which then cools rapidly via the high VB DOS. Klimov *et al.*[191] ruled out the effect of surface coupling because the same dynamics were observed in both colloidal and glass-embedded QDs; and later showed the dynamics were indifferent to the choice of passivating ligand.[192] This was shown conclusively by deliberately sequestering the hole through surface trapping, which led to longer electron cooling times.[193,194] Guyot-Sionnest *et al.*[195] then showed that in this regime, hot electron lifetimes were limited by surface effects, for example via energy transfer to ligand vibrations. By encapsulating the CdSe QDs with a ZnSe shell, the electron and hole could be decoupled while still limiting energy transfer to the surface, and long carrier cooling times were observed.[196] The controversies surrounding the effect of confinement on hot carrier cooling in LHP nanomaterials will be the subject of investigation in Chapter 4.

2.4 Recombination

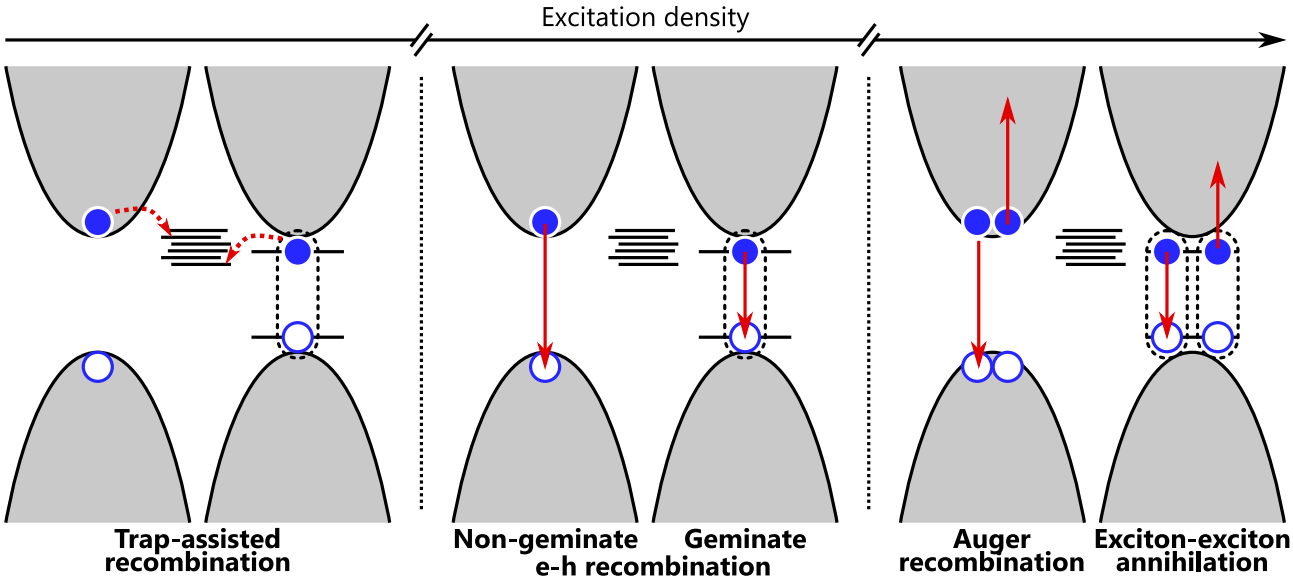


Figure 2.6 – Electron-hole recombination mechanisms are strongly density-dependent.

There are multiple possibilities for the fate of a nascent photocarrier that largely depend on its nature (exciton or free carrier), material properties (crystalline or amorphous) and the excitation density (high or low n), as depicted in Figure 2.6.[197,198] In general, these loss processes can be described by:

$$-\frac{\mathrm{d}n}{\mathrm{d}t} = k_1 n + k_2 n^2 + k_3 n^3 \tag{2.6}$$

Naturally, terms of higher order in n dominate at higher excitation densities. For low n, monomolecular decay processes such as trap-assisted recombination dominate. This is first-order because it involves the scattering of a mobile carrier or exciton with an immobile trap, which then facilitates non-radiative recombination. Geminate exciton recombination dominant in excitonic systems is also monomolecular because it involves the (usually radiative) recombination of a bound electron-hole pair formed by the same photoexcitation event.

At higher excitation densities, bimolecular ($\propto n^2$) processes such as non-geminate free electron-hole recombination dominate, which is particularly prevalent in low E_b materials. Despite their soft ionic structure, LHPs exhibit comparable bimolecular recombination rates to high-

performing covalent semiconductors such as GaAs.[136] This has been attributed to the aforementioned polaron screening, which may even make electron-hole interactions repulsive at short-range.[199] For excitonic systems, high excitation densities can give rise to non-radiative exciton-exciton annihilation, wherein the energy released by the decay of one exciton is transferred to another nearby.

At the highest free carrier densities, Auger recombination may dominate which (analogous to exciton-exciton annihilation) involves the transfer of energy from a non-geminate electron-hole pair to a nearby third carrier, and is therefore trimolecular ($\propto n^3$). While the excitation densities required are not particularly relevant to the operation of a SC under 1-Sun illumination, they can be routinely achieved using pulsed lasers and so often require separation from other processes of interest in spectroscopic measurements. Higher order recombination processes tend to be faster, and can be discerned by their dependence on the intensity of the light source used.

Stimulated emission (SE) occurs when the presence of a photon of suitable energy and phase initiates the radiative recombination of a carrier. This becomes more apparent as the ES population approaches that of the ground state (GS), and is the basis of the operation of the laser described in Section 3.1.

2.5 Defects and trapping

The solid state theory introduced thus far is built upon the assumption of an infinite periodic array of atoms. However, the structure of any real solid invariably contains interruptions to this otherwise perfect crystal structure, termed *defects*.[200] As summarised schematically in Figure 2.7, these may come in the form of 'point defects' due to an atom not residing in its intended lattice site; or larger scale defects such as grain boundaries, where the atoms at the surface of a crystal experience a different chemical environment to those in the bulk. If the energy levels that arise from these defects lie between bands, they can act as *traps* which localise charge carriers, shortening their lifetime and preventing them from doing useful work. In general, this is detrimental to PV device performance and much effort goes into minimising trap state density through careful fabrication methods (although they can also be beneficial where a short

carrier lifetime is required, such as in fast-switching diodes).[201]

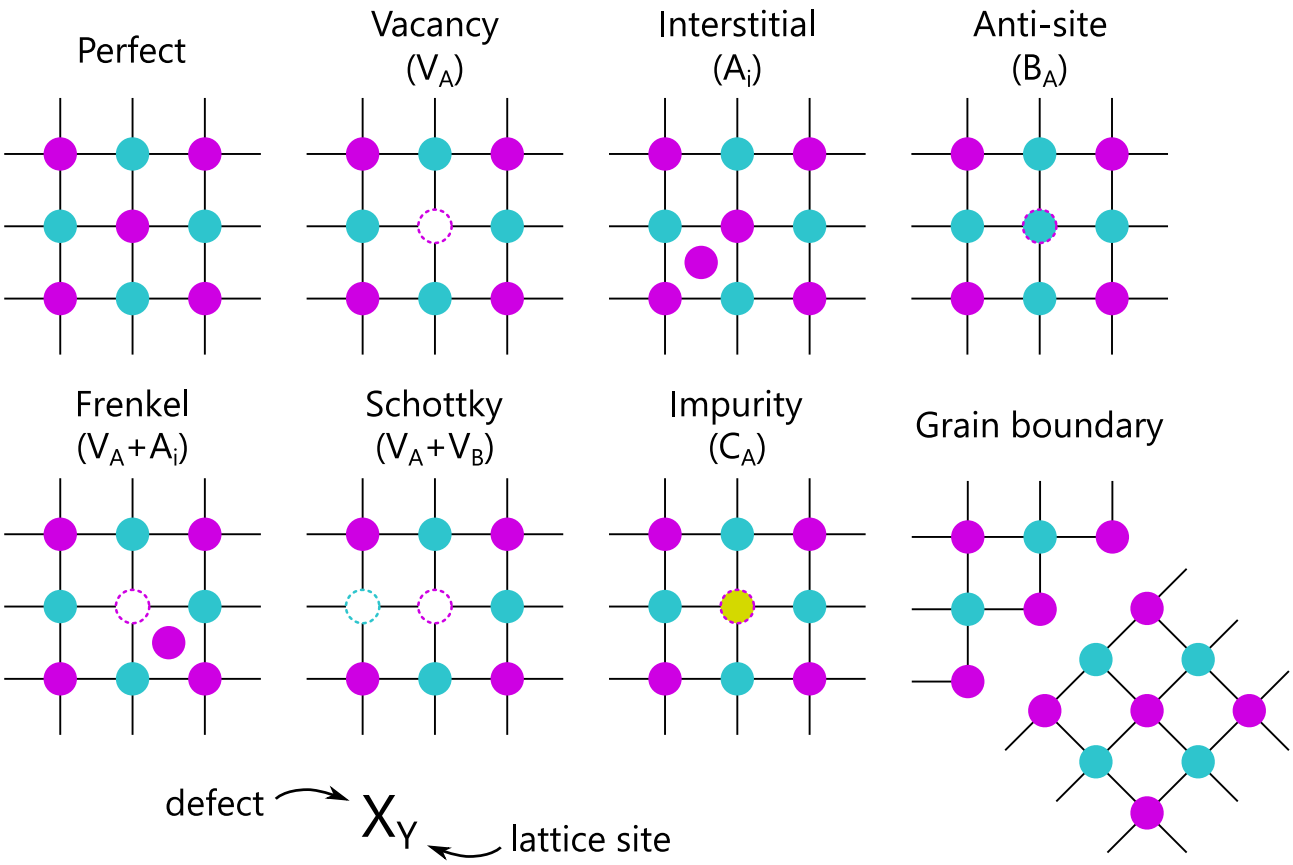


Figure 2.7 – Schematic diagram showing different types of defects, adapted from Ref. [200].

In contrast to traditional inorganic semiconductors such as c-Si and GaAs, the low-temperature fabrication methods used for LHPs endows them with a much higher defect density.[82] However, these seemingly do not impede their optoelectronic properties owing to their reported *defect tolerance*, which is said to arise from their unique band structure. Most semiconductors have a valence band maximum (VBM) mainly comprised of bonding MOs, and a conduction band minimum (CBM) comprised of antibonding MOs. As a result, any defect likely gives rise to non-bonding orbitals which lie *between* bands, forming trap states (Figure 2.8a). However, early calculations on LHPs suggested that the dominant defect type instead results in states that are buried *within* bands (Figure 2.8b) for the following reasons: (i) the VBM is mainly comprised of antibonding states formed by the hybridisation of Pb($6s$) and X(np) AOs, meaning VB vacancies are buried within the band; (ii) vacancies that would otherwise form 'shallow' traps just below the CB, are instead buried due to relativistic effects on the Pb($6p$) AO that lower the energy of the CBM;[202] and (iii) anti-site and interstitial defects that form 'deep' traps,

have a high formation energy and therefore only exist in low concentrations.[203,204]

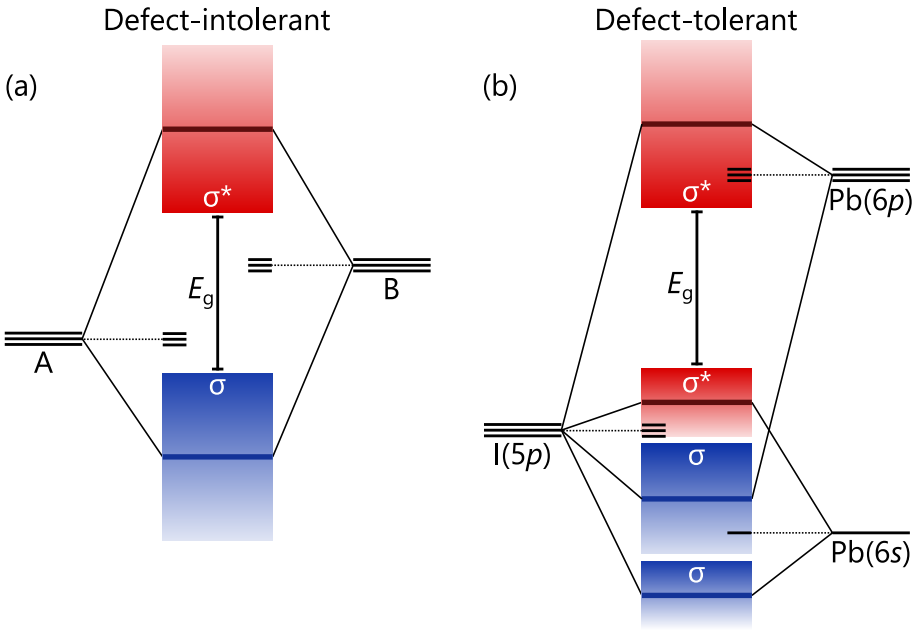


Figure 2.8 – (a) Defect intolerance in conventional semiconductors. (b) Defect tolerance in LHPs arises from the antibonding (σ*) nature of the VBM, meaning dangling bonds formed by vacancies are buried within the band. Adapted from Refs. [202] and [205].

The surface atoms form a much larger proportion of nanoscale structures and thus often have a sizable impact on their properties. Defect tolerance has also therefore been invoked to explain the promising properties of LHP NCs, which often demonstrate a high photoluminescence quantum yield (PLQY) from solution-based methods, without the need to resort to complicated core-shell architectures seen in traditional analogues.[205] In analogy to the predictions for bulk LHPs, interstitial atoms may be the only defect found in significant concentrations due to their low formation energy, but tend to form shallow traps.[206] The defect tolerance of LHP NCs is still somewhat controversial. For example, it was recently posited that extrapolation from bulk-like arguments is dubious because under-coordinated AOs experience a different electrostatic environment at the surface that may push their energies into the band gap.[207] The defect tolerance of LHP NCs, extended to its role on hot carrier dynamics, will be the subject of Chapter 5.

3 Methods

The utility of LHPs as optoelectronics is predicated on their electronic transitions being optically allowed. By the same token, their interaction with light can therefore be used as a powerful tool to probe their underlying electronic structure through spectroscopic methods. As described in Chapter 2, a material's characteristics is governed by dynamical processes and thus *time-resolved* methods are required to study them. The most fundamental light-matter interactions in LHP systems occur in transiting charge-carriers *between* bands and therefore visible light is commonly used. However, by employing NIR light, the *intraband* structure can be assessed and used to elucidate device-limiting processes. Furthermore, THz radiation can be used to study lattice dynamics in response to electronic excitation. The central theme for the approach used in this work is based on ultrafast intraband spectroscopy, expanded to multi-pulse approaches which can manipulate, and therefore study, sequences of distinct ESs.

3.1 Basic principles of a laser

As described in Section 2.2 and depicted in Figure 3.1, the transition rate between two states ("0" and "1") depends on their relative populations. Thus, at thermal equilibrium where, by definition, the lower state is more highly populated, a photon traversing a medium is more likely to be absorbed than to stimulate emission of another photon. The net result is that the incident radiation is attenuated. For a medium to amplify a light source, a *population inversion* must be formed wherein the higher-lying state is more highly populated. This is infeasible for a two-level system because, at best, $r_{0\to1} = r_{1\to0}$.[208]

In a three-level system, another energy level ("2") is introduced which can rapidly depopulate – and has a longer lifetime than – state 1, establishing a population inversion between 0 and 2. The first working example of a laser by Maiman in 1960[209] made use of ruby ($Cr:Al_2O_3$) as the lasing medium, which amplified light of ~690 nm. This was later expanded to four-level systems, such as in Nd-doped yttrium aluminium garnet (Nd:YAG) lasers, which can also more effectively depopulate the lower energy state ("3"), improving lasing efficiency.[210]

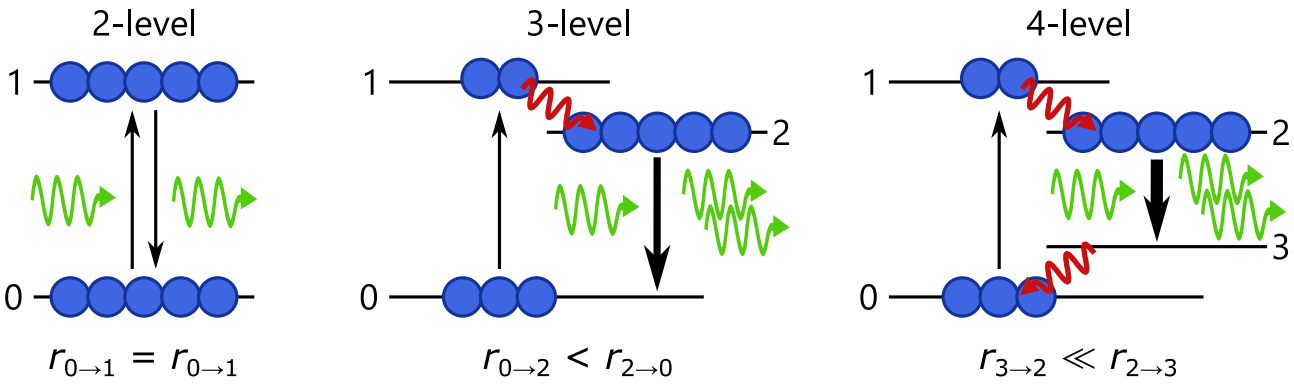


Figure 3.1 – Lasing requires a population inversion to be achieved via a multi-level system.

In a working laser, a 'cavity' is formed by placing the active medium between two mirrors with near-unity reflectance at the desired wavelength. A pump source is required to establish a population inversion in the active medium, and can be electrical or optical (e.g. an intense 'flash lamp' or, indeed, another laser) in nature. The nascent emitted light makes many passes between the two cavity mirrors, wherein the constructive interference of the travelling photons forms standing waves if the wavelength matches the cavity modes ($n\lambda = 2L$, where n is an integer and L is the cavity length), being amplified with each pass. A greater number of modes satisfy this relationship with a wider emission line and longer cavity. As the laser operates on the basis of SE, the emitted light has a high degree of spatial coherence, producing beams with low divergence that can be sent over long distances in the laboratory without loss in intensity.

While lasing can occur continuously over time, in this case only a small population inversion is sustained and the laser power remains relatively low. The peak amplification can be much greater if lasing is forced into brief bursts. One method of doing so is *Q-switching*, wherein the exit mirror is initially made transparent (low Q) such that optical feedback is suppressed and a high population inversion can be created by the pump; the mirror is then made reflective (high

Q) and lasing occurs rapidly from far above the gain threshold, producing short and intense light pulses. This is typically achieved using a shutter or electro-optic modulation of the cavity mirror, producing light pulses a few nanoseconds in duration.[210]

While the pulse duration achieved through Q-switching is limited by the lifetime of the emitting state and the rate of the modulating bias, few-femtosecond pulses can be produced through *mode locking* in the laser cavity. As per the Fourier transform described in Section 3.3.3, bringing modes spanning a wide range of frequencies into phase results in amplified pulses that are short in duration. This is readily achieved in titanium-doped sapphire (Ti:Al_2O_3, Ti:sapphire) lasers, whose Ti^{3+} ion dopants offer a very large gain bandwidth, generally centred at ~800 nm. The Ti:sapphire medium also affords the additional benefit of passive mode locking via the Kerr lensing effect, wherein the refractive index change is non-linear in intensity and thus self-focuses only the most intense modes.

A critical issue with the generation of ultrashort light pulses is degradation of the active medium due to extremely high peak irradiance. This can be circumvented by the use of *chirped-pulse amplification* first described by Strickland and Mourou in 1985,[211] wherein light is first stretched temporally by dispersive optics prior to amplification, before being re-compressed to afford high intensity, ultrashort laser pulses (Figure 3.2). This has since permitted the development of table-top ultrafast laser systems that pervade much of research and industrial applications.

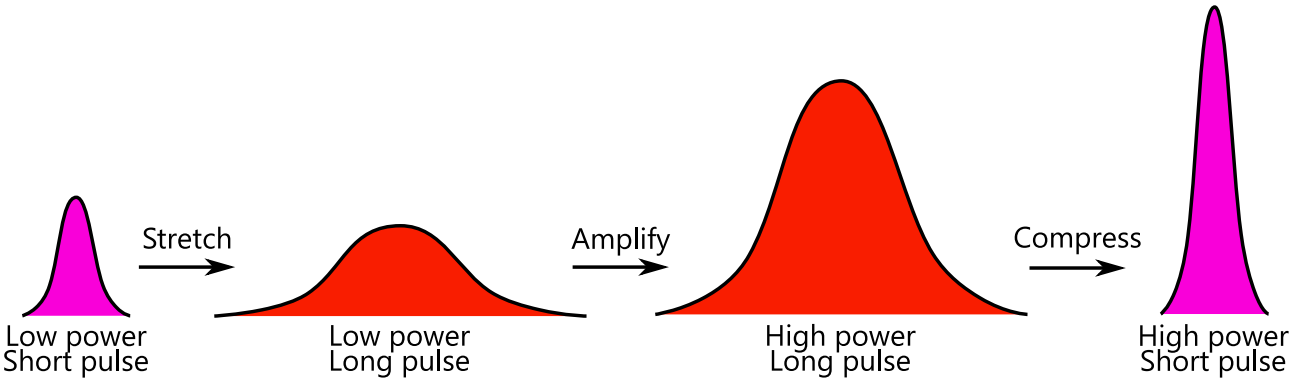


Figure 3.2 – During chirped pulse amplification, ultrashort, low power pulses are temporally stretched prior to amplification, before being re-compressed to produce ultrashort, high power pulses.

Key to their utility in the laboratory is the ability to manipulate the wavelength of light emitted

by a laser source. This can be achieved through the use of non-linear optics, involving multiple simultaneous light-matter interactions. For example, optical parametric amplifiers (OPAs) generate two low-energy photons – termed the 'signal' and 'idler' – from a single higher-energy 'fundamental' input. For the experiments described later, this is used to down-convert the 800 nm Ti:sapphire laser emission into NIR photons then used to probe intraband dynamics. Through up-conversion, two lower-energy photons can be used to produce a single higher-energy photon, for example in the generation of visible light used to initiate band-to-band transitions. Focusing an ultrashort narrowband laser pulse can also lead to 'self-phase modulation', thereby generating broadband white light.

3.2 Steady-state methods

3.2.1 Ultraviolet-visible absorption spectroscopy

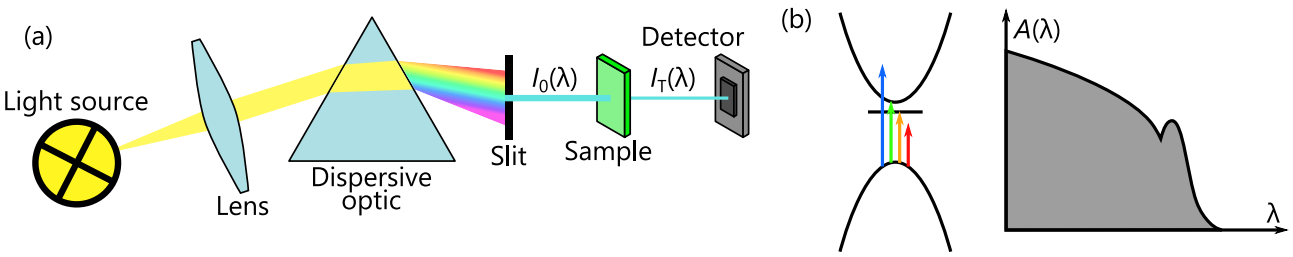


Figure 3.3 – (a) Schematic diagram of a UV-vis absorption spectrometer. (b) Schematic example of LHP UV-vis absorption spectrum.

As described in Section 2.2, a photon is only absorbed when its energy matches that of a transition between two quantum states of the material. Under equilibrium conditions, this corresponds to transitions from the material GS to higher-energy ESs. Many of the optoelectronic materials described in this thesis interact with light spanning the ultraviolet-visible (UV-vis) portion of the electromagnetic spectrum. As such, UV-vis absorption spectra are a central pillar in their characterisation, yielding insight on their electronic structure through widely available instruments.

The material's attenuation of a particular wavelength of light is assessed by comparing the incident light intensity (I_0) with that transmitted through the sample (I_T). The two values are

related to *absorbance* (or equivalently, optical density, OD) by the following equation:

$$A(\lambda) = \mathrm{OD}(\lambda) = -\log \frac{I_T(\lambda)}{I_0(\lambda)} \tag{3.1}$$

In practice, this is generally achieved using a white light source (e.g. Xe lamp), with the wavelength of light selected by combining a dispersive optic and a thin slit. Rotating the optic or translating the slit alters the wavelength of light impinging on the sample, and an absorbance spectrum can be generated. The width of absorption features correlates with the vibrational coupling to the electronic states involved and/or, in the case of LHP NCs, crystallite size dispersion across the sample.

3.2.2 Photoluminescence spectroscopy

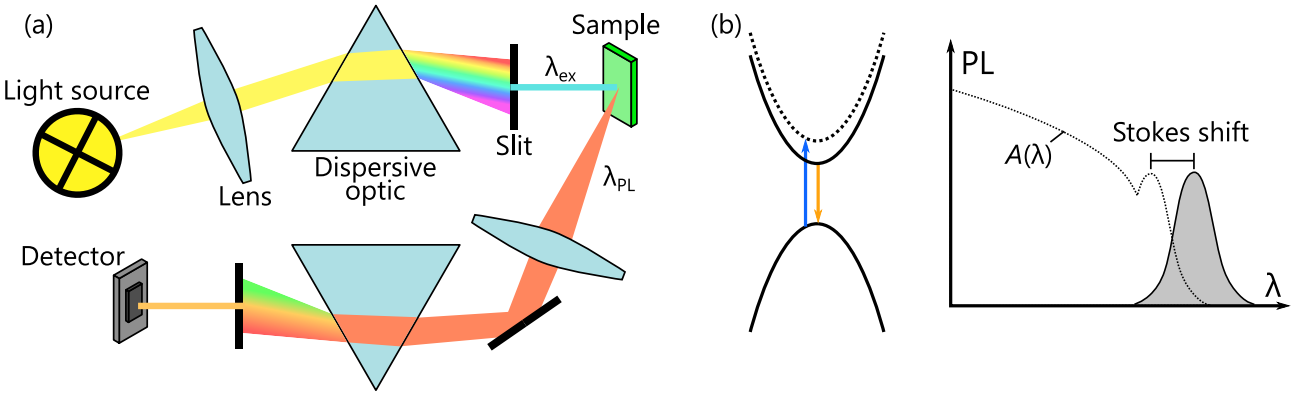


Figure 3.4 – (a) Basics of a PL spectrometer. (b) Schematic example of LHP PL spectrum.

While steady-state absorption spectra describe transitions from the GS, initial insight into the fate of a particular ES can be extracted from a material's emission spectrum. The emission of light from an ES can follow energy transfer via a chemical reaction (chemiluminescence) or electrical bias (electroluminescence), however emission following light absorption (*photoluminescence*, PL) is the most instructive for the systems described in this thesis.

Typically, a monochromatic light source (e.g. a laser, LED or a broadband source in combination with a monochromator, as in Section 3.2.1) is used to excite the sample. The resulting PL spectrum is generated by scanning the detection wavelength, either through another monochromator paired with a photodiode (PD), or a wavelength-calibrated pixel array (i.e. a camera).

While absorption can occur from any GS to any ES, emission predominantly occurs from the lowest-lying ES, according to Kasha's rule.[212] In LHPs, the *Stokes shift* between the absorption onset and PL maximum is thought to arise from lattice relaxation around the carrier (polaron formation) after excitation,[213] in analogy to the solvent reorganisation energy exhibited by isolated molecules.[214] The widths of the PL peaks, as in absorption spectra, are also related to (in)homogeneous broadening.

The PLQY (ϕ_{PL}) of a material can give initial insight into the relative efficiencies of its underlying radiative (k_{r}) and non-radiative (k_{nr}) processes:

$$\phi_{\mathrm{PL}} = \frac{k_{\mathrm{r}}}{k_{\mathrm{r}} + k_{\mathrm{nr}}} \tag{3.2}$$

For example, carrier trapping at defects lowers PLQY, which can be used to assess characteristics of a sample such as grain boundaries of polycrystalline films or the passivation of NC surfaces. As PL is a spontaneous process, emission occurs in all directions and thus PLQY measurements benefit from the use of an integrating sphere to capture all of the nascent light.

3.3 Pump-push-probe (PPP) spectroscopy

In the study of ES dynamics in optoelectronics, a very commonly applied variant of the PP scheme is transient absorption spectroscopy (TAS). Here, the system is pumped into an ES, and then probed by a broadband (usually visible) light source. The differential absorption spectrum with (A_{on}) and without (A_{off}) the pump can be used to investigate a wide range of overlapping ES species:[198,215]

$$\Delta A(t,\lambda) = A_{\mathrm{on}}(t,\lambda) - A_{\mathrm{off}}(\lambda) \tag{3.3}$$

$$= -\log \frac{I_{\mathrm{T,on}}}{I_0}(t,\lambda) + \log \frac{I_{\mathrm{T,off}}}{I_0}(\lambda) \tag{3.4}$$

$$= -\log \frac{I_{\mathrm{T,on}}(t,\lambda)}{I_{\mathrm{T,off}}(\lambda)} \tag{3.5}$$

Transient absorption (TA) features for LHPs can be broadly classified into three types:

- Ground state bleach (GSB), $\Delta A < 0$:

  When the pump is absorbed by the sample, electrons transit from the GS to an ES and the GS is "bleached". The sample is therefore rendered *more* transmissive to the probe, which is manifested as a negative feature in the TA spectrum at the steady-state absorption edge.

- Stimulated emission (SE), $\Delta A < 0$:

  Following pump excitation, the probe may stimulate emission from the ES to the GS. This results in additional light intensity at that wavelength reaching the detector, and a negative feature in the TA spectrum near the steady-state PL peak.

- Photoinduced absorption (PIA), $\Delta A > 0$:

  The population of an ES by the pump means the subsequent probe can transit carriers to an otherwise inaccessible higher-lying ES, rendering the sample *less* transmissive to the probe at those energies and yielding a positive feature in the TA spectrum.

The wide number of spectrally and temporally overlapping features in a TA spectrum can complicate their interpretation. For example, the presence of band-edge carriers in the CB can *increase* the band gap energy through the 'Burnstein-Moss effect',[216] resulting in a blue-shifted GSB; conversely, the photoinjection of carriers into the CB has also been shown to *decrease* the band gap via 'band gap renormalisation' (BGR).[180] The competition between these effects is sample-dependent and thus the net effect can be hard to predict *a priori*. Debate over the effects of photoinduced refractive index changes can also obfuscate the interpretation of results.[217]

BGR leads to a sub-gap PIA feature in the TA spectra which, after above-gap photoexcitation, diminishes as the hot carriers cool and fill these band-edge states. As such, tracking the changes in this sub-gap PIA is one method employed to study hot carrier dynamics.[218,219] Another approach is by following the early-time rise in the band-edge kinetics: under resonant conditions, the band-edge states are filled promptly within the pump pulsewidth; while under above-gap excitation, the GSB onset is delayed by hot carrier cooling.[220]

By far, the most common approach to studying hot carrier dynamics is through the *shape*

of the GSB after above-gap excitation.[180,184,221–225] After thermalisation, the carriers form a pseudo-Fermi energy distribution and this is manifested as a high-energy tail in the GSB. Fitting this tail yields an effective carrier temperature whose evolution over time relates to hot carrier cooling. Due to spectral overlap with other features, the inherent difficulty with this approach is that the fitted region cannot be assigned solely to the presence of hot carriers and there is not a definitive method for choosing the relevant spectral window, potentially yielding inconsistent results.[226] Moreover, the definition of an effective temperature is somewhat unclear at low carrier densities[227] and/or in quantised band structures such as those in NCs.[228] More elaborate methods that take into account a wider range of spectral contributions have now been developed by Sum *et al.*[226]

The vast majority of hot carrier studies are based on a PP scheme with all carriers produced by a single common excitation event. Increasing the pump fluence increases the initial carrier density, leading to longer cooling times via the hot phonon bottleneck effect (Section 2.3). However, higher carrier density also leads to a higher likelihood of Auger recombination (Section 2.4), during which hot carriers are formed as a by-product. The 'intrinsic' hot carrier lifetimes typically fall on sub-ps timescales, and Auger recombination >10 ps. Therefore, the hot carrier lifetime falls into two distinct regimes of intraband cooling and 'Auger heating', with the relative contributions of each difficult to disentangle at intermediate excitation densities. In this regard, three-pulse 'pump-push-probe' (PPP) spectroscopic approaches described herein offer more rigorous control of hot carrier density.

The PPP scheme was first used by Guyot-Sionnest *et al.* in 1999.[193] Here, a visible pump was used to excite CdSe QDs, and their ES dynamics probed by a NIR pulse tuned to the $1S$-$1P$ transition. A third, more intense NIR pulse arrived ∼10 ps after the pump, ensuring it interacted exclusively with the lowest-lying ES ($1S$), bleaching the probe absorption by re-excitation to the $1P$ state. The recovery of the probe absorption could be solely assigned to the intraband relaxation from $1P$ to $1S$, and used to elucidate the role of Auger-type electron-hole energy transfer in overriding the phonon bottleneck. Klimov *et al.*[229] later used a similar scheme for CdSe QDs capped with a hole acceptor. By introducing the push at later delays after

the pump, a larger proportion of holes became spatially decoupled from the electrons, prolonging intraband relaxation by suppressing electron-hole energy transfer. PPP spectroscopy was also then used elsewhere in other notable works on CdSe QDs,[195,196] and expanded to PbSe[230] and InP[194] QDs soon after.

Variants of PPP spectroscopy have now recently been applied to LHPs.[231–239] In the following Sections, the optical setups and analysis procedures used to obtain the results presented in Chapters 4-6 are described in detail.

3.3.1 Pump–push–NIR-probe (PPP-NIR) spectroscopy

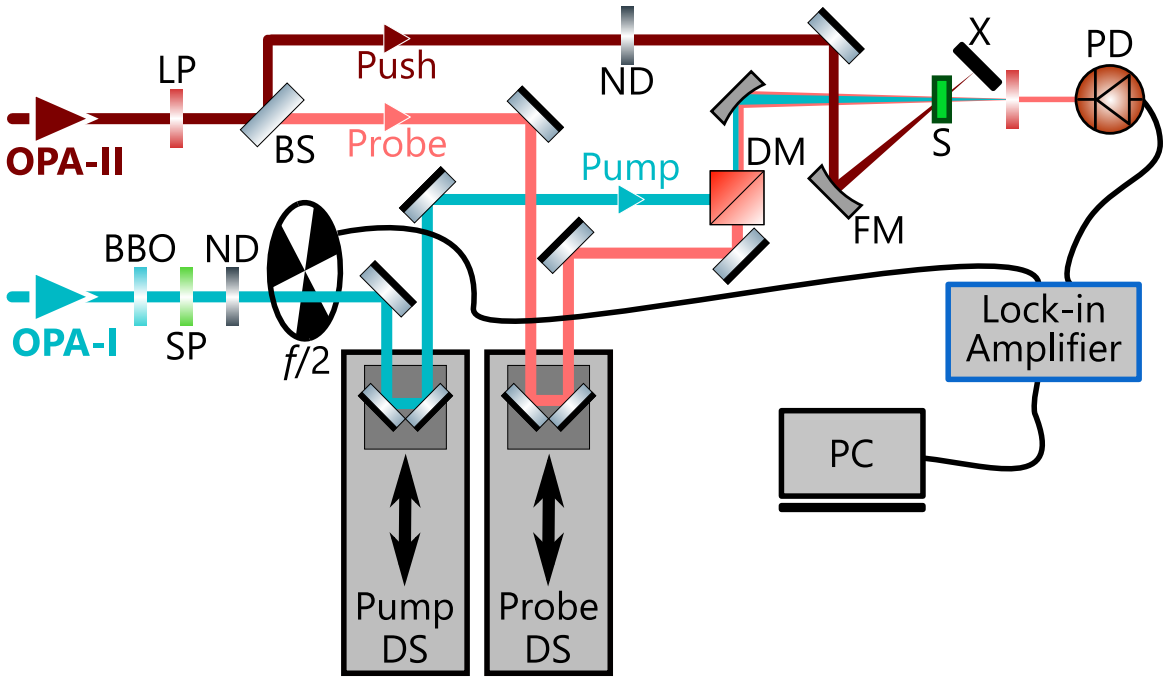


Figure 3.5 – Schematic diagram of PPP-NIR setup. BBO: β-barium borate; BS: beamsplitter; DM: dichroic mirror; DS: delay stage; FM: focusing mirror; LP: long-pass filter; ND: neutral density filter; OPA: optical parametric amplifier; PD: photodiode; S: sample; SP: short-pass filter; X: beam-block.

The output ($\lambda_c \sim 800$ nm, $\tau \sim 35$ fs, $f = 4$ kHz) of a Ti:sapphire regenerative amplifier (Astrella, Coherent) seeds two OPAs (TOPAS Prime, Light Conversion) for tunable-wavelength NIR light generation. TOPAS-I light is further upconverted (by frequency-mixing or second harmonic generation (SHG)) in a β-barium borate (BBO) to produce a visible pump with $h\nu \sim E_g$. This then passes through a mechanical chopper modulated at $f/2 = 2$ kHz, an

optical delay line (controlling the pump-push time delay), and a neutral density (ND) filter wheel on its path to the sample. TOPAS-II light is tuned to a wavelength within the range of *intra*band transitions, and split by a R:T=10:90 beamsplitter. The more intense portion forms the push and passes through a separate ND filter wheel; while the other arm forms the probe and is sent through another optical delay line (controlling pump(-push)-probe time delay). Pump and probe are introduced collinearly at the sample via a 100 mm focusing mirror; with the off-axis push superimposed via a 300 mm focusing mirror – the position of which is moved to achieve a fluence that gives sufficient signal-to-noise, with minimal sample degradation. The probe is detected by an amplified PbSe PD (PDA20H-EC, Thorlabs), and the differential signal read-out to a lock-in amplifer (MFLI, Zurich Instruments).

3.3.2 Pump–push–Visible-probe (PPP-Vis) spectroscopy

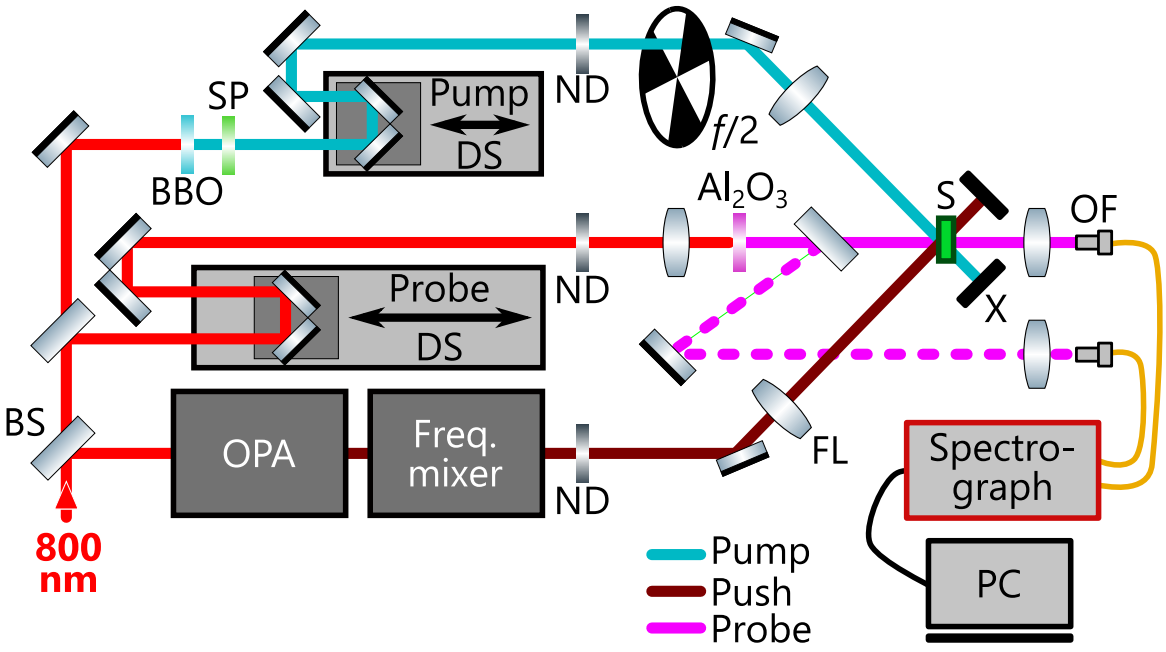


Figure 3.6 – Schematic diagram of PPP-Vis setup. BBO: β-barium borate; BS: beamsplitter; DS: delay stage; FL: focusing lens; ND: neutral density filter; OF: optical fibre; OPA: optical parametric amplifier; S: sample; SP: short-pass filter; X: beam-block.

All measurements were performed using a commercially available setup (Helios, Ultrafast Systems) with home-built adaptations for three-pulse experiments. The output ($\lambda_c \sim 800$ nm, $\tau \sim 100$ fs, $f = 1$ kHz) of a Ti:sapphire regenerative amplifier (Solstice, SpectraPhysics) is split into three arms. One arm seeds an OPA (TOPAS Prime, Light Conversion) and a frequency

mixer (NirUVis, Light Conversion) to produce a NIR push, where it passes through a variable ND filter before being focused onto the sample. The second arm of seed laser light is coupled into an optical delay line which ultimately controls the pump(-push)-probe delay time, before then being focused into a sapphire crystal to generate the broadband visible probe. The probe is collimated before it then passes through a beamsplitter to form the 'sample' and 'reference' beams. While the reference is focused directly into an optical fibre, the sample probe is first re-focused onto a spot on the studied system, before the transmitted probe is passed into a second optical fibre. Next, the light passes through a dispersive optic to spatially separate it according to wavelength. The dispersed light impinges on a camera, whose pixel positions are calibrated to probe wavelength. The use of sample and reference beams means shot-to-shot laser instability is accounted for and the resulting data are less noisy. The third arm of the seed laser passes through a BBO to generate a 400 nm pump, where it makes a double pass through a retroreflector mounted on a translation stage whose position controls the resulting pump-push delay. The pump is chopped at $f/2 = 500$ Hz before being focused onto the sample.

Introduced in Section 3.1, the *chirp* experienced by a laser pulse means that longer-wavelength probe photons arrive at the sample fractionally earlier than those of shorter wavelength. As a result, the '*time-zero*' position of maximum temporal overlap with the pump is wavelength-dependent and chirp-correction needs to be performed on any TA surface prior to data analysis. This is done by hand-picking a selection of (t, λ) points corresponding to the half-rise of the kinetics at that wavelength. A polynomial is fitted to these points and subtracted from the data set, such that the half-rise occurs consistently at time-zero across all parts of the spectrum. Any residual 'pre-pump' ($t < 0$) signal amplitude is also background subtracted to ensure only ES dynamics are present. These corrections are made in the *Surface Xplorer* software package (Ultrafast Systems).

For PPP-Vis experiments, the kinetics are integrated over a wavelength range slightly to the low-energy side of the GSB maximum. This is to minimise the effect of spectral line shape change of the high-energy GSB tail due to the presence of hot carriers upon push re-excitation, as described earlier; while also ensuring minimal contamination from the sub-gap PIA feature.

The initial carrier density ($\langle n \rangle$) can be calculated from the pump conditions as follows:

$$F_{\text{pump}} = \frac{E_{\text{pump}}}{\pi R^2/2} \tag{3.6}$$

$$\langle n \rangle = (1 - 10^{-A}) \times F_{\text{pump}} \tag{3.7}$$

where E_{pump} is the pump energy per pulse, R is the pump beam radius of ∼250 µm, A is the sample absorbance at the pump wavelength.

The average cold carrier density immediately prior to the push, and the hot carrier density immediately following the push, can be calculated as follows:

$$\langle n_{\text{cold},0} \rangle = \langle n \rangle \times \frac{\Delta A_{\text{GSB,pre-push}}}{\Delta A_{\text{GSB,max}}} \tag{3.8}$$

$$\langle n_{\text{hot},0} \rangle = \langle n_{\text{cold},0} \rangle \times \frac{|\delta(\Delta A_{\text{PPP}})|}{\Delta A_{\text{PP}}} \tag{3.9}$$

3.3.3 Pump–push–THz-probe (PPP-THz) spectroscopy

The PPP-THz optical setup, electronics and *LabVIEW* control software were built by Dr. Xijia Zheng and Dr. Andrei Gorodetsky (Imperial College London). The output ($\lambda_c \sim 800$ nm, $\tau \sim 35$ fs, $f = 4$ kHz) of a Ti:sapphire regenerative amplifier (Astrella, Coherent) is first aligned through a pair of cage-mounted irises, which makes alignment of the entire setup more facile. The 800 nm beam is split, with one portion forming the THz probe, and the other the 'gate'. THz radiation is generated by defocusing 50 mW of 800 nm light through a photoconductive antenna (PCA, Tera-SED, Laser Quantum) with a pulsed bias ($f = 2$ kHz, $V = 40$ V) applied by an external power supply (2231A-30-3, Keithley)–microcontroller (Arduino) pair. The THz probe is focused onto the sample using parabolic mirrors, with the transmitted light collected at a ZnTe crystal. The gate pulse initially passes through an optical delay line, before overlapping with the transmitted THz at the ZnTe crystal. The THz waveform is produced via electro-optic sampling – that is, the presence of the THz induces a rotation of the 800 nm gate electric field vector. The extent of rotation determines the relative magnitudes of the *s*- and *p*-polarised vector components, which are separated by a Wollaston prism before each are detected by a

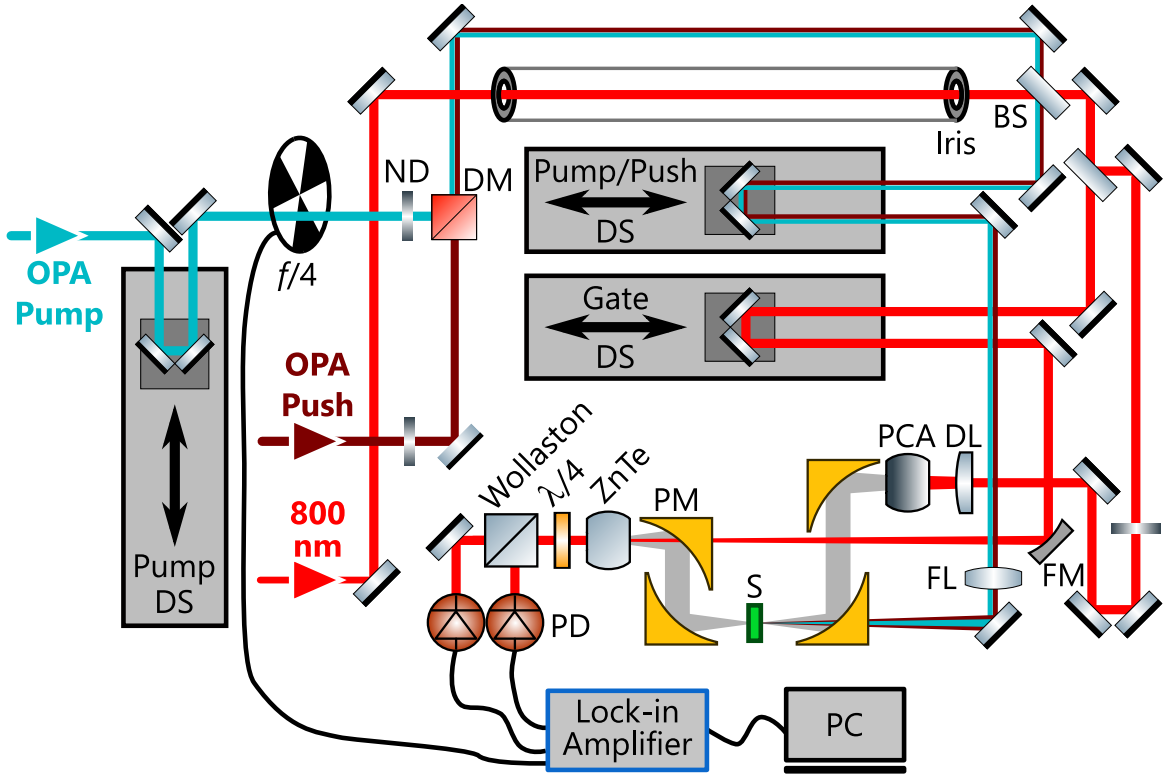


Figure 3.7 – Schematic diagram of PPP-THz setup. BS: beamsplitter; DL: defocusing lens; DM: dichroic mirror; FL: focusing lens; FM: focusing mirror; OPA: optical parametric amplifier; PCA: photoconductive antenna; PD: photodiode; PM: parabolic mirror; S: sample; λ/4: quarter-waveplate.

pair of PDs. The PDs are 'balanced' under zero THz field by rotating a quarter-waveplate mounted on the ZnTe crystal. Thus during data acquisition, the *difference* in signal between the PDs, as read out to a lock-in amplifier (MFLI, Zurich Instruments), is related to the THz field amplitude. By controlling the THz-gate delay, the time-varying THz waveform can be extracted (Figure 3.8).

The time- to frequency-domain conversion of the THz waveform is achieved via *Fourier Transformation*, the basic principles of which are described further here. It can be shown that any continuous function may be represented by an infinite sum of sine and cosine waves:[240]

$$f(x) = \frac{1}{2}a_0 + \sum_{n=1}^{\infty} a_n \cos(nx) + \sum_{n=1}^{\infty} b_n \sin(nx) \tag{3.10}$$

$$= \sum_{n=-\infty}^{\infty} A_n \, e^{inx} \tag{3.11}$$

Here, Equations 3.10 and 3.11 are the sine-cosine and complex forms of the Fourier *series*,

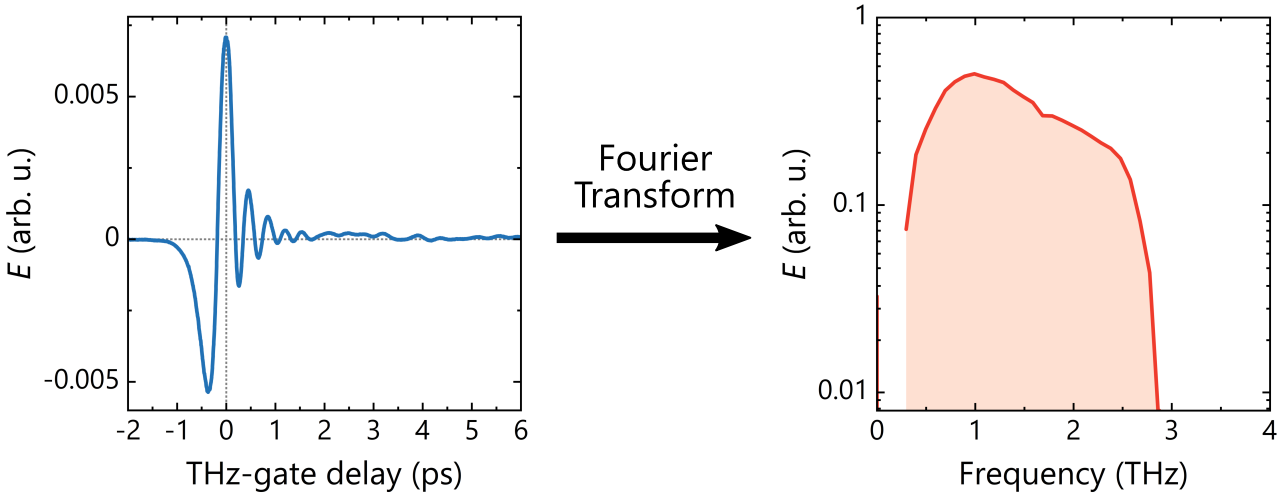


Figure 3.8 – Time- to frequency-domain conversion of THz spectrum via Fourier transformation

respectively, where:

$$a_n = \frac{1}{\pi}\int_{-\pi}^{\pi} f(x)\cos(nx)\,\mathrm{d}x$$
$$b_n = \frac{1}{\pi}\int_{-\pi}^{\pi} f(x)\sin(nx)\,\mathrm{d}x$$
$$A_n = \frac{1}{2\pi}\int_{-\pi}^{\pi} f(x)\,e^{-inx}\,\mathrm{d}x$$

For a function that is periodic in $[-L/2, L/2]$, Equation 3.11 can be written as:[241]

$$f(x) = \sum_{n=-\infty}^{\infty} A_n\,e^{2\pi inx/L} \tag{3.12}$$

The Fourier *transform* is a case of the Fourier series where $L \to \infty$ and the discrete A_n is replaced by the continuous $\hat{f}(k)\,\mathrm{d}k$ with $n/L \to k$, to give the relationship between a conjugate pair of functions, f and $\hat{f}$:

$$f(x) = \int_{-\infty}^{\infty} \hat{f}(k)\,e^{2\pi ikx}\,\mathrm{d}k \tag{3.13}$$
$$\hat{f}(k) = \int_{-\infty}^{\infty} f(x)\,e^{-2\pi ikx}\,\mathrm{d}x \tag{3.14}$$

where x and k are the *reciprocal domains* in which each function operates. Schematically, this

amounts to finding the average amplitude ($\hat{f}$) of an input signal (f) after rotation through the *complex plane*, where $\hat{f}$ will only be non-zero when the frequency of rotation (k) matches a component of the input signal.

Any signal that is non-zero in only a small region of one domain, is non-zero in a large region of its reciprocal domain. This has powerful and far-reaching implications for signal processing – most notably, in the context of this thesis, for the interconversion between the *time* and *frequency* domains of an electric field: as outlined in Section 3.1, for an optical pulse to be short in time duration, it must be comprised of photons spanning a broad range of frequencies (energies). The well-known *Heisenberg Uncertainty Principle* (Equation 3.15), which describes the fundamental limit of precision to which both the *position* (x) and *momentum* (p, "spatial frequency") of a particle can be known simultaneously, is also a direct consequence of Fourier transformation.

$$\Delta x \Delta p \geq \frac{h}{4\pi} \tag{3.15}$$

For PPP-THz measurements, the gate delay was fixed at the THz field maximum. TOPAS I (as in Section 3.3.1) is detuned to transmit as much of the 800 nm seed as possible, from which the 400 nm pump is generated via SHG in a BBO and residual seed light removed using a 450 nm shortpass filter (FESH0450, Thorlabs). The pump is mechanically chopped at $f/4 = 1$ kHz and passed into an optical delay line whose position is fixed to determine the pump-push delay. The NIR push is derived from either the 'signal' or 'idler' of TOPAS II, depending on the wavelength required, and made collinear with the pump before entering the THz setup. Figure 3.9 shows the measured signal spectrum, with the idler spectrum predicted from the energy difference between the signal and fundamental input, due to limited spectrometer bandwidth (950-1700 nm, Qneo, Broadcom). Both pump and push pass through another optical delay line to control pump(-push)-probe time delay. They are then focused through a lens onto the sample. The intensity of the pump and push are separately controlled by continuous variable ND filters.

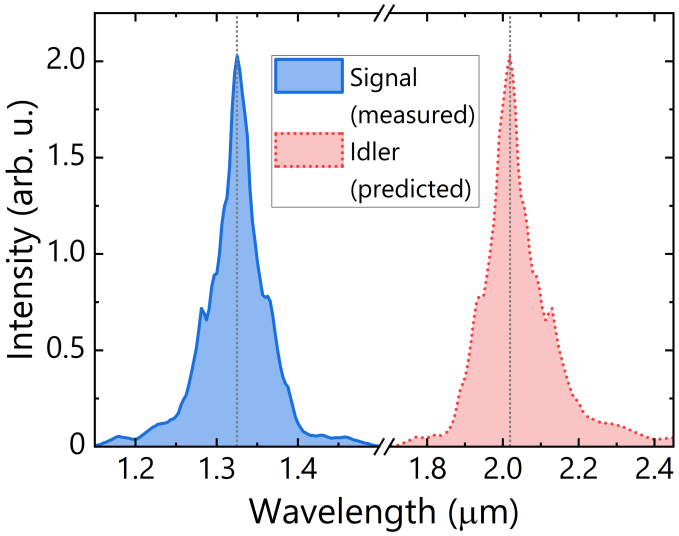


Figure 3.9 – Push spectra for PPP-THz. The signal is measured using a spectrometer; due to limited spectrometer bandwidth, the idler spectrum is predicted based on the signal.

3.4 Kinetic modelling

The kinetics of a photophysical species are defined in terms of the rate of change of their density with respect to time, the first-order derivative $\mathrm{d}n/\mathrm{d}t$. The kinetics often depend on multiple different interactions with (i) the environment; (ii) other members of the same species; and (iii) members of other species that have their own time-evolving population. This *system of coupled differential equations* therefore cannot be solved analytically and so numerical approximation methods are valuable in extracting physically meaningful parameters from the transient spectroscopic data.

The definition of the first derivative of a function $y(x)$, for a small step Δx, is:

$$\frac{\mathrm{d}y}{\mathrm{d}x} = y'(x) = \lim_{\Delta x \to 0} \frac{y(x + \Delta x) - y(x)}{\Delta x} \tag{3.16}$$

A subset of numerical approximations to differential equations, described herein, are based on the Taylor expansion:

$$y(x + \Delta x) = y(x) + \sum_{n=1}^{\infty} \frac{(\Delta x)^n}{n!} y^{(n)}(x) \tag{3.17}$$

The *Euler method* approximates $y(x)$ by truncating at the 1st term of the Taylor expansion:

$$y(x + \Delta x) \approx y(x) + y'(x)\Delta x \tag{3.18}$$

Adding successive terms in the expansion gives a better approximation of $y(x)$ but requires knowledge of the explicit form of its n^{th} derivative. The Runge-Kutta (RK) methods are based on the Taylor expansion but simplify computation by reducing higher order derivatives. The 2nd-order RK method has the form:

$$y(x + \Delta x) \approx y(x) + y'\left(x + \frac{\Delta x}{2},\, y(x) + y'(x)\frac{\Delta x}{2}\right)\Delta x \tag{3.19}$$

Geometrically, this amounts to propagating from $y(x)$ to $y(x + \Delta x)$ using the gradient at the point *halfway* between them $(x + \frac{\Delta x}{2},\, y(x + \frac{\Delta x}{2}))$, and is therefore also called the *Midpoint method*. As shown in Figure 3.10, this converges to $y(x)$ faster than the Euler method and so is more accurate, but marginally more expensive computationally, for a given Δx.

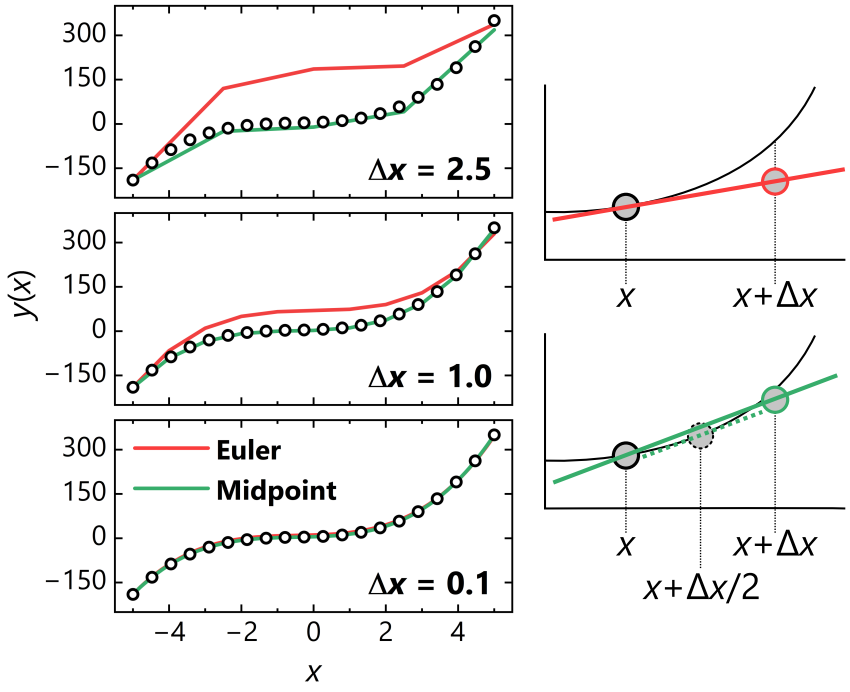


Figure 3.10 – Euler and Midpoint methods for the numerical approximation to the exemplar polynomial $y = 2x^3 + 3x^2 + 4x + 5$ (circles). The Midpoint method converges to $y(x)$ faster (i.e. at a larger step size Δx) than the Euler method.

Kinetic modelling of the experimental results was performed using custom-made Python codes

in interactive Jupyter Notebooks.

3.5 Exciton binding energy via Elliott model

E_b is an important parameter in characterising the nature of the ES present in a semiconductor. Multiple methods for calculating E_b are available, including temperature-dependent PL,[242–244] magneto-optical spectroscopy,[119,245,246] ellipsometry[247] and first-principles calculation.[248] Modelling steady-state absorption spectra using the Elliott formula is another common approach,[249–252] and is the one chosen here due to its accessibility. Modelling of absorption spectra was performed using custom-made Python code in interactive Jupyter Notebooks.

Within the Elliott model, the absorption spectra can be decomposed into a linear combination of exciton (α_x) and continuum (α_c) states:

$$\alpha(E) = \alpha_x(E) + \alpha_c(E) \tag{3.20}$$

where:

$$\alpha_x(E) = \left[A_x \sum_{n=1}^{\infty} \frac{1}{n^3} \cdot \delta\left(E - E_\mathrm{g} + \frac{E_\mathrm{b}}{n^2} \right) \right] + B_x\, \delta(E - E_2) \tag{3.21}$$

and:

$$\alpha_c(E) = A_c \cdot \theta(E), \qquad \theta = \begin{cases} \sqrt{E - E_g} & \text{for } E > E_\mathrm{g} \\ 0 & \text{for } E \leq E_\mathrm{g} \end{cases} \tag{3.22}$$

The sub-gap exciton states are modelled in the first term of Equation 3.21 by a series of delta functions at $E = E_\mathrm{g} - E_\mathrm{b}/n^2$ (which thus converge at E_g), with intensities that scale with $1/n^3$. As such, expanding the series to $n \lesssim 5$ is typically sufficient in practice. The second term of Equation 3.21 describes an exciton-like transition found above the band gap at $E = E_2$ in the more confined systems.

The continuum is modelled in Equation 3.22 as a Heaviside function, θ, that scales with $\sqrt{E - E_\mathrm{g}}$ above E_g, which assumes a parabolic band structure near the band edge.

A_x, B_x and A_c are scaling factors to fit the model to the experimental data. Line broaden-

ing due to static and dynamic disorder is modelled by convolving the exciton and continuum contributions with a Gaussian function, $G(E, \sigma)$. The final fitted spectra thus have the form:

$$\alpha_{\text{total}}(E) = [\alpha_x(E) * G(E, \sigma_x)] + [\alpha_c(E) * G(E, \sigma_c)] \tag{3.23}$$

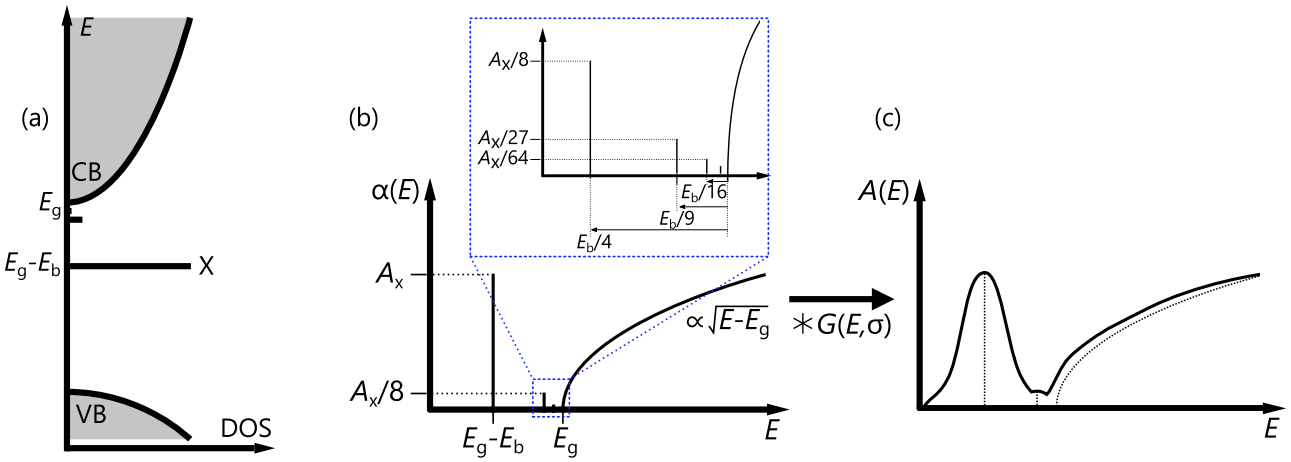


Figure 3.11 – The Elliott model assumes the band structure depicted in (a). The contributions of excitons and the continuum to absorption spectrum are depicted in (b). Gaussian convolution to account for line broadening yields modelled absorption spectrum depicted in (c).

4 Hot Carrier Confinement in Lead Halide Perovskite Nanomaterials

Thus far, the photophysics of LHPs and their nanomaterials have been introduced, with hot carrier cooling highlighted as an important energy loss pathway that warrants a thorough understanding for novel device design. Hot carrier cooling is governed by their interactions with the lattice and neighbouring carriers. Here, these are assessed in a range of nanomaterials using the first of three variants of the multi-pulse approach described in Chapter 3, where the use of a NIR probe directly interrogates intraband dynamics. Through this, it is shown that the carrier-carrier scattering pathway becomes more dominant in confined systems.

The contents of this Chapter are adapted from work described in Ref. [234]:
B. P. Carwithen, T. R. Hopper, Z. Ge, N. Mondal, T. Wang, R. Mazlumian, X. Zheng, F. Krieg, F. Montanarella, G. Nedelcu, M. Kroll, M. Albaladejo-Siguan, J. M. Frost, K. Leo, Y. Vaynzof, M. I. Bodnarchuk, M. V. Kovalenko, A. A. Bakulin, Confinement and Exciton Binding Energy Effects on Hot Carrier Cooling in Lead Halide Perovskite Nanomaterials, *ACS Nano*, **2023**, *17*, 6638–6648

4.1 Background and motivation

As discussed previously, the variety of potential applications for semiconductors has been greatly enhanced by the development of facile synthesis routes to quantum-confined structures. Naturally, understanding the underlying (photo)physics at play in these systems can help guide

their applicability.

The manner in which increased confinement affects hot carrier cooling dynamics in nanomaterials is still largely contested. Based on the phonon bottleneck picture, wherein the discretisation of electronic states requires that carriers relax via a multiphonon mechanism (Figure 2.4), cooling ought to be intrinsically slower[188] and exhibit a more severe hot phonon bottleneck in quantum-confined materials than their bulk analogues. Indeed, some early reports on GaAs showed slower cooling in QWs than bulk systems,[171,172,253] but cooling times were found to be similar elsewhere.[169] This was also contested on the grounds that any differences observed could instead be explained by the variation in carrier densities used for each.[254–256] In other words, this was a *hot* phonon bottleneck effect that should display a dependence on carrier density. Nozik *et al.*[257,258] would then later show that the hot phonon bottleneck is in fact stronger in QWs than in bulk GaAs.

Debate around the effects of confinement on hot carrier dynamics is also prevalent for LHP NCs. Sum *et al.*[259] showed that cooling times were longer in $MAPbI_3$ NCs – crucially also showing the protracted cooling process enabled efficient *extraction* of these carriers by a 4,7-diphenyl-1,10-phenanthroline acceptor. Conversely, Wu *et al.*[260] observed a subtle increase in cooling rate for progressively smaller $CsPbBr_3$ NCs; while Hodgkiss *et al.*[221] observed faster cooling in $CsPbBr_3$ NCs than the bulk yet with, intriguingly, no size-dependence between the ∼8 and ∼4 nm NCs despite clear spectral signatures of discrete states only appearing in the latter. A lack of observable difference between the cooling behaviour of bulk and nanocrystalline LHPs has also been reported elsewhere in the literature,[261,262] including in work by Hopper *et al.*[232] comparing bulk and 8 nm cuboidal $CsPbBr_3$ NCs. This may also be explained by considering the weak confinement experienced by the carriers in NCs of this size ($d_B \sim 7$ nm in $CsPbBr_3$[76]). In this latter work, achieved through the same pump–push–NIR-probe (PPP-NIR) scheme as used later in this Chapter, the hot carrier dynamics were shown to depend not only on the hot carrier density due to the hot phonon bottleneck, but also on the background cold carrier density. At higher cold carrier density, cooling was faster, which was attributed to an alternative cooling pathway mediated by the scattering of hot and cold carriers. This provides a key mechanistic

basis for the results described hereinafter.

In NPLs, whose anisotropic shape mean they are strongly confined in one dimension, carrier cooling has been shown to be density-independent and faster than in the bulk, which was attributed to a reduction in screening of carrier-phonon interactions.[263,264] Meanwhile, QW-type perovskites have seen contrasting reports of both faster[265,266] and slower[267,268] cooling with increased confinement.

In this Chapter, the hot carrier cooling dynamics in a range of LHP nanomaterials spanning weak to strong confinement regimes are systematically investigated by ultrafast PPP-NIR spectroscopy. The results reveal the effect of quantum confinement and highlight the importance of studying hot carrier density-dependence when making comparisons between the dynamics of different systems.

4.2 Specific experimental details

4.2.1 Sample preparation and characterisation

5 nm $CsPbBr_3$ NCs, prepared by Dr. Franziska Krieg (ETH Zurich)

Chemicals: Cs_2CO_3 (Fluorochem), $Pb(OAc)_2.3H_2O$ (99.99%), Br_2 (99.9%), 1-octadecene (ODE, technical grade), 3-(N,N-dimethyloctadecylammonio)propanesulfonate (ASC18, >99%), oleic acid (OA, 90%, Sigma-Aldrich/Merck), toluene, acetone (HPLC grade), ethyl acetate (HPLC grade, Fischer) and trioctylphosphine (TOP, >97%, STREM).

Cs-oleate precursor, 0.4 M in ODE: Cs_2CO_3 (1.628 g, 5 mmol), OA (5 mL, 16 mmol) and ODE (20 mL) were evacuated at 25–120 °C until gas evolution was complete.

Pb-oleate precursor, 0.5 M in ODE: $Pb(OAc)_2.3H_2O$ (4.607 g, 12 mmol), OA (7.6 mL, 24 mmol), and ODE (16.4 mL) were mixed in a three-necked flask and evacuated at 25–120 °C until complete evaporation of acetic acid and water.

TOP-Br_2 precursor, 0.5 M in toluene: TOP (6 mL, 13 mmol) and Br_2 (0.6 mL, 11.5 mmol) were mixed under an inert atmosphere. Once the reaction was complete and cooled to room temperature, TOP-Br_2 was dissolved in toluene (18.7 mL).

Synthesis of 5 nm $CsPbBr_3$-ASC18 NCs: Cs-oleate (4 mL, 1.6 mmol), Pb-oleate (5 mL, 2.5 mmol) and ASC18 (0.215 g, 0.512 mmol) were dissolved in ODE (10 mL) and heated to 130 °C under vacuum, whereupon the atmosphere was changed to argon and TOP-Br_2 in toluene (5 mL, 5 mmol Br_2) was injected. The reaction mixture was cooled immediately in an ice bath. The crude solution (24 mL) was precipitated by the addition of ethyl acetate (20 mL) and acetone (21 mL) in a N_2-filled glovebox, followed by centrifugation at 29500g for 10 min. The precipitated fraction was dispersed in toluene (3 mL) and then washed three more times. Each time the solution was mixed with two volumetric equivalents of acetone and centrifuged at 1300g for 10 min before being dispersed in progressively smaller volumes of solvent (1.5 mL, then 0.75 mL). After the final precipitation, NCs were dispersed in toluene (3 mL) and centrifuged at 1300g for 1 min to remove non-dispersed residue. Z-cut single-crystalline quartz substrates were cleaned by sonication in soap water and water stream and then blow-dried (sequence repeated twice), sonicated in ethanol and acetone – blow-drying between steps – and covered with a monolayer of hexamethyldisilazane before annealing in a N_2-filled glovebox. Films were prepared by drop-casting from a 0.8 mg/mL NC solution.

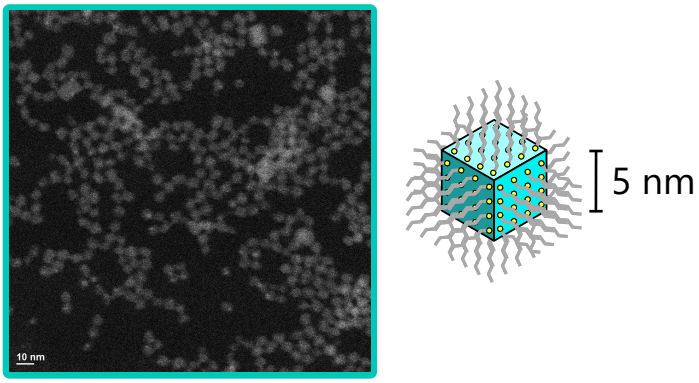


Figure 4.1 – Scanning tunnelling electron micrograph of 5 nm $CsPbBr_3$ NCs, scale = 10 nm.

$CsPbBr_3$ NPLs, prepared by Dr. Federico Montanarella (ETH Zurich)

Chemicals: Cs_2CO_3 (Aldrich, 99.9%), OA (Sigma-Aldrich, 90%), ODE (Sigma-Aldrich, 90%), oleylamine (OAm, Acros Organics, 80–90%), $PbBr_2$ (ABCR, 98%), mesitylene (Aldrich, 97%) and toluene (Fischer Scientific, HPLC grade). All materials were used without any further purification except OA and OAm, which were pre-dried for 1 h under a vacuum at 125 °C and stored in the glovebox.

Cs-oleate precursor: Cs_2CO_3 (0.4075 g), OA (1.25 mL) and ODE (20 mL) were added to a

50 mL three-neck flask and vigorously stirred under vacuum for 1 h at 120 °C, forming a transparent yellow solution. Cs-oleate was preheated to 100 °C prior to injection to avoid precipitation.

Synthesis of $CsPbBr_3$ NPLs: $PbBr_2$ (138 mg) and pre-dried OA and OAm were loaded into a 25 mL three-necked round-bottom flask under N_2 atmosphere. The flask was transferred to a Schlenk line and mesitylene (5 mL) was added to the reaction mixture. The system was flushed (N_2/vac.) three times at room temperature, after which the temperature was raised to 130 °C under N_2 flow. Cs-oleate (0.8 mL) was swiftly injected and the reaction was immediately stopped by immersing the reaction flask in a cold-water bath. After the reaction, 1 mL of crude solution was centrifuged for 3 min at 5000 rpm. The obtained precipitate was dispersed in 1 mL of toluene and centrifuged again for 10 min at 13400 rpm, before the supernatant was filtrated.

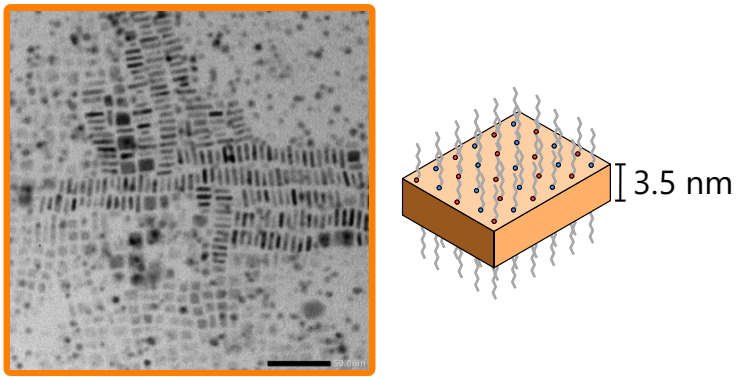


Figure 4.2 – Transmission electron micrograph of $CsPbBr_3$ NPLs, scale = 50 nm.

$(PEA)_2PbI_4$, prepared by Dr. Martin Kroll (TU Dresden)

The precursor solution was prepared by dissolving PEAI (GreatCell Solar) and PbI_2 (TCI) in a stoichiometric ratio in dimethylformamide (DMF, Acros) to obtain a 0.25 M solution. Prior to deposition, quartz substrates were sequentially cleaned in acetone, ethanol and isopropanol by ultrasonication for 10 min, followed by an oxygen plasma treatment at 100 mW for 10 min. The drop-cast films were prepared by dropping 100 µL of the solution on a substrate, followed by 10 min of annealing at 100 °C. A home-built setup was used for fabrication of zone-cast films. The substrates were placed on a 100 °C aluminium block and moved slowly (0.02 mm/s) using stepper motors below a nozzle, which supplied a meniscus of the perovskite solution.

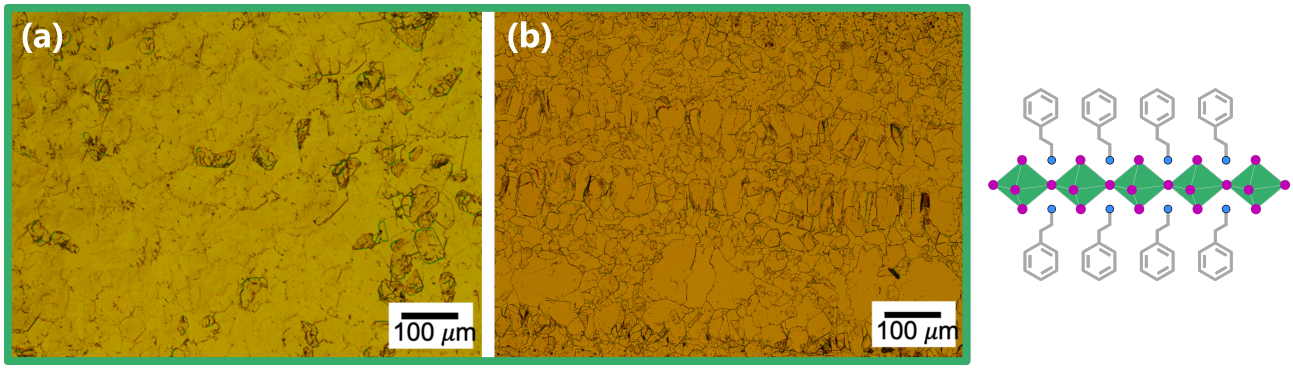


Figure 4.3 – Optical microscope images of (a) drop-cast and (b) zone-cast $(PEA)_2PbI_4$ films.

4.2.2 PPP-NIR

PPP-NIR experiments were performed using the setup described in Section 3.3.1. A 490 nm pump was generated by frequency-mixing of the 800 nm fundamental and ∼1200 nm TOPAS-I signal output in a BBO. The ∼2000 nm push and probe were derived from the TOPAS-II idler output. Measurements were taken from multiple spots from three replicas of each material.

4.3 Results and discussion

In order to resolve the ongoing debate regarding the effect of confinement on the hot carrier cooling dynamics of LHP nanomaterials, a selection of systems with a range of sizes and dimensionalities are studied herein. The use of ultrafast PPP spectroscopy allows independent control of the cold and hot carrier sub-populations via the pump and push fluences, respectively. The upshot of this is two-fold: (i) the hot carrier density-dependence of cooling may be investigated in a total carrier density that precludes significant effects of Auger recombination which can obscure hot carrier dynamics; and (ii) allows separation of the cooling pathways mediated by carrier-carrier and carrier-phonon scattering. Here, carrier cooling dynamics are investigated through the framework of their hot phonon bottleneck behaviour. As such, most systems are based on the $CsPbBr_3$ perovskite as their monatomic cation imbues them with a more pronounced hot phonon bottleneck than other compositions such as $MAPbI_3$,[218,231,269] and thus any confinement effects between materials will be more apparent.

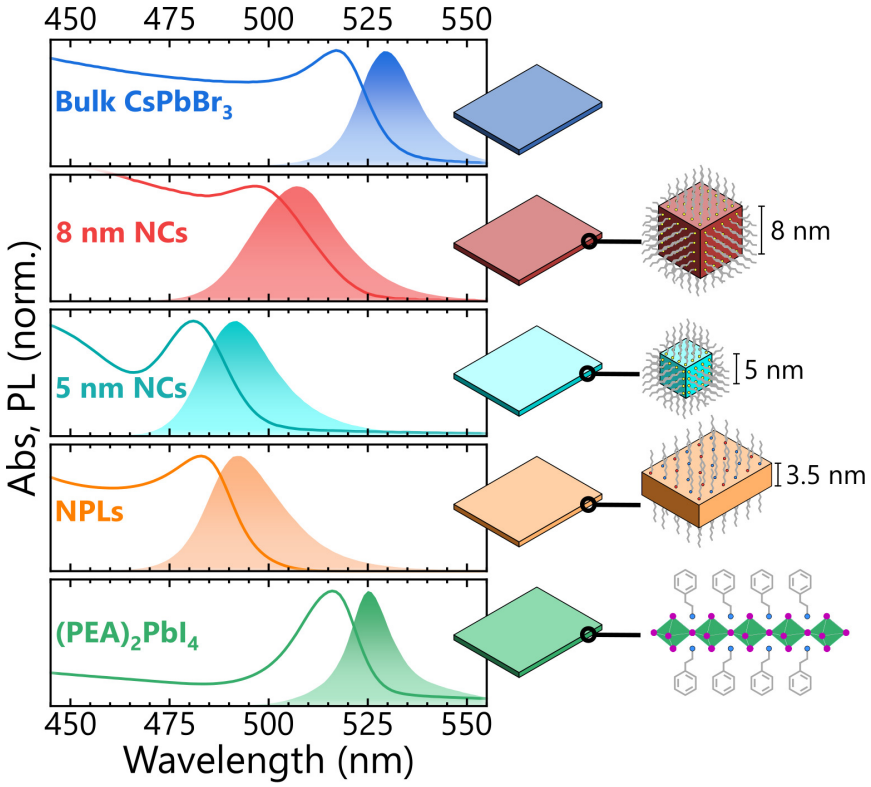


Figure 4.4 – Normalised absorption and PL spectra for each of the material systems studied.

Figure 4.4a shows the steady-state absorption and PL spectra of the studied materials. The spectra for the 5 nm NCs and 3.5 nm-thick NPLs are blue-shifted with respect to the bulk and 8 nm NCs, which are manifestations of the increased confinement experienced by carriers. While the lowest-lying exciton absorption and PL peak of the NPLs are closely aligned with that of the 5 nm NCs, the CBM of the former lies higher in energy due to its greater E_b, as shown later in this Chapter. The strongest confinement is apparent in the RP-type $(PEA)_2PbI_4$, whose optical spectra are strongly blue-shifted with respect to that typically found in bulk lead iodide-based perovskites.

The action of the pump, push and probe pulses on carriers is summarised schematically in Figure 4.5a, and the resulting effect on exemplar kinetics in Figure 4.5b. The pump produces free carriers whose time-evolving population is monitored by a ∼2 µm probe within the broad featureless intraband NIR absorption observed in LHPs.[270,271] At a fixed delay (∼12 ps), an intense ∼2 µm push pulse arrives at the sample, optically re-exciting a portion of the band-edge carriers to form a new population of hot carriers, and bleaching the transient response. Increasing the push fluence results in an increase in the bleach magnitude, corresponding to a

higher hot carrier density. Fitting the bleach and its recovery to the 'pump-only' baseline with a Gaussian-modified ($\sigma = 100$ fs, see Figure 4.5c) monoexponential allows extraction of a time constant associated with cooling, τ_{cool}. In all cases, the push fluence is limited so as to avoid interband transitions via multiphoton absorption. As the effective masses of electrons and holes are expected to be similar in LHPs,[272] the discussion of their dynamics is generalised for both carrier types.

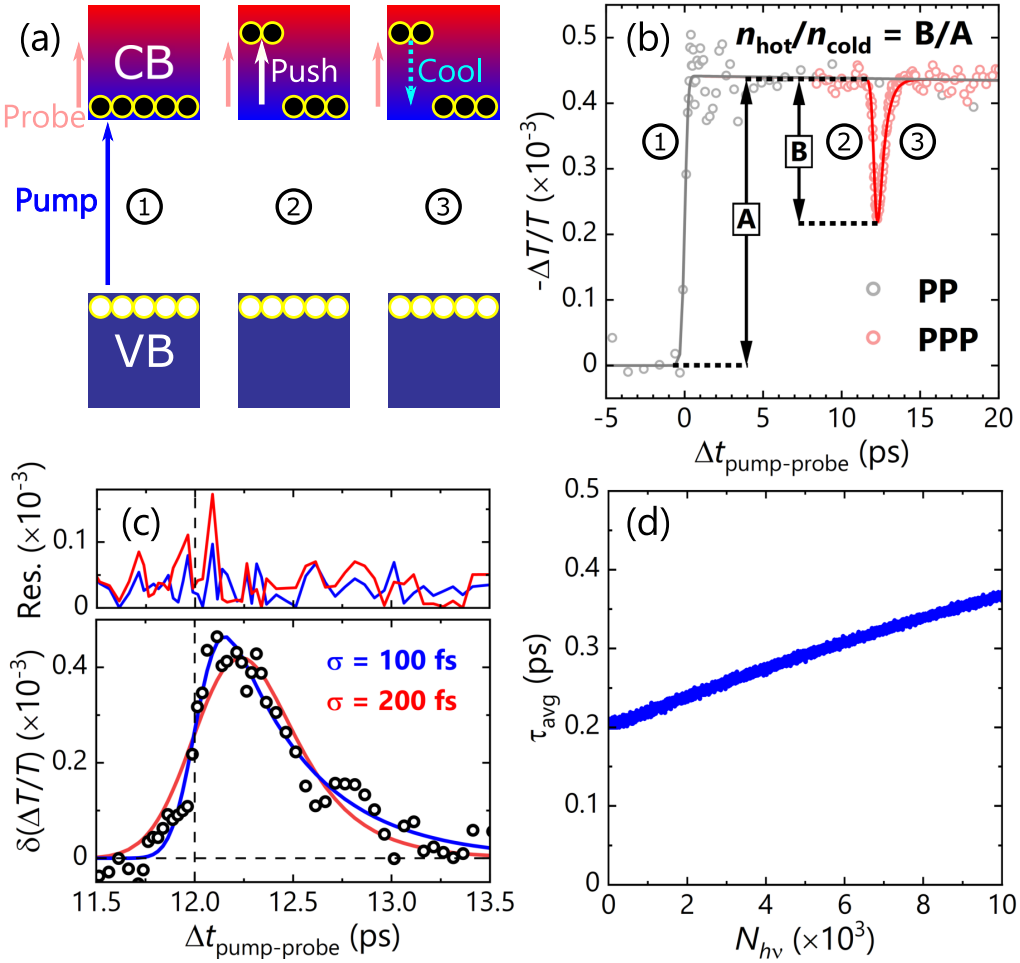


Figure 4.5 – (a) The action of the pump and push pulse on carrier populations and (b) Exemplar PPP-NIR transients, also showing calculation of n_{hot}/n_{cold}. (c) The push-induced bleach rise is most accurately described by a Gaussian convolution with a width (σ) of 100 fs, and is used for all fits to the PPP-NIR transients. (d) Monte Carlo simulation of cooling within strictly confined NCs gives the same trend as that observed in bulk systems.

In this Chapter, the cooling time is investigated as a function of n_{hot}/n_{cold} – that is, the push-induced hot carrier density (n_{hot}), normalised to the pump-induced cold carrier density (n_{cold}),

as described in Figure 4.5b and Equation 4.1.

$$n_{\text{hot}}/n_{\text{cold}} = \left| \frac{\delta(\Delta T/T)}{\Delta T/T} \right| = \frac{B}{A} \tag{4.1}$$

This metric is advantageous because (i) it eliminates the need to calculate exact absolute values of n_{hot}, which would require accurate measurement of the pump and push/probe absorptivity across different areas of inhomogeneous films; and (ii) it includes the effects of both n_{hot} and n_{cold} on the cooling dynamics, such that different material classes can be directly compared, assuming n_{cold} is not too high.[232] While this might suggest a population inversion is achieved for $n_{\text{hot}}/n_{\text{cold}} > 0.5$, that some cooling inevitably occurs within the push pulse duration ensures vacant hot states are replenished and more than half of the cold carrier density may be optically re-excited. Strictly speaking, a 200% bleach would be expected for a total population inversion due to the added effect of SE, requiring a correction factor not accounted for here. The implicit assumption in adopting $n_{\text{hot}}/n_{\text{cold}}$ as the metric by which to compare the different materials is that the nanomaterials also exhibit a spatially averaged bulk-like carrier density, as opposed to describing their average population *within* each crystallite (i.e. "per dot"). To justify this, a Monte Carlo algorithm was employed to model the action of the push pulse on an array of strictly confined NCs. $N_{h\nu}$ push photons are randomly assigned to a test set of 10000 already-pumped NCs. As $N_{h\nu}$ (equally, push fluence) increases, the probability distribution of forming 0, 1 or 2 hot carrier(s) in each NC shifts to a higher average value. Assuming cooling within singly occupied NCs takes τ_1, and τ_2 in doubly occupied NCs (where $\tau_1 < \tau_2$ due to the hot phonon bottleneck), the weighted average cooling time across all NCs increases smoothly with $N_{h\nu}$, as shown in Figure 4.5d. The result obtained is very similar to a bulk free carrier model and therefore both classes of system may be treated in the same way.

Figure 4.6a shows the pump fluence-dependence of the PP transients for cuboidal $CsPbBr_3$ NCs with edge lengths of 5 nm. At low fluence, the kinetics are described by a single component ascribed to radiative electron-hole recombination with $\gg$1 ns lifetime. A second, faster component ($\tau \sim 10$ ps) is apparent at higher fluences, ascribed to the three-body Auger recombination process. PPP measurements were carried out at a low pump fluence ($F_{\text{pump}} \lesssim 10$ µJ cm^{-2}, nom-

inally corresponding to an average NC occupation of $\langle N \rangle \sim 0.3$, assuming all light is absorbed within 100 nm of the NC film) so as to remove Auger effects, thereby isolating the hot phonon bottleneck behaviour by varying the push fluence. Figure 4.6b displays the push-induced bleach after subtraction of the PP 'background' in PPP measurements, $|\delta(\Delta T/T)|$.

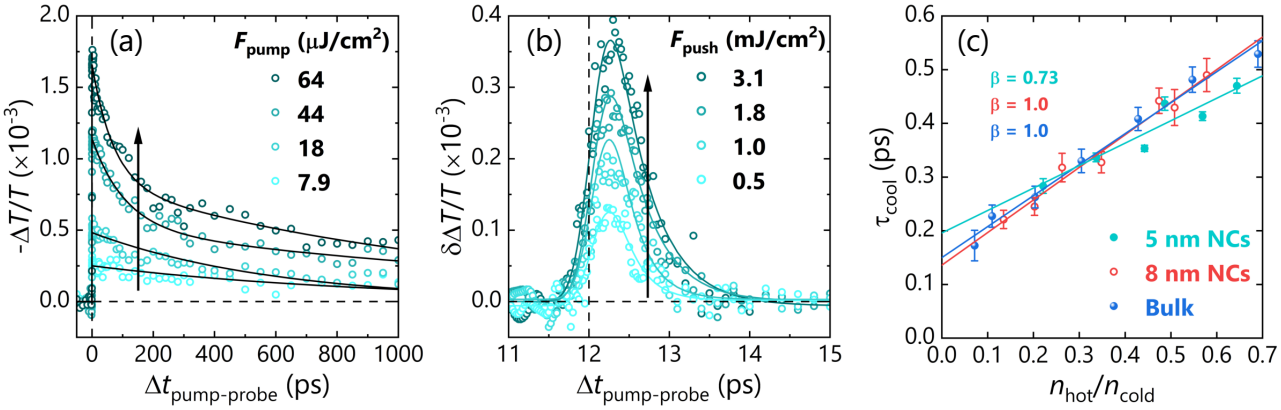


Figure 4.6 – (a) Pump fluence-dependent PP kinetics of $CsPbBr_3$ NCs. (b) Push fluence-dependent PPP kinetics around the region of the push-induced bleach. (c) Hot carrier density-dependent hot carrier dynamics in $CsPbBr_3$. The 5 nm NCs exhibit a slightly suppressed hot phonon bottleneck (β) than larger analogues.

Figure 4.6c shows how τ_{cool} in 5 nm NCs increases with increasing hot carrier density due to the hot phonon bottleneck. This is analogous to the behaviour exhibited by the bulk and 8 nm NCs (measured by Dr. Thomas Hopper, Imperial College London[232,273]). Hereinafter, the parameter β is chosen to represent the strength of the hot phonon bottleneck, and is calculated from the slope of $\tau(n_{hot}/n_{cold})$ for each system, normalised to that of bulk $CsPbBr_3$. The y-intercept can be ascribed to the intrinsic cooling time of an isolated hot carrier. In contrast to the 8 nm NCs, the 5 nm NCs analogues exhibit a slightly suppressed hot phonon bottleneck ($\beta = 0.73 \pm 0.07$) and similar intrinsic cooling time, which suggests that the *phonon bottleneck* is not present, or at least does not have a dominant effect on cooling dynamics in LHP NCs of this confinement regime. This is in keeping with other studies on hot carrier cooling in LHPs which saw minimal deviation from bulk-like behaviour in NCs larger than ∼4 nm.[221,260,261]

To extend this study into stronger confinement regimes, $CsPbBr_3$ NPLs of ∼3.5 nm (or 6 MLs) thickness, and lateral dimensions of $\sim 11 \times 14$ nm, were studied. As described in Figure 4.7a, the PP transients for the NPLs follow a similar dependence on F_{pump} as the NCs: at low fluence, the kinetics can be described by a single exponent corresponding to band-edge recombination;

and a faster Auger-type component becomes apparent at early times for the higher fluences. All PPP measurements were undertaken at $F_{\text{pump}} \lesssim 10$ µJ cm^{-2} to remove the effect of higher-order recombination pathways, and the resulting transients exhibit the same characteristic push-induced bleach and recovery as all other systems (Figure 4.7b).

As can be seen from Figure 4.7c, the hot phonon bottleneck is suppressed ($\beta = 0.42 \pm 0.08$) with respect to the 5 nm NCs. In principle, there may be three underlying causes for this effect: (i) increased carrier-phonon coupling due to the intrinsic confinement of the NPLs; (ii) increased carrier-phonon coupling to the surface and/or ligands in the NPLs, owing to their greater surface area:volume ratio and differing ligands (OA/OAm versus ASC18); or (iii) increased hot-cold carrier coupling.

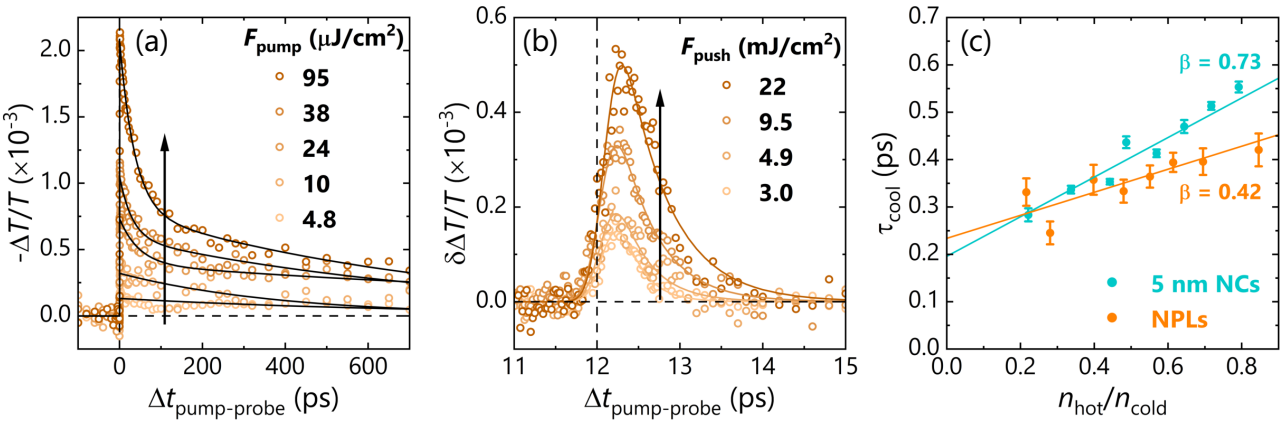


Figure 4.7 – (a) Pump fluence-dependent PP kinetics of $CsPbBr_3$ NPLs. (b) Push fluence-dependent PPP kinetics around the region of the push-induced bleach. (c) Hot carrier density-dependent hot carrier dynamics in $CsPbBr_3$ NCs and NPLs. The NPLs exhibit a suppressed hot phonon bottleneck (β) due to enhanced carrier-carrier scattering.

On (i), other studies have predicted minimal changes in phonon spectra[274,275] and Fröhlich coupling constant[276] for NPLs of this thickness. While the accelerated cooling observed elsewhere in NPLs was attributed to changes in the carrier-phonon coupling,[263,264] these studies were carried out on thinner (3 ML) NPLs via *two-pulse* TAS, which is not sensitive to the effect of carrier-carrier coupling. On (ii), other works have suggested that the dimensionality of the nanosystem has far greater influence on its cooling dynamics than the choice of ligand.[228,260] While Liu *et al.*[277] observed a modulation of the cooling time in $CsPbBr_3$ NCs through substitution of the OAm ligands by a cross-linked polysiloxane, this represents a much more drastic

shift in the nature of the ligand and its surface coupling than between the NC-ASC18 and NPL-OA/OAm systems discussed here.

Therefore, this leaves (iii) as the more likely explanation: the greater confinement in NPLs causes an increase in hot-cold carrier coupling. This, in turn, provides an alternative cooling pathway which increases the hot phonon density required to slow cooling and thus flattens the observed dependence of τ_{cool} on n_{hot}. Herz *et al.*[235] and Kahmann *et al.*[278] both highlighted the role of the background cold holes formed by the self-doping of Sn-based perovskites; and a similar effect of 'spectator' excitons has been observed in PbS NCs by Ruhman *et al.*[279] This cooling pathway mediated by carrier-carrier scattering has similarities with the 'Auger cooling' mechanism reported in CdSe QDs.[190,191,280] Here, the hot electrons circumvent any phonon bottleneck by instead transferring their excess energy to cold holes; the nascent hot holes then cool rapidly due to the higher VB DOS. However, as mentioned, the electrons and holes are expected to have similar effective masses in LHPs, and so the precise mechanism presumably differs slightly to this case.

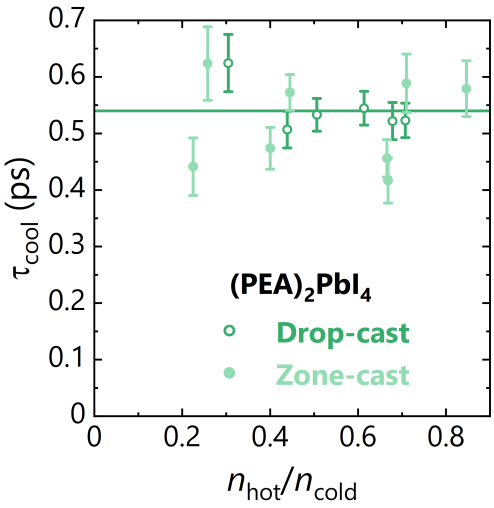


Figure 4.8 – The hot phonon bottleneck is completely suppressed ($\beta < 0.2$) in the RP-type $(PEA)_2PbI_4$ due to its highly excitonic character.

The study was then extended to the RP-type perovskite $(PEA)_2PbI_4$, whose single-ML thickness results in a much higher E_b than the previously discussed systems. All ultrafast spectroscopic measurements for $(PEA)_2PbI_4$ were carried out by Ziyuan Ge (Imperial College London). The experimental approach followed a similar protocol to the aforementioned systems: the PP

dynamics were evaluated to find an excitation regime in which many-body recombination is suppressed, and then used to study the push-fluence dependence of the PPP-NIR response. A full discussion of the PP dynamics found in this system can be found in Ref. [234], and only the hot phonon bottleneck is discussed herein. As can be seen from Figure 4.8, there is no correlation ($\beta < 0.2$) between n_{hot} and τ_{cool}, implying the total lack of a hot phonon bottleneck. This is ascribed to the further enhanced electron-hole coupling in this highly excitonic system, arising from the reduction in screening and resulting stronger Coulombic interaction between charges. This behaviour is the same in both drop-cast and zone-cast samples, despite the quite dissimilar film morphologies between the two, adding support to the notion that the differences in hot carrier dynamics between systems is not due to an effect of carrier-surface coupling.

The behaviour of $(PEA)_2PbI_4$ also differs from the other ABX_3 nanomaterials in that its intrinsic hot carrier lifetime is consistently longer ($\sim$550 fs). This may allude to there being, somewhat paradoxically, a *phonon bottleneck* even in the absence of a *hot phonon bottleneck*. That is, the electronic state distribution of $(PEA)_2PbI_4$ may contain quasi-discrete regions which slows hot carrier cooling due to the requirement for multiphonon coupling; but the enhanced carrier-carrier scattering due to increased confinement suppresses the density-dependence of τ_{cool}. While the spacer ligand is expected to contribute more to the photophysics of 2D perovskites, a recent report observed only modest exciton coupling to phonons derived from the organic moiety in a RP iodide-perovskite.[281] The difference in intrinsic cooling time is partly determined by the choice of halide,[231] however this effect alone is not sufficient to explain the difference observed here. Even longer (>1 ps) timescales have been reported elsewhere,[268] however this was observed in multiple-QW structures which exhibit the charge cascade effect from wide- to narrow-gap layers, obscuring the intrinsic intraband relaxation time of each.

The demonstration of a suppressed hot phonon bottleneck in more strongly confined LHPs is consistent with reports elsewhere. Cassette *et al.*[228] showed that RP perovskites exhibit a stronger hot phonon bottleneck as solid films than colloidal dispersions; and Wang *et al.*[282] observed the absence of a hot phonon bottleneck in isolated $CsPbBr_3$ NPLs which became activated upon formation of a layer-stacked 'superlattice'. Conversely, Pb-chalcogenide QDs were

shown to exhibit slower cooling with a greater inter-dot spacing, either through dispersion in a solvent[283] or control over solid film growth.[284] Therein, the authors attributed the differences to the ability of carriers to access phonons on neighbouring QDs, alleviating the phonon bottleneck within each QD. A comparison of solution- and solid-phase systems was beyond the scope of the current work due to issues with solvent effects under intense push illumination, but it is likely that the determining factor in the LHP nanomaterials is different as the phonon bottleneck is not as strong.

It should be noted that hot carrier "cooling" in this context – despite its name – is not a thermal process because the timescales involved are too fast for thermal equilibrium of carriers and the lattice to be achieved, as exemplified by time-resolved microscopy measurements wherein thermal transport was observed on timescales of several nanoseconds.[285] For the same reason, any heat from the push pulse will dissipate fully between laser pulses separated by 250 µs (f = 4 kHz), meaning its effect will not "build up" over the course of an experiment. Furthermore, the differences in cooling dynamics between nanomaterials are unlikely to be a consequence of thermal conductivity as thermal transport is primarily governed by acoustic phonons[286] (rather than Fröhlich-coupled LO phonons that mediate intraband relaxation); and the lower conductivity of 2D perovskites[287] ought to give the opposite trend if thermal effects were dominant here. Taking these factors combined, it can be assumed that the action of the push pulse is solely to *optically* transit cold carriers to hot states, and its recovery governed by hot carrier-LO phonon and hot-cold carrier scattering dynamics.

4.4 Kinetic modelling of confinement effect on cooling dynamics

In order to more rigorously quantify the observations described thus far, a numerical kinetic model was developed based on the following system of coupled differential equations, and

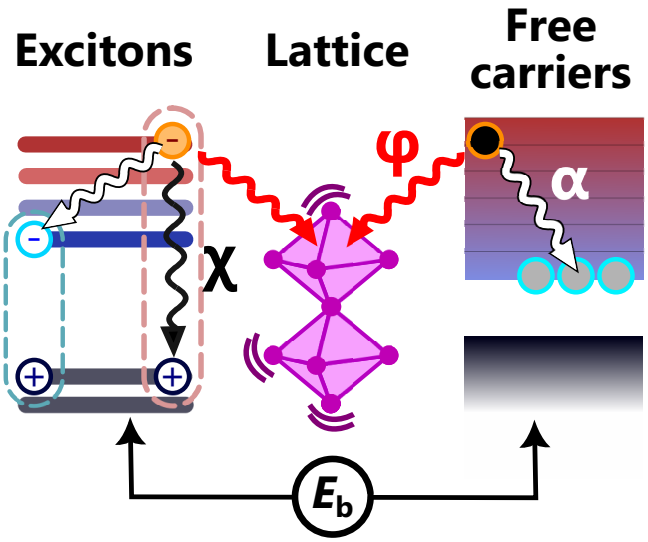


Figure 4.9 – Schematic diagram depicting the various loss pathways for hot carriers modelled in this work. α: hot-cold carrier scattering; φ: carrier-phonon scattering; χ: exciton cooling.

described schematically in Figure 4.9:

$$\frac{\mathrm{d}n_{\mathrm{hot}}}{\mathrm{d}t} = -\alpha n_{\mathrm{hot}} n_{\mathrm{cold}} - \phi n_{\mathrm{hot}} n_{\mathrm{ph}} - \chi n_{\mathrm{HX}} \tag{4.2}$$

$$\frac{\mathrm{d}n_{\mathrm{cold}}}{\mathrm{d}t} = \alpha n_{\mathrm{hot}} n_{\mathrm{cold}} + \phi n_{\mathrm{hot}} n_{\mathrm{ph}} + \chi n_{\mathrm{HX}} \tag{4.3}$$

$$\frac{\mathrm{d}n_{\mathrm{ph}}}{\mathrm{d}t} = -\phi n_{\mathrm{hot}} n_{\mathrm{ph}} \tag{4.4}$$

Here, n_{hot} and n_{cold} are the total hot and cold state densities, respectively, and the hot states are further sub-divided into hot free carriers (HCs) and hot excitons (HXs), i.e. $n_{\mathrm{hot}} = n_{\mathrm{HC}} + n_{\mathrm{HX}}$. Vacant phonon modes (those that are available to receive excess carrier energy) have a density n_{ph}, and become occupied upon scattering with hot carriers whereupon they no longer contribute to cooling. α and ϕ are coefficients describing hot-cold carrier and hot carrier-phonon scattering, respectively. This assumes that HCs and HXs cool via these mechanisms with identical efficiencies, and the coefficient χ therefore represents a cooling 'enhancement factor' due to cooling *within* an exciton. Band-to-band recombination and occupied phonon freeing rates are assumed negligible on timescales relevant for hot carrier cooling.

The partitioning of total ES density between free carriers (n_{e}) and bound excitons (n_{x}) can be

described by the Saha equation:[132,133,288–290]

$$\frac{n_e^2}{n_x} = \frac{1}{\lambda^3} e^{-\xi} \qquad \text{where} \quad \xi = \frac{E_b}{k_B T} \quad \text{and} \quad \lambda = \frac{h}{\sqrt{2\pi \mu_{eh}^* k_B T}} \tag{4.5}$$

where $\mu_{eh}^* = 0.2 m_e$.[289] E_b values are extracted from the optical absorption spectrum of each system using the Elliott model (Figure 4.10), as outlined in Section 3.5. This portion of work was carried out with the assistance of Rozana Mazlumian (University College London). The fitted E_b values show good agreement with the literature[43,103,291,292] when used alongside the fitting parameters shown in Table 4.1. The value used for the bulk $CsPbBr_3$ was taken from the literature and not verified further here as a result of the morphological effects in bulk perovskites that can lead to prominent excitonic peaks in their absorption spectra despite having a low E_b.[251,293,294] In the case of $(PEA)_2PbI_4$, spline subtraction in the region between the exciton and continuum contributions yielded a better fit to the model.

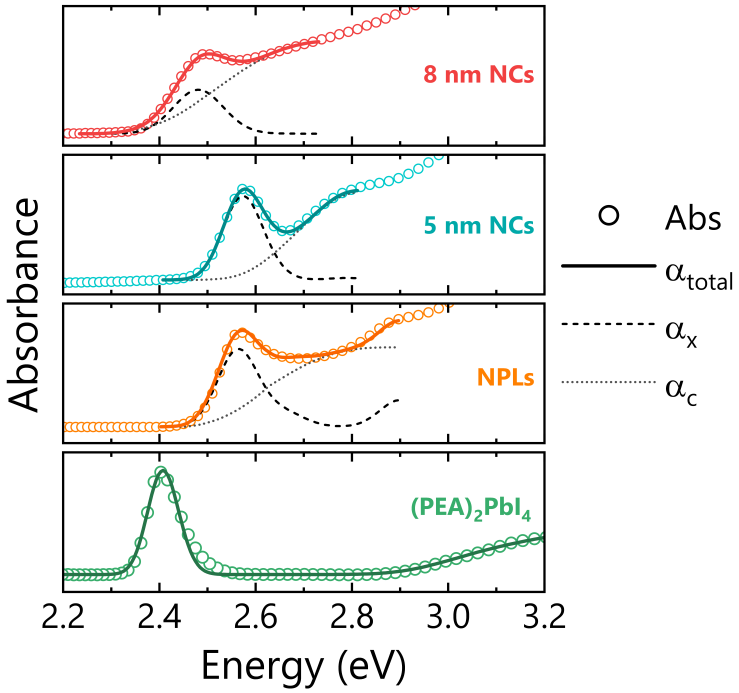


Figure 4.10 – Elliott model fits (lines) to LHP nanomaterial UV-vis spectra (open circles), showing excitonic and continuum contributions.

Here, Equation 4.5 is modified for the case of n_{hot}, n_{HC} and n_{HX}, becoming:

$$\frac{x^2}{1-x} = \frac{1}{n_{hot}\lambda^3} e^{-\xi} \tag{4.6}$$

	E_b (eV)	E_g (eV)	A_x (arb.u.)	σ_x (eV)	B_x (arb.u.)	E_2 (eV)	A_c (arb.u.)	σ_c (eV)
8 nm NCs	0.044	2.52	0.48	0.05	n/a	n/a	0.07	0.43
5 nm NCs	0.055	2.63	0.43	0.19	0.02	2.79	0.08	0.30
NPLs	0.11	2.68	0.24	0.04	0.08	2.90	0.02	0.59
$(PEA)_2PbI_4$	0.24	2.65	0.45	0.07	n/a	n/a	0.03	0.55

Table 4.1 – Elliott fitting parameters for UV-vis absorption spectra.

where $x = n_{\mathrm{HC}}/n_{\mathrm{hot}}$. Rearranging in the form $ax^2 + bx + c$ yields:

$$x^2 + \frac{e^{-\xi}}{n_{\mathrm{hot}}\lambda^3}x - \frac{e^{-\xi}}{n_{\mathrm{hot}}\lambda^3} = 0 \tag{4.7}$$

$$x = -\frac{e^{-\xi}}{2n_{\mathrm{hot}}\lambda^3} \pm \frac{1}{2}\sqrt{\left(\frac{e^{-\xi}}{n_{\mathrm{hot}}\lambda^3}\right)^2 + \frac{4e^{-\xi}}{n_{\mathrm{hot}}\lambda^3}} \tag{4.8}$$

In Equation 4.8, each term is dimensionally consistent with that expected. Furthermore, $c < 0 < a,b$ and thus $b^2 - 4ac > 0$ (so roots are real) and $b < \left|\sqrt{b^2 - 4ac}\right|$, meaning there is exactly one positive solution which is taken as the true value of x. Rate equations 4.2 and 4.3 can then be re-expressed in terms of x:

$$\frac{\mathrm{d}n_{\mathrm{hot}}}{\mathrm{d}t} = -\alpha n_{\mathrm{hot}} n_{\mathrm{cold}} - \phi n_{\mathrm{hot}} n_{\mathrm{ph}} - \chi(1-x)n_{\mathrm{hot}} \tag{4.9}$$

$$\frac{\mathrm{d}n_{\mathrm{cold}}}{\mathrm{d}t} = \alpha n_{\mathrm{hot}} n_{\mathrm{cold}} + \phi n_{\mathrm{hot}} n_{\mathrm{ph}} + \chi(1-x)n_{\mathrm{hot}} \tag{4.10}$$

As described in Section 3.4, the Midpoint method is a convenient numerical approximation used to solve coupled differential equations. The initial boundary conditions imposed for the simulations are:

$$n_{\mathrm{hot}}(i=0) = I_{\mathrm{push}} \times N_{\mathrm{pump}}$$

$$n_{\mathrm{cold}}(i=0) = (1 - I_{\mathrm{push}}) \times N_{\mathrm{pump}}$$

$$n_{\mathrm{ph}}(i=0) = N_{\mathrm{ph}}$$

where N_{pump} is the carrier density produced by the pump and a portion thereof is instanta-

neously re-excited by the push ($0 < I_{\text{push}} < 1$). N_{ph} is the total available phonon density at the instant immediately prior to the push arrival. For a given initial hot carrier density, hot carrier cooling within a system with a higher E_{b} is faster due to the exciton cooling term in Equation 4.9, as exemplified in Figure 4.11a.

The simulations were looped over a range of I_{push}, and the cooling time extracted by fitting an exponential decay function ($e^{-t/\tau_{\text{cool}}}$) to the simulated kinetics. The dependence of the predicted τ_{cool} on I_{push} – i.e. β – was then calculated for a range of E_{b}. As summarised in Figure 4.11b, the kinetic model accurately reproduces the experimental hot phonon bottleneck dependence on E_{b} using parameters displayed in Table 4.2. The values for α and ϕ are based on a previous kinetic model of cooling within larger $CsPbBr_3$ NCs,[295] with χ tuned to give good agreement with experiment. The results of the kinetic model add further strength to the notion that cooling is more strongly influenced by carrier-carrier scattering in systems with greater excitonic character, leading to a suppression of the hot phonon bottleneck. The observation of efficient carrier-carrier scattering mediating the cooling of hot carriers also gives tentative insight into the prior thermalisation step (Section 2.3). While this process falls within the instrument response function (IRF) of most experimental setups, it may guide first-principles investigations into carrier thermalisation, such as those reported recently.[296]

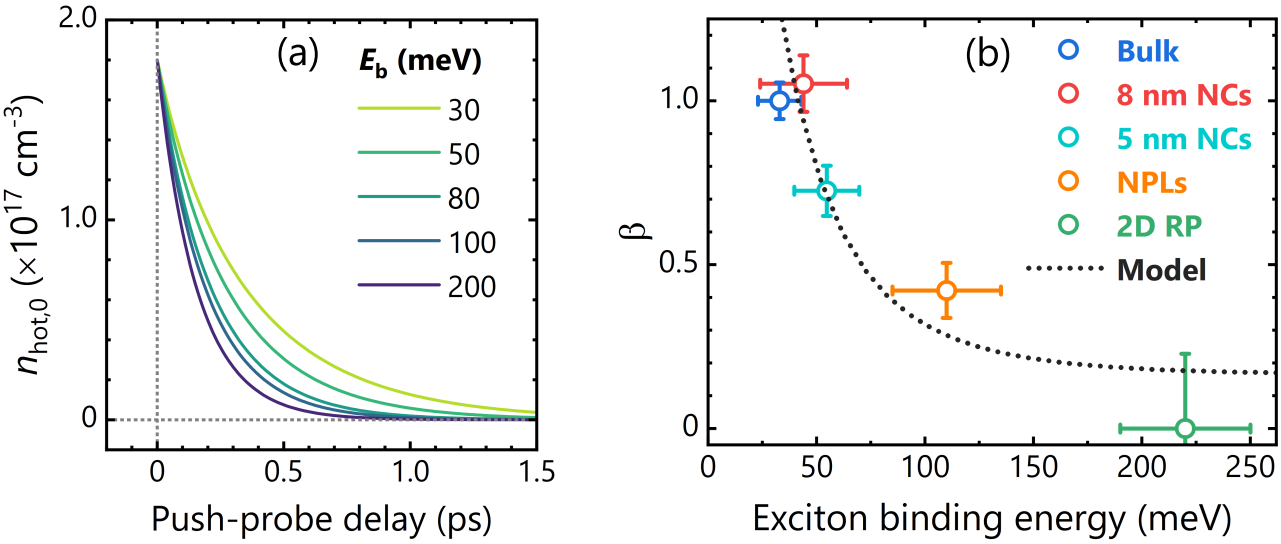


Figure 4.11 – (a) For a given initial hot carrier density, cooling is faster in systems with higher E_{b}. (b) The kinetic model accurately reproduces the experimental trend of a reduced hot phonon bottleneck in the more excitonic systems; error bars denote 99% confidence intervals.

Fit parameter			Value
Pump carrier density	n_{pump}	(cm^{-3})	2.0×10^{17}
Carrier-carrier	α	(cm^3 ps^{-1})	2.0×10^{-18}
Carrier-phonon	ϕ	(cm^3 ps^{-1})	1.8×10^{-17}
Exciton cooling	χ	(ps^{-1})	5.1
Total phonon density	N_{ph}	(cm^{-3})	1.0×10^{17}

Table 4.2 – Kinetic model fitting parameters for confinement effect on hot carriers in LHP nanomaterials.

4.5 Conclusions

In this Chapter, the effect of quantum confinement on the hot carrier dynamics of LHP nanomaterials has been investigated through the use of multi-pulse PPP intraband spectroscopy. This technique allows control over the hot carrier density in a regime that precludes many-body Auger recombination that would otherwise obscure cooling dynamics. The density-dependent cooling times are evaluated, revealing that in more confined systems characterised by a higher exciton binding energy, the hot phonon bottleneck effect becomes increasingly suppressed. This is attributed to the enhanced influence of hot-cold carrier scattering in more confined systems, which provides an efficient alternative cooling pathway and diminishes the role of carrier-phonon interactions. This work represents the first systematic comparison of hot carrier dynamics in such a range of confinement regimes, and highlights the critical importance of evaluating the carrier density-dependence of the response when drawing comparisons between systems. As such, it should help resolve disparities surrounding the precise effect of confinement on hot carrier dynamics, which have generally arisen through comparing a limited range of systems under a single excitation condition.

In the RP-type system, the intrinsic hot carrier lifetime is longer, suggesting that a phonon bottleneck arises due to the discretisation of the electronic DOS. Based solely on this observation, this might suggest the RP LHP is the best candidate for a hot carrier SC absorber. However, the cooling times are still rapid and likely to out-compete carrier extraction, while the large band gap of this strongly confined system will undoubtedly limit SC efficiency under solar

illumination. While hot carrier solar cells still remain a somewhat distant prospect owing to the rapid cooling observed, the results herein offer fundamental insight into the carrier-carrier and carrier-phonon interactions that govern all applications of lead halide perovskite nanomaterials, including those that operate under similar carrier densities as used here, such as lasers and concentrator PV.

5 Hot Carrier Trapping in Lead Halide Perovskite Nanocrystals

Having interrogated the effect of size and dimensionality on hot carrier dynamics, this Chapter aims to present insight into the reported defect tolerance of LHPs by extending its focus to hot carriers. An open question remains over whether the trapping dynamics of band-edge carriers can be extrapolated to those of their above-gap counterparts. Here, defects are introduced to a range of $CsPbX_3$ NCs via a post-synthesis treatment, and their hot carrier dynamics studied via a PPP variant employing a visible light probe. The results suggest defect tolerance is not retained in Br-based LHPs for band-edge nor above-gap excitation.

The contents of this Chapter are adapted from work described in a manuscript that is currently under preparation:
J. Ye*, N. Mondal*, **B. P. Carwithen**, Y. Zhang, L. Dai, X. Fan, P. Ghosh, C. Otero-Martínez, Z. Yu, Z. Chen, N. C. Greenham, S. D. Stranks, L. Polavarapu, A. Rao, A. A. Bakulin, R. L. Z. Hoye, Extending the Defect Tolerance of Halide Perovskite Nanocrystals to Hot Carrier Cooling Dynamics, *authors contributed equally

5.1 Background and motivation

The tolerance of LHPs towards defects is widely reported, as introduced in Section 2.5, and is one facet that has led to an impressive rise in PV and LED efficiencies from simple synthesis routes. While the earliest studies were primarily conducted for the then-archetypal LHP,

$MAPbI_3$, later studies showed that defect tolerance was not a general characteristic. For example, wide-gap Cl-containing LHPs are highly susceptible to defects,[297] which limits the performance of blue emitters,[298,299] and has ramifications for the use of wide-gap LHPs in tandem SCs.[300,301] In $CsPbX_3$ NCs, defects not only limit carrier lifetime, but can also impact stability by acting as nucleation points for degradation.[88]

Trapping dynamics are generally discussed in the context of band-edge (cold) carriers.[200,302–307] This is often achieved through analysis of their PLQY as well as TRPL dynamics. As suggested in Equation 3.2, a higher rate of non-radiative carrier loss, e.g. by trap-assisted recombination, lowers the PLQY of the sample. Similarly, faster PL dynamics are observed in time-resolved methods where competition with fast trapping is present. The most widely used TRPL method is 'time-correlated single-photon counting' (TCSPC), which usually has a resolution limited to several hundred picoseconds by a combination of the laser diode pulsewidth and the electronically gated detector. As such, the investigation of trapping and/or defect tolerance is often blind to effects on the ultrafast (sub-ps) hot carrier dynamics.

Early work by Bonn *et al.* observed trap-free hot carrier cooling.[308] Conversely, Jiang *et al.*[309] suggested that although band-edge carriers in $MAPbI_3$ were defect-tolerant, the same could not be said of the hot carriers, finding their lifetime was diminished due to trapping at the grain boundaries of polycrystalline films. Similarly, state filling at high excitation density was found to increase hole trapping at LHP NCs surfaces by surmounting an energetic barrier, which would have ramifications for lasing applications.[310] This hot carrier-activated trapping was also observed in $MAPbX_3$ NCs by Sum *et al.*[236] using a variant of PPP spectroscopy. A common theme in other notable works is that trap removal increases hot carrier lifetime, e.g. by grain boundary[311–313] or halide vacancy[314] passivation in polycrystalline films, or surface passivation in NCs.[315] In addition to prolonged lifetimes, Huang *et al.*[316] showed defect passivation by alkali cation substitution also improved hot carrier transport.

Here, the effect of defects is further expanded to the case of hot carriers in LHP NCs. This is achieved here by intentionally and systematically introducing surface defects to a range of $CsPbX_3$ NCs, namely: $CsPbBr_3$, $CsPb(Br/I)_3$ and $CsPbI_3$. The results show that the defect

tolerance of iodide-based NCs is retained for cold and hot carriers, but lost upon bromide substitution.

5.2 Specific experimental details

5.2.1 Sample preparation and characterisation

Samples were prepared by Dr. Junzhi Ye (University of Cambridge) according to previously reported procedures.[317,318] Briefly, colloidal dispersions of $CsPbBr_3$, $CsPbI_3$ and $CsPb(Br/I)_3$ NCs were obtained by ligand-halide exchange of OAm and purified by centrifugation before being re-dispersed in toluene. These are denoted the 'pristine' samples hereinafter. In the case of $CsPb(Br/I)_3$, the initial precursor PbX_2 salts were mixed in a Br:I ratio of 30:70. To create surface traps, halide ions were stripped by centrifugation in methyl acetate (MeOAc), and termed the 'washed' samples hereinafter. The edge lengths of the cuboidal NCs were 10, 11 and 12 nm for $CsPbBr_3$, $CsPb(Br/I)_3$ and $CsPbI_3$, respectively, as confirmed by transmission electron microscopy (TEM) images in Figure 5.1.

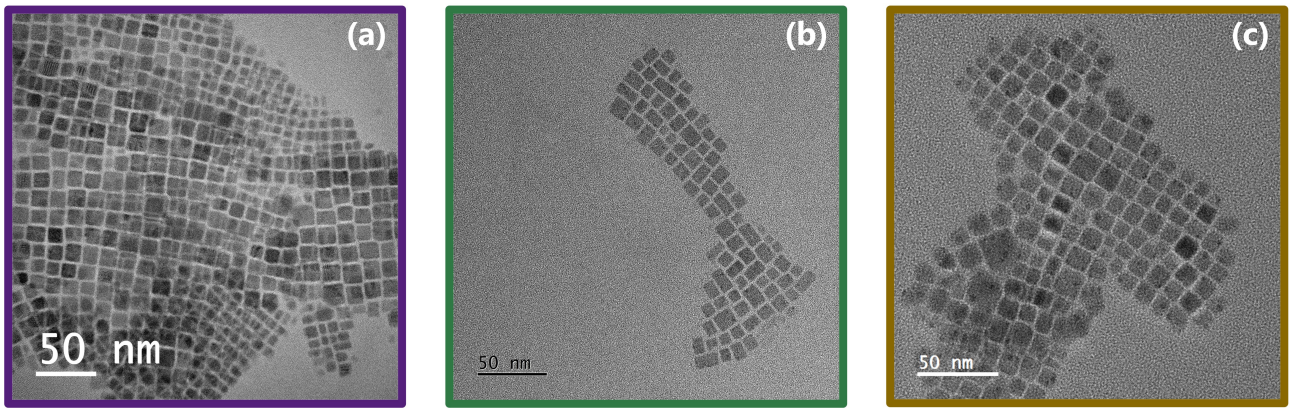


Figure 5.1 – TEM images for (a) $CsPbBr_3$, (b) $CsPb(Br/I)_3$ and (c) $CsPbI_3$.

5.2.2 PPP-Vis

The ultrafast spectroscopy experiments were performed by Dr. Navendu Mondal (Imperial College London) using the setup described in Section 3.3.2. The pump wavelength was 400 nm, ensuring sufficient photon energy to photoexcite all samples used. The push wavelength was 1300 nm in all cases, within the broad featureless NIR PIA of the samples. The laser pulsewidth

was $\sigma \sim 100$ fs, and was therefore used for all fits to the cooling dynamics. To ensure comparable excitation density across the measured samples, all NC solutions were diluted in hexane to give ~0.6 OD at the pump wavelength, and measured in a 1 mm-thick quartz cuvette.

5.3 Results and discussion

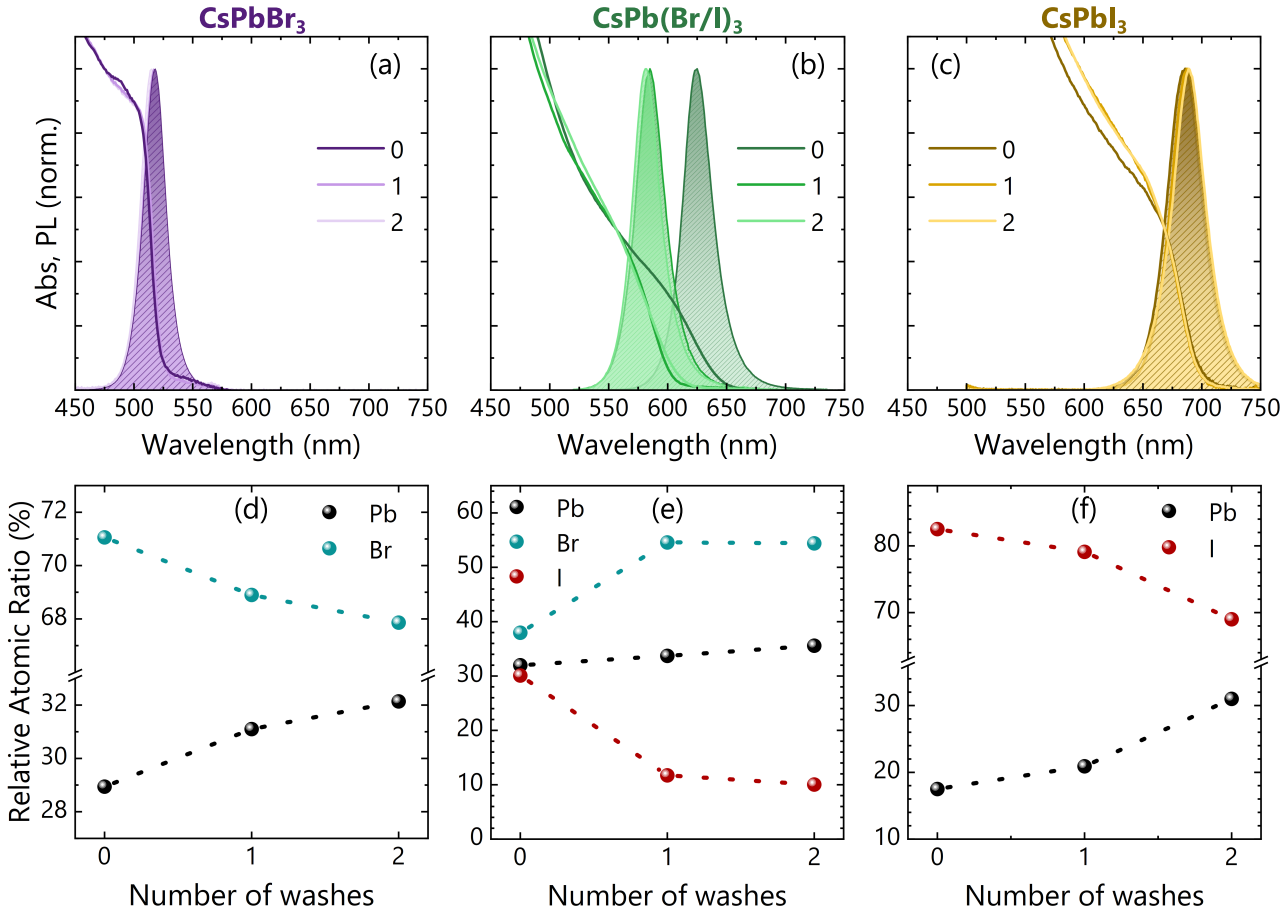


Figure 5.2 – (a-c) UV-vis absorption and PL spectra (legend: number of post-synthetic anti-solvent washes); and (d-f) Compositional analysis from XPS for $CsPbX_3$ NCs. Data provided by Dr. Junzhi Ye (University of Cambridge).

The absorption and PL spectra for each of the studied NC systems are presented in Figures 5.2a-c. The narrow PL peaks in each case suggest the NCs are highly monodisperse; while the spectra for the as-synthesised ('pristine') samples exhibit no discernible excitonic features and a minimal blue-shift relative to that expected for their respective bulk systems[43]. This attests to the weak confinement experienced by carriers in NCs of these sizes, as measured through TEM images shown in Figure 5.1. As such, the systems studied herein could reasonably be described as bulk-like but with a much greater susceptibility to surface defects.

The synthesis of LHP NCs often includes a solvent wash for purification. However, care needs to be taken to ensure this does not lead to reconstruction of the highly ionic and dynamic NC surface, nor ligand removal.[83,319] Here, this washing is directly used to control the level of defect density in the $CsPbX_3$ samples. Upon post-synthetic antisolvent washing with MeOAc, the absorption and PL peak for $CsPbBr_3$ and $CsPbI_3$ NCs remained fairly constant. Meanwhile, a clear shift was observed for the $CsPb(Br/I)_3$ NCs, becoming more reminiscent of the pure Br NCs. This suggests the surface I ions are more labile to the washing step than Br, in keeping with reports elsewhere.[317] This is further corroborated by compositional analysis via X-ray photoelectron spectroscopy (XPS), as shown in Figures 5.2d-f. Upon washing, the relative decrease in I content in $CsPbI_3$ is considerably greater than that of Br in $CsPbBr_3$, and I is preferentially etched from $CsPb(Br/I)_3$.

In the pristine samples, the PLQY follows the trend $CsPbI_3 > CsPb(Br/I)_3 > CsPbBr_3$ (Figure 5.3). Upon washing, the PLQY is lowered in each of the three compositions due to the introduction of further trap states via surface halide removal, but this is least apparent in $CsPbI_3$. This contravenes predictions from an early theoretical work, which suggested $CsPbBr_3$ remained trap-free even after several (simulated) wash cycles.[320] Therein, it was posited that the drop in PLQY upon washing was in fact due to aggregation of NCs, however this is hard to verify here given their large size and bulk-like absorbance and PL spectra. The PLQY of the $CsPb(Br/I)_3$ NCs is lowered dramatically by the washing step, more closely resembling that of the washed $CsPbBr_3$ NCs. The higher PLQY in both pristine and washed $CsPbI_3$ NCs despite their higher defect density ascertained from compositional analysis, suggests the $CsPbI_3$ NCs exhibit a higher defect tolerance than their Br-containing counterparts. These observations are consistent with those found elsewhere, wherein wider-gap LHPs are more susceptible to the formation of deep traps.[298,299,315] It should be noted that the stoichiometry of the pristine $CsPbI_3$ NCs implies a certain amount of excess iodide which is then removed upon washing. However, the twice-washed samples do show a clear iodide deficit, yet with minimal impact on the PLQY, validating discussion around defect tolerance of carriers in this work.

As a first glimpse into the effect of defects on hot carrier dynamics, the excitation energy-

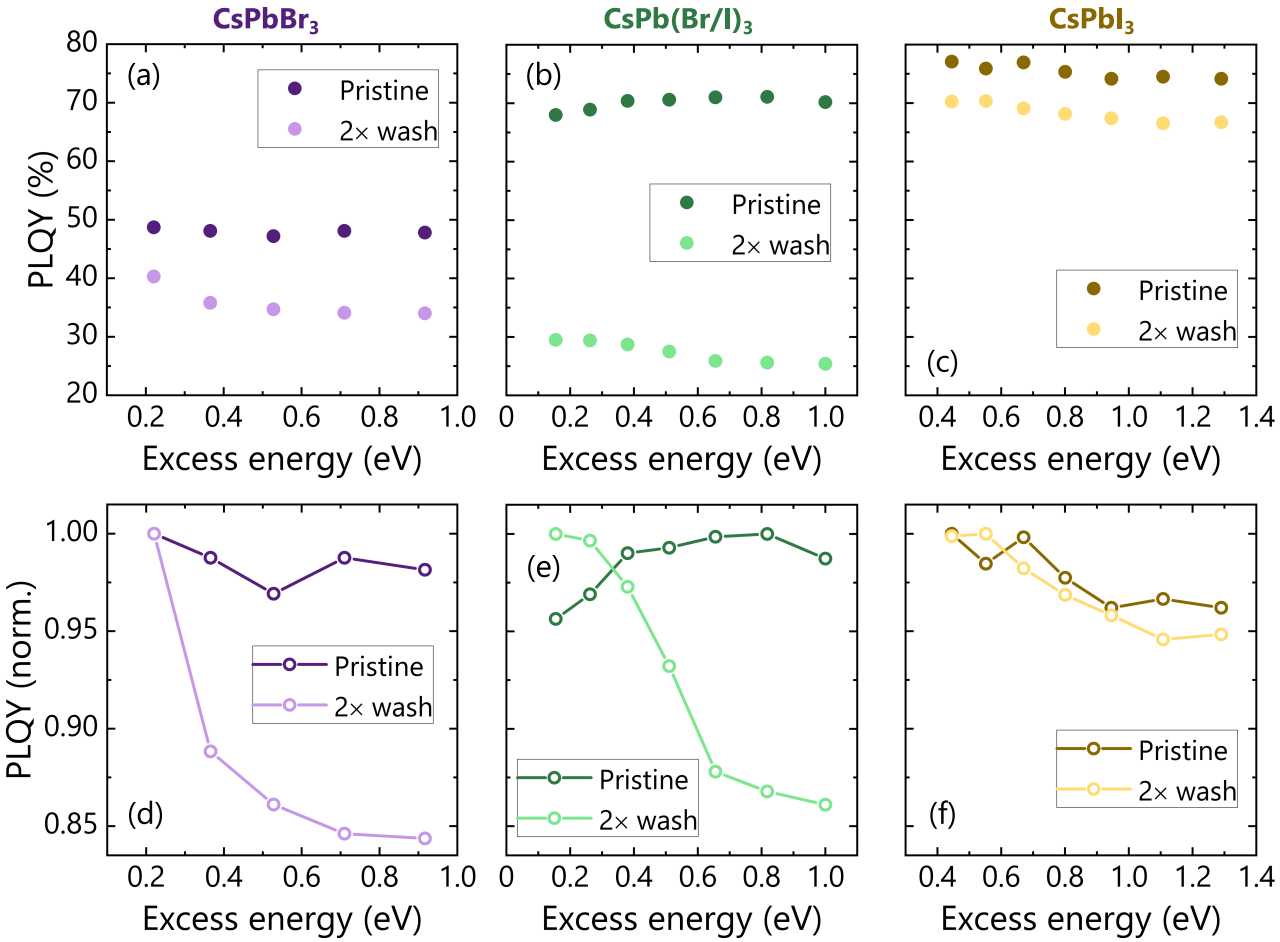


Figure 5.3 – (a-c) Absolute and (d-f) normalised excitation energy-dependent PLQY of $CsPbX_3$ NCs. Data provided by Dr. Junzhi Ye (University of Cambridge).

dependence of the PLQY for each system is investigated. For the $CsPbBr_3$ and $CsPb(Br/I)_3$ NCs, the washed samples show a more obvious decrease in PLQY for excitation further above the band edge. For the I-based NCs, there is minimal dependence of the PLQY on excitation energy for both the pristine and washed samples. Taken together with the compositional analysis after each washing, it appears that the introduction of surface trap states via the removal of surface halides does not influence the hot carrier dynamics of the I-based NCs; but does impact those of the Br- and Br/I-based NCs.

In order to elucidate the differences in hot carrier dynamics between systems in more detail, PPP spectroscopy measurements employing a broadband visible probe (PPP-Vis) were carried out, with the experimental setup described in full detail in Section 3.3.2. In each case, a 400 nm (3.1 eV) pump and a 1300 nm (0.95 eV) push are used. The push arrives 10 ps after the pump, ensuring that it interacts with a purely band-edge (cold) carrier distribution despite the varying

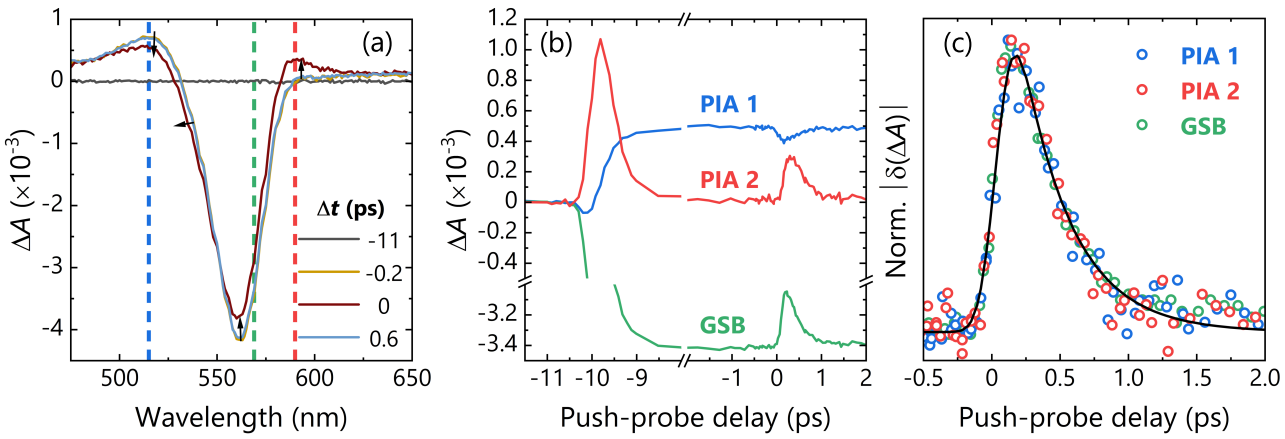


Figure 5.4 – (a) Exemplar TA spectra before, during and after the push arrival; arrows represent direction of change due to push; dashed coloured lines are slices whose kinetics are shown in panel (b). (c) Normalised push-induced bleach kinetics for each region of interest – the bleach recovery time is independent of spectral region chosen for analysis.

band gaps of the studied materials, and thus the nascent hot carriers are formed with the same excess energy in all cases. Figures 5.4a-b exemplify the effect of the push on the TA spectra. The push causes a transient depletion of the GSB and above-gap PIA signal, as well as a change in spectral *shape*: the GSB momentarily extends to higher energies and the sub-gap PIA feature reappears, in keeping with the early-time signal found in two-pulse TAS measurements upon above-gap excitation described in Section 3.3. The region of the spectrum corresponding to the low-energy portion of the GSB for each sample was integrated, and their kinetics analysed. The same bleach recovery time constant is extracted regardless of the portion of the spectrum chosen, as shown in Figure 5.4c, but the GSB is analysed hereinafter to maximise signal-to-noise ratio (SNR). Upon absorption of the push, the GSB is diminished, before recovering to the PP baseline. These temporal and spectral characteristics combined point to the push pulse having the effect of re-exciting a portion of the cold carriers to hot states, and the bleach recovery is attributed to hot carrier cooling. By varying the push fluence, and therefore the hot carrier density, the role of defect density is observed through the hot phonon bottleneck effect. As in Chapter 4, the band-to-band recombination dynamics depend on the pump excitation density and thus PPP-Vis measurements were carried out at a low pump fluence ($\sim 1 \times 10^{12}$ cm^{-2}) to remove the effect of Auger recombination on the hot carrier dynamics.

Figure 5.5 shows how the hot carrier lifetime varies with hot carrier density for the three

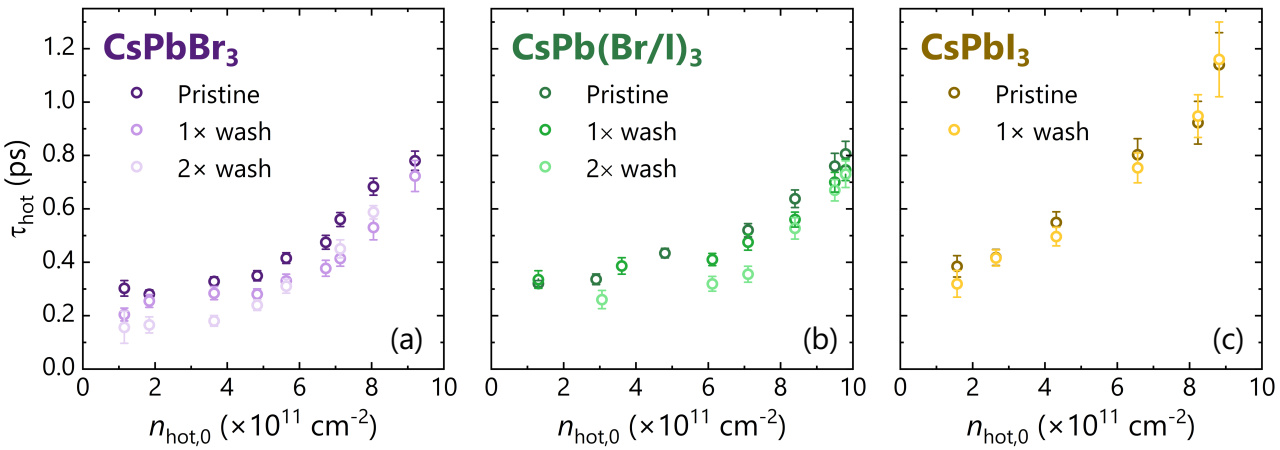


Figure 5.5 – Hot carrier lifetimes as function of initial hot carrier density for (a) $CsPbBr_3$, (b) $CsPb(Br/I)_3$ and (c) $CsPbI_3$.

material systems under study. In Chapter 4, the calculation of precise carrier density was largely precluded by the use of thin-film samples with a NIR probe, however it may be calculated to reasonable accuracy for the solution-phase samples when using a visible light probe here (see Section 3.3.2). Irrespective of composition, all materials show a longer hot carrier lifetime at higher density due to the hot phonon bottleneck. In the case of the Br- and Br/I-based NCs, the hot carrier lifetime is generally shorter for a given hot carrier density in the washed (higher defect density) samples. This effect is attributed to hot carrier trapping, which offers an additional relaxation pathway and thus shortens their lifetime. The difference between pristine and washed samples is diminished at the highest hot carrier densities as the trap states become saturated.[321] In the I-based NCs, the introduction of traps upon washing does not alter the hot carrier dynamics, in keeping with the trends observed for the PLQY measurements.

5.4 Kinetic modelling of hot carrier trapping dynamics

To explain the experimental observations, a numerical kinetic model was developed based on the following system of differential equations, and described schematically in Figure 5.6:

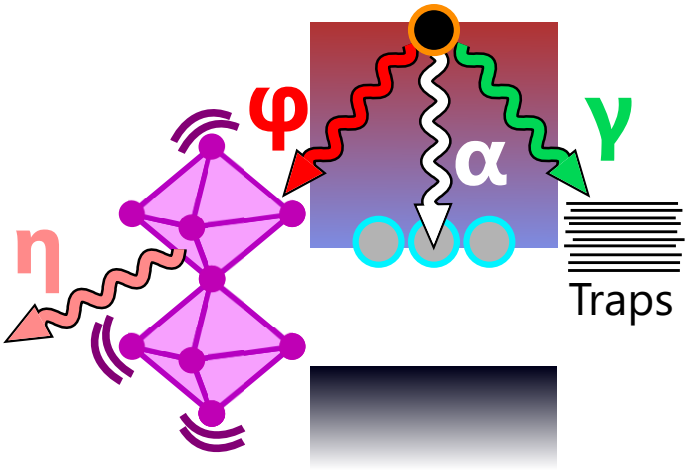


Figure 5.6 – Hot carrier trapping model in $CsPbX_3$ NCs. Labels denote coefficients for α: hot-cold carrier; φ: carrier-phonon; γ: carrier-trap scattering; and η: LO phonon freeing.

$$\frac{\mathrm{d}n_{\mathrm{hot}}}{\mathrm{d}t} = -\alpha n_{\mathrm{hot}} n_{\mathrm{cold}} - \phi n_{\mathrm{hot}} n_{\mathrm{ph}} - \gamma n_{\mathrm{hot}} (N_{\mathrm{t}} - n_{\mathrm{t}}^*) \tag{5.1}$$

$$\frac{\mathrm{d}n_{\mathrm{cold}}}{\mathrm{d}t} = \alpha n_{\mathrm{hot}} n_{\mathrm{cold}} + \phi n_{\mathrm{hot}} n_{\mathrm{ph}} \tag{5.2}$$

$$\frac{\mathrm{d}n_{\mathrm{ph}}}{\mathrm{d}t} = -\phi n_{\mathrm{hot}} n_{\mathrm{ph}} + \eta (N_{\mathrm{ph}} - n_{\mathrm{ph}}) \tag{5.3}$$

$$\frac{\mathrm{d}n_{\mathrm{t}}^*}{\mathrm{d}t} = \gamma n_{\mathrm{hot}} (N_{\mathrm{t}} - n_{\mathrm{t}}^*) \tag{5.4}$$

where α, ϕ, γ and η correspond to rate coefficients for hot-cold carrier, hot carrier-phonon and hot carrier-trap scattering, as well as phonon freeing, respectively. Phonon freeing refers to the process by which LO phonons, after scattering with a hot carrier, dissipate their excess energy to the wider lattice (e.g. via Klemens decay). The total trap density is given by N_{t}, and occupied trap density by n_{t}^*. Just as in the kinetic model in Chapter 4, the hot carrier, cold carrier, vacant and total phonon densities are given by n_{hot}, n_{cold}, n_{ph} and N_{ph}, respectively. Therefore, band-to-band and trap-assisted recombination rates are assumed negligible on the timescales relevant for hot carrier cooling. This is reasonable given the experimental push-induced GSB bleach returns to the PP baseline in all cases.

The Midpoint method was employed for the simulations, where the numerical approximations to Equations 5.1-5.4 are:

$$n_{\mathrm{hot}}(t_{i+1}) \;=\; n_{\mathrm{hot}}(t_i) \;+\; \frac{\mathrm{d}n_{\mathrm{hot}}}{\mathrm{d}t}\left(t_i + \frac{\Delta t}{2},\, n_{\mathrm{hot}}\left(t_i + \frac{\Delta t}{2}\right)\right)\Delta t \;+\; \tilde{I}(t_i)n_{\mathrm{cold}}(t_i) \tag{5.5}$$

$$n_{\mathrm{cold}}(t_{i+1}) \;=\; n_{\mathrm{cold}}(t_i) \;+\; \frac{\mathrm{d}n_{\mathrm{cold}}}{\mathrm{d}t}\left(t_i + \frac{\Delta t}{2},\, n_{\mathrm{cold}}\left(t_i + \frac{\Delta t}{2}\right)\right)\Delta t \;-\; \tilde{I}(t_i)n_{\mathrm{cold}}(t_i) \tag{5.6}$$

$$n_{\mathrm{ph}}(t_{i+1}) \;=\; n_{\mathrm{ph}}(t_i) \;+\; \frac{\mathrm{d}n_{\mathrm{ph}}}{\mathrm{d}t}\left(t_i + \frac{\Delta t}{2},\, n_{\mathrm{ph}}\left(t_i + \frac{\Delta t}{2}\right)\right)\Delta t \tag{5.7}$$

$$n^*_{\mathrm{t}}(t_{i+1}) \;=\; n^*_{\mathrm{t}}(t_i) \;+\; \frac{\mathrm{d}n^*_{\mathrm{t}}}{\mathrm{d}t}\left(t_i + \frac{\Delta t}{2},\, n^*_{\mathrm{t}}\left(t_i + \frac{\Delta t}{2}\right)\right)\Delta t \tag{5.8}$$

where $n\left(t_i + \frac{\Delta t}{2}\right) = n(t_i) + \frac{\mathrm{d}n(t_i)}{\mathrm{d}t}\frac{\Delta t}{2}$, and $\tilde{I}(t_i) = I_{\mathrm{push}} \exp\left(-\frac{t_i^2}{2\sigma^2}\right)$ represents the Gaussian push envelope. The initial boundary conditions imposed for the simulations are:

$$n_{\mathrm{hot}}(i=0) = 0$$

$$n_{\mathrm{cold}}(i=0) = N_{\mathrm{pump}}$$

$$n_{\mathrm{ph}}(i=0) = N_{\mathrm{ph}}$$

$$n^*_{\mathrm{t}}(i=0) = 0$$

For each data set, I_{push} was varied to simulate the push fluence, and N_{t} increased for each antisolvent washing step. The results of the kinetic model are shown for each system in Figure 5.7 with their respective fitting parameters in Table 5.1. The kinetic model reproduces the experimental results for all systems: in the Br- and Br/I-based NCs, the hot carrier lifetime is shorter in the presence of a higher defect density, but this effect is diminished with sufficient hot carrier density due to trap saturation; and defect density does not affect the I-based NCs.

N_{pump} was calculated from F_{pump} via Equation 3.7. The values are very similar across the three different NCs because a similar F_{pump} was used, and each solution was diluted to give approximately the same absorbance at the pump wavelength. The carrier-carrier coupling strength (α) was the same for each material, under the assumption that the choice of halide does not have an effect here in these large NCs, which have similar and small E_{b}.[234] The exciton cooling term in the model for Chapter 4 is excluded here for the same reason.

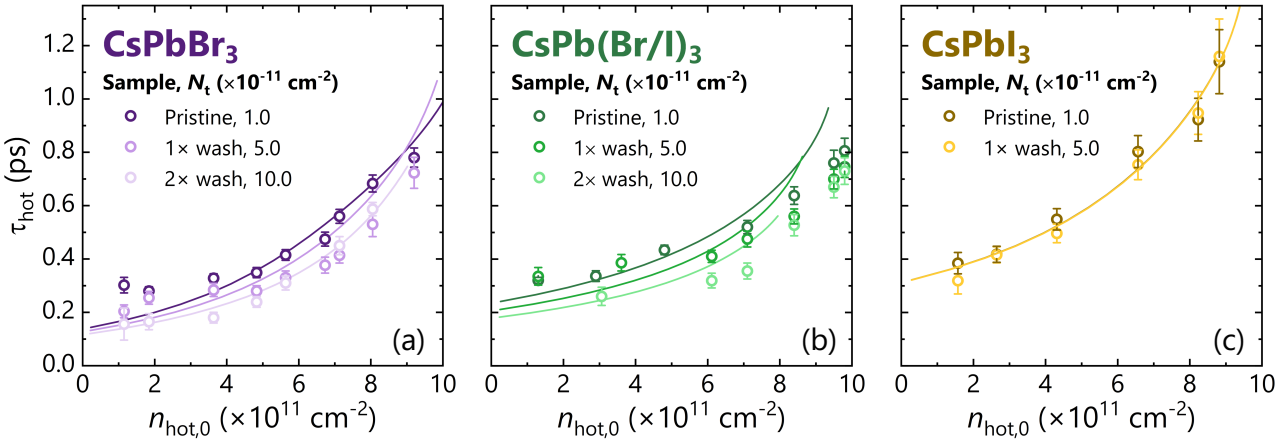


Figure 5.7 – Results from kinetic model of trapping effect on hot carrier dynamics in (a) $CsPbBr_3$, (b) $CsPb(Br/I)_3$ and (c) $CsPbI_3$.

Fit parameter			$CsPbBr_3$	$CsPb(Br/I)_3$	$CsPbI_3$
Pump carrier density	N_{pump}	$(\times 10^{12}$ cm$^{-2})$	1.1	1.0	1.0
Carrier-carrier	α	$(\times 10^{-12}$ cm^2 ps$^{-1})$	1.3	1.3	1.3
Carrier-phonon	ϕ	$(\times 10^{-12}$ cm^2 ps$^{-1})$	7.0	3.5	3.5
Carrier-trap	γ	$(\times 10^{-12}$ cm^2 ps$^{-1})$	1.5	1.5	0.0
Phonon freeing	η	(ps^{-1})	0.15	0.15	0.03
Total phonon density	N_{ph}	$(\times 10^{12}$ cm$^{-2})$	8.0	8.0	5.5

Table 5.1 – Kinetic model fitting parameters for hot carrier trapping in $CsPbX_3$ NCs.

The choice of halide will, however, have ramifications on the lattice structure, and therefore phonon behaviour in each system. The heavier I ions imbue the $CsPbI_3$ NCs with lower frequency phonon modes,[231] represented as a lower phonon density (N_{ph}), and which also results in lower carrier-phonon scattering (ϕ) and phonon freeing (η) rate constants than in $CsPbBr_3$. The closest fit to the data for mixed-halide $CsPb(Br/I)_3$ NCs is obtained when ϕ and η are equal to that found in the $CsPbBr_3$ NCs, tentatively suggesting the phonon spectra are dominated by the presence of Br. However, the carrier-phonon coupling constant extracted for $CsPb(Br/I)_3$ is the same as $CsPbI_3$ NCs, and this inconsistency may therefore represent a limitation of the model.

The carrier-trap scattering coefficient (γ) is negligible in $CsPbI_3$, accounting for the similarities in cooling times between pristine and washed NCs. The value for γ extracted for $CsPbBr_3$ and $CsPb(Br/I)_3$ NCs is non-zero and equal in both cases, tentatively suggesting that LHP

defect tolerance is lost for small inclusions of Br – the precursors for the mixed-halide NCs were mixed at Br:I = 3:7, although compositional analysis from XPS (Figures 5.2d-f) suggest the final (pristine) products have a ratio closer to 4:3. In general, the trend in trapping efficiency follows that of carrier-phonon scattering due to the nature of the halide: lighter halides result in a wider band gap and thus reduced defect tolerance, while also increasing phonon frequency. The caveat to the conclusions herein is the difficulty in accurately extracting trap densities from experimental data, and so this is likely to have a moderate bearing on the final fitting parameters obtained. While the fit to the mixed-halide NCs is the poorest, the qualitative trends are reproduced for physically reasonable fitting parameters. Overall, these results suggest that hot carrier defect tolerance is retained in $CsPbI_3$ NCs, and thus makes them more suitable candidates for hot carrier devices. This is fortuitous given their smaller band gap means hot carriers are formed more readily from any given light source.

5.5 Conclusions

In this Chapter, the defect tolerance of LHP NCs has been assessed and extended to its impact on hot carrier dynamics. This was achieved through a three-pulse variant of the typical broadband visible transient absorption spectroscopy used elsewhere, in order to isolate the hot carrier dynamics from other overlapping spectral and dynamical contributions. The density-dependent hot carrier lifetime was investigated for a range of $CsPbX_3$ nanocrystal compositions: $CsPbBr_3$, $CsPb(Br/I)_3$ and $CsPbI_3$. In each case, additional antisolvent washing steps introduced a greater defect density by stripping halide ions from the nanocrystal surface. The reduced band-edge emission, and shorter hot carrier lifetime of Br-containing nanocrystals suggest that neither cold nor hot carriers are defect tolerant. Conversely, defects in I-based nanocrystals had minimal impact on band-edge emission and hot carrier dynamics, suggesting defect tolerance is retained in these systems. By applying a kinetic model which accounted for hot carrier trapping, the differences in experimental hot carrier lifetime were rationalised.

The results presented suggest care should be taken when employing the commonly used post-synthetic washing steps for $CsPbX_3$ NCs, so as to not impede carrier extraction. Furthermore,

the results offer input for the rational design of PV and LED devices based on $CsPbX_3$ NCs. For example, upon electrical injection above the band-edge, a portion of hot carriers in $CsPbBr_3$ NCs of this size will undergo trapping, thereby lowering the efficiency of blue/green emission. A possible way to circumvent this may then lie in blue-shifting $CsPbI_3$ emission by using smaller NCs. In this regard, an extension of the study herein could investigate whether the defect tolerance is retained in smaller NCs where surface effects are magnified further. Furthermore, the dependence of the dynamics on carrier excess energy should be extended to the three-pulse transient measurements through variation in push wavelength.

6 Hot Carrier Mobility in Lead Halide Perovskite Single-Crystals

Up to this point, hot carrier dynamics have been studied in the context of their time-evolving population density. For working devices, it is also important to understand charge *transport* characteristics such as carrier mobility. To this end, the final variant of PPP spectroscopy employed in this thesis makes use of a THz probe, which offers a non-contact measurement of the hot carrier conductivity. The dynamics observed are distinct from those observed in the NIR-based variants described earlier, alluding to the existence of a previously unaddressed electronic state which suppresses carrier mobility even after intraband relaxation is complete.

6.1 Background and motivation

The performance of a full-stack device is greatly determined by the (opto)electronic properties of the 'active layer' materials discussed in this thesis. The mobility of charge-carriers is one such key performance parameter: in PV devices, a higher mobility in the photo-absorber layer means they may transport over a greater distance prior to recombination, thus a thicker layer can be used which improves light harvesting and therefore PCE; in field-effect transistors (FETs), a higher mobility permits a greater possible switching rate.[322] Myriad techniques exist to measure carrier mobility, such as those based on space-charge-limited current,[323–325] Hall effect,[34,125,326] time-of-flight[327,328] and FET measurements.[329,330] All these have particular demands in terms of device architecture and charge injection conditions which can make the experiments time-consuming and the reported results inconsistent.[331]

$$\mu(\omega) = \frac{\epsilon_0 \, \omega_{\mathrm{p}}^2 \, \tau_{\mathrm{s}}}{eN(1 - i\omega\tau_{\mathrm{s}})} \tag{6.1}$$

Charge-carrier mobility is determined by phonon scattering on sub-picosecond timescales, accounted for in the Drude model in Equation 6.1 as τ_{s} (ϵ_0: vacuum permittivity, ω_{p}: plasma frequency). Therefore, τ_{s}^{-1} lies on the order of 10^{12}–10^{14} s^{-1} and mobile charges show a strong response in the THz frequency range. In other words, while the methods described above are all largely based on applying an electric field in the form of a direct-current (DC) bias in order to perturb carrier transport, the electric field may also be applied *optically*, removing the need for complex electrical contacts. Moreover, while DC methods measure macroscale transport which can be influenced by film morphology and defects, carriers have a few-nm displacement over a THz cycle and thus the *intrinsic* mobility may be measured.[332] THz radiation can now be routinely produced from table-top ultrafast laser sources, making THz spectroscopy a powerful non-contact probe of material conductivity.[333–336]

While the transient spectroscopies introduced thus far based on visible and NIR probes are sensitive to the population of electronic states, combining an ultrafast pump with a delay-controlled THz probe, as in optical pump–THz probe (OPTP) spectroscopy, yields insight into how a system's photoconductivity evolves over time. The photoconductivity ($\Delta\tilde{\sigma}$) of a thin-film sample measured from an OPTP transient ($\Delta E/E$) can be expressed as:[337,338]

$$\Delta\tilde{\sigma}(t,\omega) = e \cdot \mu(\omega) \cdot N_{\mathrm{pump}}(t) \tag{6.2}$$

$$= -\frac{\epsilon_0 c(n_{\mathrm{a}} + n_{\mathrm{b}})}{L} \frac{\Delta E(t,\omega)}{E(\omega)} \tag{6.3}$$

where n_{a} and n_{b} are the refractive indices of the media immediately before and after a thin-film of thickness L, respectively. Combining Equations 6.2 and 6.3, the THz mobility (μ_{THz}) can be calculated, in practice, as follows:

$$\mu_{\mathrm{THz}}(\omega) = \frac{hc^2\epsilon_0(n_a + n_b)}{e\phi\lambda F_{\mathrm{pump}}(1 - R - T)} \frac{\Delta E_{\mathrm{max}}}{E}(\omega) \tag{6.4}$$

where ϕ is the free carrier generation efficiency, often assumed unity for bulk perovskites at room temperature; and λ, F_{pump}, R and T are the pump wavelength and fluence, and sample reflectance and transmittance at that pump wavelength, respectively. The mobility is calculated from the early-time peak THz response ($\Delta E_{\text{max}}/E$) of the sample, as carrier density is most accurately calculated from experimental conditions prior to recombination, and thus so too is the mobility. Comparing calculations from OPTP with the analogous time-resolved microwave conductivity (TRMC) approach – where recombination occurring within the few-ns microwave pulsewidth obfuscates calculation at high carrier density, but which samples mobility over longer distances – can give valuable insight across multiple time- and length-scales in polycrystalline films.[339–341] The early-time OPTP response has been used elsewhere to study processes such as free carrier generation,[342] carrier-phonon coupling[343–345] including polaron formation,[138,346–348] and hot carrier cooling.[349,350] The THz probe waveform can also be sampled in the time-domain, yielding *spectral* information on the amplitude and phase (via Fourier transformation, as described in Section 3.3.3) of the carrier response. The frequency-dependent response can be used to infer the extent of localisation of charges.[351]

Extending the OPTP technique with the use of an intraband push represents a natural progression for studying hot carrier dynamics. Indeed, three studies have been reported (at the time of writing, to the best of the author's knowledge) employing an optical-pump–NIR-push–THz-probe (PPP-THz) scheme in this pursuit. Wang & Bonn *et al.*[352] reported a transient *increase* in conductivity in the double perovskite $Cs_2AgBiBr_6$ upon push re-excitation. This was ascribed to hot holes having a *higher* mobility than when electronically cold, on account of their reduced momentum scattering (longer τ_s) extracted from photoconductivity spectra. This is in contrast to other band-transport semiconductors which generally display increased mobility after carrier relaxation;[349] while the time-invariant plasma frequency (ω_p) indicated the observations were not due to a change in effective mass (i.e. DOS), presumably due to the specific band structure in these materials.

Meanwhile, Herz & Johnston *et al.*[235] studied the hot carrier dynamics in the tin-based perovskite $FA_{0.83}Cs_{0.17}SnI_3$ using PPP-THz, observing a *decrease* in the transient THz response

upon push re-excitation. Following analysis of the Lorentzian line shape in the photoconductivity spectra, it was concluded that hot carriers undergo stimulated THz emission. That is, rather than any effect of the relative mobility of – and therefore THz absorption by – hot and cold carriers, it was deemed that the emission of THz by hot carriers enhanced the detected transmission (in analogy to the SE features described for broadband TAS in Section 3.3.2). Furthermore, the hot carrier lifetime was found to depend inversely on excess energy: cooling from 0.6 eV or 1.1 eV above the band edge had time constants of 0.9 and 0.2 ps, respectively. This ostensibly conflicts with a phonon-limited carrier cooling model wherein the dissipation of greater excess energy ought to be slower due to the need to couple to more phonons, and so was attributed to the effect of the large reservoir of cold hole states that arise from the oxidation of Sn^{2+} – a greater energy difference creates a stronger driving force for cooling via hot-cold carrier scattering. However, it should be noted that Wang & Bonn *et al.*[352] suggest this can also be explained by "the enhanced density of charge states and efficient phonon emission before hot carriers reach full thermalisation".

While the assumed origin of the push-induced bleach differs between these two studies, they both ultimately depend directly on the presence of hot carriers. As such, the bleach recovery time should increase with higher push fluence due to the hot phonon bottleneck effect described earlier, which prolongs the population of hot carriers. However, no such effect was reported in either case. Shortly after their publication, Bakulin *et al.*[233] reported a comparison of the dynamics from PPP-THz and PPP-NIR on $MAPbI_3$, observing a decrease in transient photoconductivity upon push re-excitation (à la Herz *et al.*[235]). Under similar pump and push conditions (i.e. energy, fluence), the dynamics of the THz and NIR bleach recovery differed in two important ways: (i) the THz recovery was consistently longer, suggesting carrier mobility remains suppressed for some time after intraband carrier relaxation has occurred; and (ii) did not show the clear push fluence-dependence observed with a NIR probe, meaning the THz probe is not directly sensitive to the hot carrier density. To explain this, the authors invoked a three-level model described schematically in Figure 6.1, wherein intraband relaxation of hot carriers (state "A") via phonon emission leads to an increase in temperature of the lattice immediately surrounding the charge. This hot local lattice ("B") then sustains the low mobility of the

nascent cold carrier, before equilibration of temperature with the wider lattice returns the carrier mobility to the 'pre-push' level ("C").

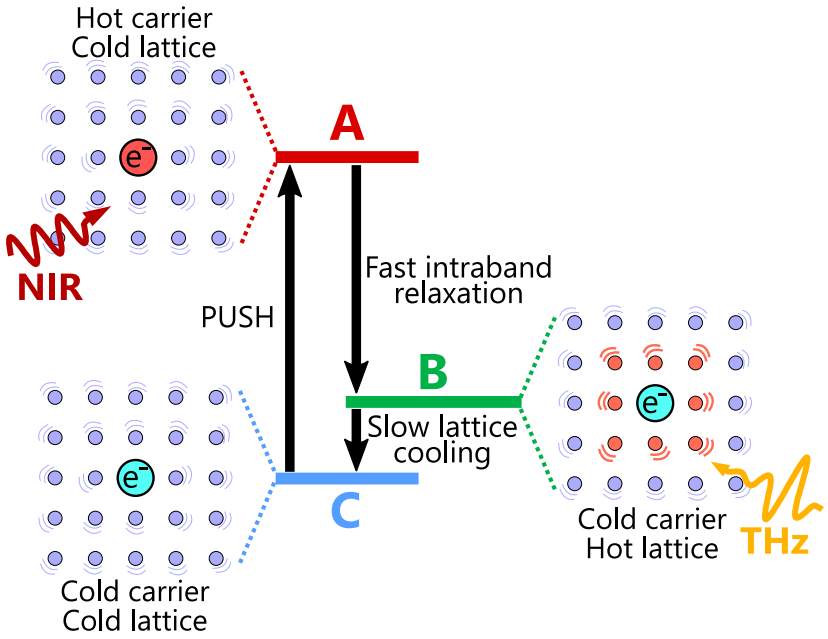


Figure 6.1 – Energy state diagram for PPP-THz. Intraband relaxation loads energy into phonons directly coupled to the carrier. Carrier mobility is suppressed until the resulting hot lattice state further dissipates excess heat.

In this Chapter, the hot carrier dynamics obtained from PPP-THz of high-quality single-crystalline $CsPbBr_3$ are reported in order to further address the discrepancies above. The very large domains (~1 mm[353]) formed in these vapour-deposited films mean carriers are less encumbered by grain boundaries,[354] leading to a higher average mobility and thus a greater THz response. Along with high intrinsic stability and well-characterised hot carrier dynamics, these materials are a useful model system to investigate further.

6.2 Specific experimental details

6.2.1 Sample preparation and characterisation

Samples were prepared by Dr Vladimir Bruevich (Rutgers University) via a procedure described in Ref. [353]. CsBr and $PbBr_2$ precursors (Sigma-Aldrich, 99.999%) were mixed in a 1:1 molar ratio and reacted by heating in an alumina boat at 380 °C for 12 h in an inert atmosphere. Muscovite mica (Electron Microscopy Sciences) was cleaved in air just prior to growth. Separate

alumina boats containing the precursor and mica substrate were loaded into a custom-designed chemical vapour deposition reactor consisting of a quartz tube in a tube furnace. The apparatus was evacuated and purged several times with the ultra-high purity He carrier gas, after which the gas flow and pressure were stabilised at 100 sccm and 0.1 bar, respectively. The precursor was then melted at 560 °C, with the mica placed downstream and heated to 500 °C, resulting in sublimation of contaminants and deposits from its surface. After stabilising the temperature and its gradient along the furnace, epitaxial growth of $CsPbBr_3$ on mica was initiated by shifting the precursor and furnace position with respect to the mica by 1 inch in the opposite direction to gas flow, thereby cooling the mica slightly while maintaining the precursor temperature. The growth duration was 15 min. The growth was terminated abruptly by withdrawing the precursor from the heated zone without moving the mica substrate. The furnace was then turned off and the substrate allowed to cool gradually to room temperature.

6.2.2 PPP-THz

Ultrafast experiments were conducted using the setup described in Section 3.3.3. A 400 nm pump, generated by SHG of the 800 nm fundamental laser output, was used to photoexcite the sample. The signal wavelength from TOPAS-II was tuned to ∼1325 nm, corresponding to an idler wavelength of ∼2020 nm. Both were used in the PPP-THz experiments presented, and were chosen as they gave reasonable difference in hot carrier excess energy (∼0.94 eV vs ∼0.61 eV) while also being near the peak of the OPA tuning curve and therefore yielding sufficient light intensity. Temperature-dependent measurements were performed using a cryostatic sample stage (HFS600E-PB4, Linkam) and the entire sample area was encased in a dry air-purged enclosure. This lowered the humidity to ∼0%, preventing ice build-up on the stage window at low temperatures, while also minimising THz transmission losses due to water vapour absorption and limiting sample degradation. The push-induced bleach recovery is convolved with a Gaussian of width $\sigma = 200$ fs for all fits.

6.3 Results and discussion

As with all PPP schemes in this thesis, the first port of call is to carry out preliminary two-pulse PP measurements to understand the underlying recombination kinetics of band-edge carriers. Figure 6.2a shows exemplar time-domain THz waveforms at selected pump-probe delays. Optical excitation alters the photoconductivity of the material, and therefore its interaction with the THz probe. Fourier transformation yields the complex photoconductivity spectra shown in Figure 6.2b. The peak at ∼1 THz can be tentatively assigned to the non-Drude behaviour observed in LHPs as a result of strong carrier-phonon coupling.[233] A full analysis of the frequency-resolved response will be the subject of a separate investigation, and the remainder of this Chapter will focus on hot carrier dynamics.

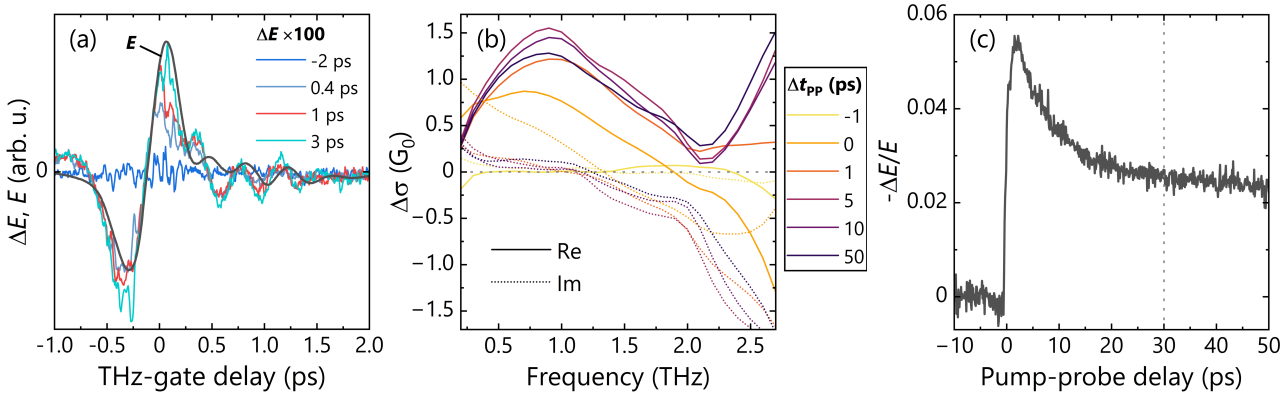


Figure 6.2 – (a) Time-domain THz waveform at selected pump-probe delays. (b) Frequency-domain THz spectra at selected pump-probe delays. (c) OPTP kinetics for $CsPbBr_3$ single-crystals. Dashed reference line denotes push arrival time in PPP-THz transients below.

Figure 6.2c shows the PP transient obtained at room temperature under a pump fluence of 200 µJ cm^{-2}. The THz-gate delay was fixed at the maximum field point and thus the kinetics are effectively 'integrated' across the probe spectral bandwidth. While this ostensibly represents a higher pump fluence used than for PPP measurements in Chapters 4 and 5, this is justified for the following reasons: (i) due to limitations of the experimental setup described later, the SNR is intrinsically lower and so this may be boosted by using a higher pump fluence; and (ii) the fast Auger component that has hitherto been avoided by employing a low fluence, is not as dominant as expected if an equivalent fluence were used on the NIR- and visible-probe setups described in Chapters 4 and 5, and so is clearly not manifesting as correspondingly high carrier

densities. This may be due to a difference in beam profiles between setups.

As described in Section 6.1, the principal aim of this portion of the thesis is to re-inspect the discrepancies between the currently existing works employing PPP-THz, while complementing these studies by investigating the dependence of the system response to the amount of excess energy imparted to the carriers. Figure 6.3 displays the response of the transients separately to a ∼1325 nm and ∼2020 nm push pulse. In both cases, the push arrived 30 ps after the pump to minimise the impact of early-time Auger dynamics. The transient THz response is diminished upon push re-excitation, in keeping with observations employing a NIR probe.

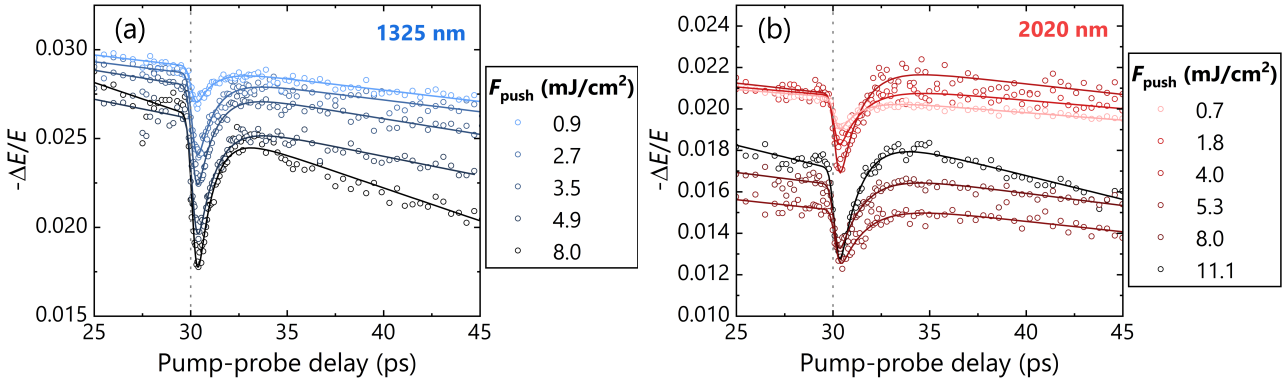


Figure 6.3 – PPP-THz transients for $CsPbBr_3$ single-crystals with (a) 1325 nm and (b) 2020 nm push. Solids lines are Gaussian-convolved exponential decay fits to push recovery.

By altering the fluence of the push, and therefore the resulting hot carrier density, two clear differences are observed with regards to the subsequent recovery of the transient to the 'pre-push' regime depending on the choice of probe, as summarised in Figure 6.4: employing a THz probe here, the extracted time constants show negligible push fluence-dependence and are consistently longer than with a NIR probe, irrespective of excess carrier energy. This is in keeping with the work reported earlier on polycrystalline $MAPbI_3$ by Bakulin *et al*,[233] which suggests separate states are being probed under THz and NIR illumination. Concretely, the results here for single-crystalline $CsPbBr_3$ suggest that the energy dissipated during intraband relaxation of hot carriers is initially contained in the lattice immediately surrounding the carrier. This local heating effect prolongs the suppression of the carrier mobility, and therefore the push bleach recovery, until the excess energy is further dissipated to more distant lattice sites that are decoupled from the carrier. At the same push energy, the recovery time obtained here for a

Cs-based LHP is also longer than that of the MA-based LHP in Ref. [233], which is consistent with another report that tracked the initial rise in two-pulse OPTP transients.[355] This may be attributed to the faster dissipation rate of the hot local lattice provided by the MA cation. While the intrinsic intraband relaxation rate is faster in Br-based LHPs than their I-based counterparts,[231] this is clearly not rate-limiting in the THz response.

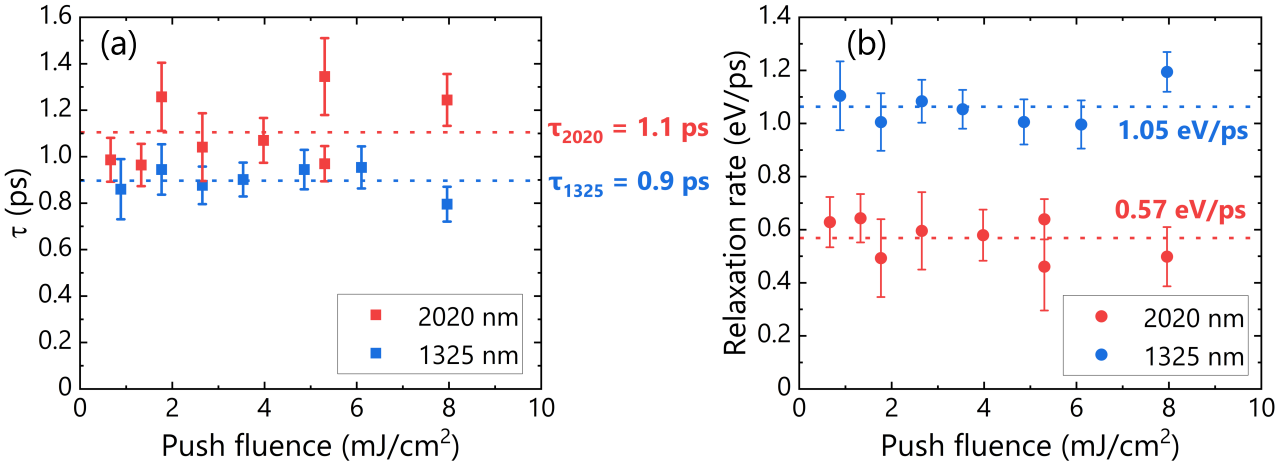


Figure 6.4 – (a) Fluence-dependent push-induced bleach recovery lifetimes at 1325 and 2020 nm push; and (b) corresponding energy dissipation rates.

Notably, the bleach recovery time is consistently shorter when using the higher-energy 1325 nm push (0.9 ± 0.1 ps) than at 2020 nm (1.1 ± 0.1 ps, Figure 6.4a), corresponding to a two-fold increase in energy relaxation *rate*, as shown in Figure 6.4b. This holds similarities with the work of Herz *et al.*,[235] who attributed this effect to the background cold holes: higher-energy carriers experience greater hot-cold carrier scattering rates, thereby increasing the rate of energy dissipation. Across the same span in energies, the relative difference was instead a factor of four, which may be due to the greater prevalence of hole-doping in the Sn-based perovskites studied therein. The use of more stable, high quality Pb-based perovskite single-crystals may explain the weaker dependence observed here.

The assumption above is that the same effect could not be accounted for if carrier-phonon coupling dominated the relaxation mechanism: greater excess energy ought to require interaction with a larger number of phonons, thereby slowing intraband carrier relaxation and showing the reverse dependence to that observed. In the absence of direct evidence for this, an alternative explanation could be that in creating carriers with greater excess energy, they may then cou-

ple to higher frequency phonon modes inaccessible to lower-energy carriers, instead leading to higher relaxation rates. Both of these contrasting hypotheses are also built within the framework that the hot carrier mobility is directly responsible for the THz response, rather than the hot lattice model proposed herein. In principle, the hot local lattice model is more consistent with a hot-cold carrier scattering effect given the results obtained: if more of the 'heat' from intraband relaxation is instead deposited into the reservoir of cold carrier states, the coupled lattice ought to then be able to more efficiently dissipate this energy, and the bleach recovery time shortened.

To resolve the contributions of carrier-carrier and carrier-phonon scattering, the temperature-dependence of the bleach recovery dynamics was investigated. In principle, at lower temperatures the higher carrier mobility found in these band-like semiconductors ought to yield higher carrier-carrier scattering rates. Meanwhile, lower temperatures should simultaneously depopulate phonon modes, making energy dissipation via a carrier-phonon scattering mechanism less efficient. As such, the bleach recovery lifetime should be shorter at low temperature if the hot-cold carrier scattering mechanism were dominant, but longer if dominated by carrier-phonon coupling.

Some preliminary insight can be obtained from the temperature-dependent early-time PP ('push off') dynamics following above-gap excitation. At lower temperatures, a smaller proportion of excitons dissociate which diminishes free carrier density. However, those free carriers have a higher mobility due to the band-transport exhibited by bulk LHPs. Figure 6.5a shows how the relative contributions of these factors results in a net increase in peak photoconductivity at lower temperature. The dynamics also become noticeably faster on <10 ps timescales due to the higher rate of Auger-type scattering that also arises from the higher carrier mobility.[356] At the very earliest times (<2 ps), Figure 6.5b shows how the ingrowing component of the rise becomes slower at lower temperature. Within the model described above, this can be attributed to slower hot lattice cooling that results from the deactivation of the phonon modes that shuttle heat away from the carrier. While this points to an effect of carrier-phonon coupling on the differences observed between push energies in three-pulse PPP-THz measurements, it does not

rule out the role of cold carriers in and of itself. As mentioned previously, the single excitation scheme used in two-pulse PP creates all carriers with the same energy, and thus three-pulse PPP is required to discern the effect of the reservoir of cold carriers.

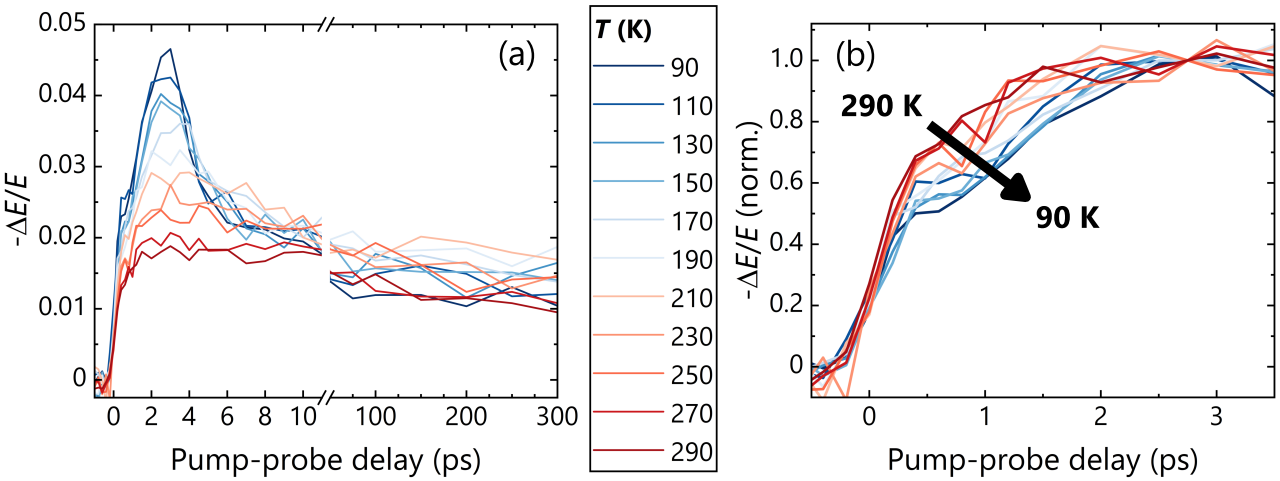


Figure 6.5 – Temperature dependence of the PP-THz dynamics under $\lambda_{\text{pump}} = 400$ nm, $F_{\text{pump}} = 100$ µJ cm^{-2}.

Figure 6.6 shows the PPP-THz transients from 270 to 120 K, obtained with a 2020 nm push. F_{pump} and F_{push} were kept constant at 200 µJ cm^{-2} and 18 mJ cm^{-2}, respectively. Due to the faster early-time PP dynamics at low temperature just described, the push is adjusted to arrive earlier (∼10 ps) than the previous experiments conducted at room temperature, ensuring ample free carrier density for interaction with the push on its arrival. The higher mobility of band-edge carriers at lower temperature also leads to an increase in the pre-push PP transient signal.

At 273 K, the push-induced bleach recovers to the PP trajectory, which is reminiscent of the transients described earlier in Figure 6.3. However, with decreasing temperature, the bleach recovery departs from this behaviour: rather than solely returning to the PP baseline, there is an overshoot followed by a fast decay. This points to the presence of additional dynamics induced by the push at lower temperatures. In principle, multiphoton push absorption could produce more carriers in the CB, increasing the photoconductivity of the sample and thus THz absorption. However, there is no clear reason why this would become more apparent at lower temperature given the minimal change in band gap, and absence of phase transitions in this temperature range for $CsPbBr_3$.[357] Another possible source for this behaviour is the larger

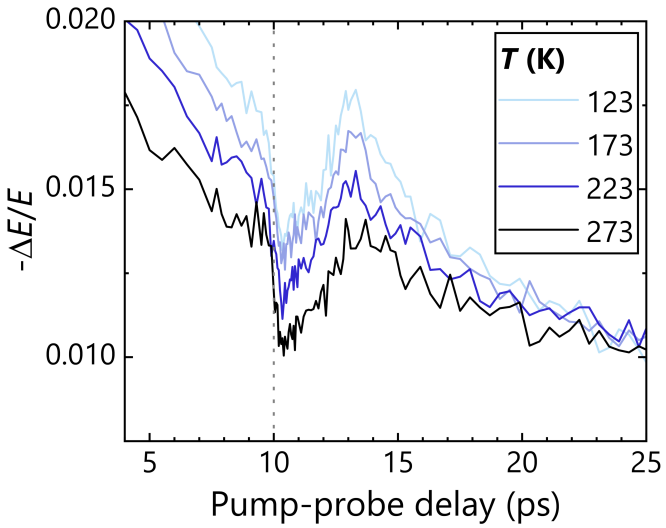


Figure 6.6 – Temperature dependence of the PPP-THz bleach recovery timescales under λ_{pump} = 400 nm, F_{pump} = 200 μJ cm^{-2}, λ_{push} = 2020 nm, F_{push} = 18 mJ cm^{-2}.

presence of bound excitons at low temperature. In this case, the push may also induce exciton dissociation, producing more free carriers and increasing photoconductivity; while simultaneously re-exciting already-free carriers to give the characteristic absorption reduction seen thus far. The difference in timescales between re-forming excitons and cold carriers would explain the observed derivative-like shape of the transient response. This push-induced exciton dissociation has also been used to study free charge generation in organic PV systems via PPP spectroscopy.[358–361]

6.4 Kinetic modelling of *T*-dependent PPP-THz

To test the above hypothesis regarding excitonic effects in lower temperature PPP-THz transients, a kinetic model was derived, as described schematically in Figure 6.7 and in the following set of coupled differential equations:

$$\frac{\mathrm{d}n_{\mathrm{HC}}}{\mathrm{d}t} = \tilde{I}_{\mathrm{c}}(t)n_{\mathrm{CC}} + \tilde{I}_{\mathrm{x}}(t)n_{\mathrm{X}} - k_{\mathrm{cool}}n_{\mathrm{HC}} \tag{6.5}$$

$$\frac{\mathrm{d}n_{\mathrm{CC}}}{\mathrm{d}t} = -\tilde{I}_{\mathrm{c}}(t)n_{\mathrm{CC}} + k_{\mathrm{d}}n_{\mathrm{X}} - k_{\mathrm{f}}n_{\mathrm{CC}} + k_{\mathrm{l}}n_{\mathrm{HL}} \tag{6.6}$$

$$\frac{\mathrm{d}n_{\mathrm{HL}}}{\mathrm{d}t} = k_{\mathrm{cool}}n_{\mathrm{HC}} - k_{\mathrm{l}}n_{\mathrm{HL}} \tag{6.7}$$

$$\frac{\mathrm{d}n_{\mathrm{X}}}{\mathrm{d}t} = -\tilde{I}_{\mathrm{x}}(t)n_{\mathrm{X}} + k_{\mathrm{f}}n_{\mathrm{CC}} - k_{\mathrm{d}}n_{\mathrm{X}} \tag{6.8}$$

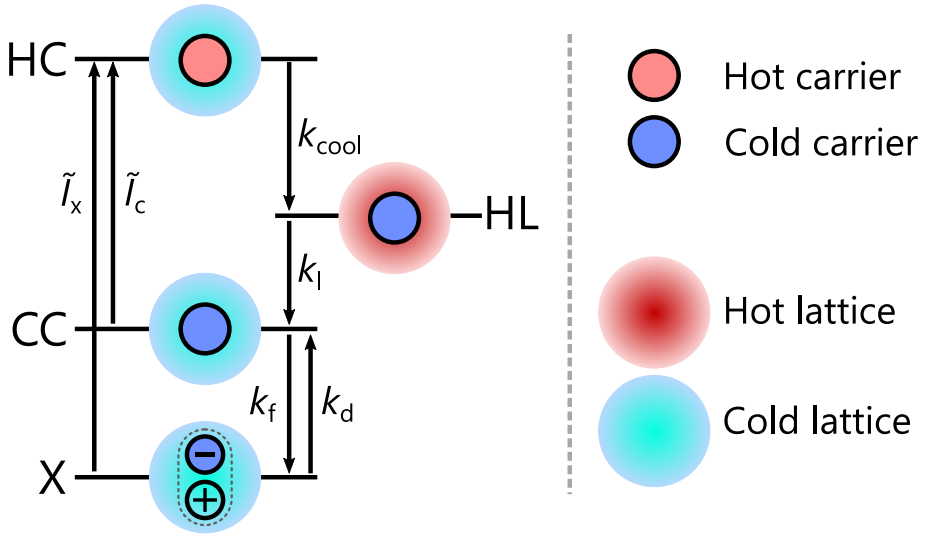


Figure 6.7 – Schematic diagram for the kinetic model used to simulate exciton contribution to temperature-dependent PPP-THz transients.

where $\tilde{I}(t) = I \exp\left(-\frac{(t-t_{\text{push}})^2}{2\sigma^2}\right)$. The following initial boundary conditions are imposed:

$$n_{\text{CC}}(t=0) = N_{\text{pump}} \tag{6.9}$$

$$n_{\text{HC}}(0) = n_{\text{HL}}(0) = n_{\text{X}}(0) = 0 \tag{6.10}$$

The simulated kinetics are performed using the Euler method. At each time point, the photoconductivity is calculated from the sum of the contributions by each species:

$$\Delta\sigma(t) = e\sum_i \mu_i n_i(t) \tag{6.11}$$

$$= e\left[\mu_{\text{HC}} n_{\text{HC}}(t) + \mu_{\text{CC}} n_{\text{CC}}(t) + \mu_{\text{HL}} n_{\text{HL}}(t) + \mu_{\text{X}} n_{\text{X}}(t)\right] \tag{6.12}$$

Representative photoconductivity kinetics for 'high-T' and 'low-T' are given in Figure 6.8. In the case of high-T, $k_{\text{d}} > k_{\text{f}}$, denoting the propensity for exciton dissociation; and at low-T, $k_{\text{d}} < k_{\text{f}}$, denoting the propensity for exciton formation. The simulations are allowed to run from 0 ps, assumed to be the point of photoinjection by the pump, at which point all ESs exist as cold carriers. Subsequently, the cold carriers equilibrate with excitons according to the balance of k_{d} and k_{f}, leading to an initial decrease in photoconductivity. The push arrives after 10 ps, optically re-exciting a portion of excitons and cold carriers according to I_{x} and

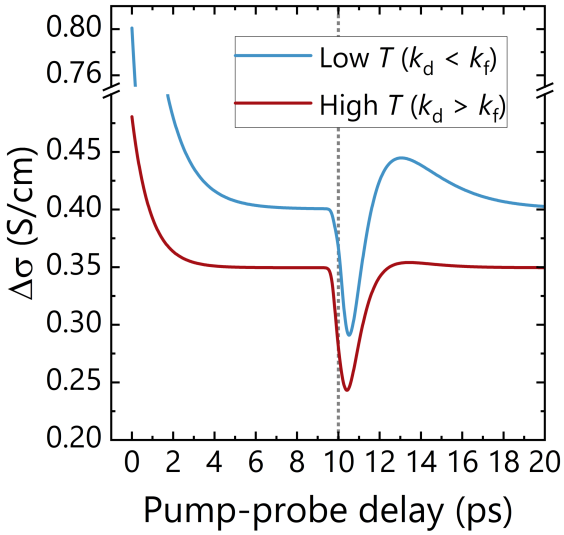


Figure 6.8 – Simulated temperature-dependent photoconductivity transients from the kinetic model described herein. The contributions of exciton dissociation and formation may explain the experimental characteristics observed.

I_c, respectively, which represent the relevant absorption cross-sections to the hot carrier state. $I_x < I_c$ is assumed due to the lower density of exciton states than at the band-edge, and both temperature-independent. Alongside the parameters displayed in Table 6.1, the qualitative experimental trends are reproduced: lower temperatures increase the pre-push photoconductivity due to the net effect of higher carrier mobility despite lower free carrier density; and the post-push dynamics exhibit the typical bleach, followed by a pronounced rise and decay feature with respect to the pre-push baseline. Within the model described, this can be attributed to push-induced exciton dissociation and subsequent re-formation via a step-wise mechanism: X,CC $\rightarrow$ HC $\rightarrow$ HL $\rightarrow$ CC $\rightleftharpoons$ X.

For simplicity, the exciton mobility is assumed negligible relative to free carriers in the simulations. The hot carrier mobility is assumed to be marginally smaller[349] than the cold carrier density calculated from FET measurements.[353] The hot lattice state is assumed to have a mobility intermediate of free carriers and excitons. At low temperatures, the mobilities of free carriers are higher due to the expected increase in phonon scattering times. Intraband relaxation is assumed temperature-independent and faster than the hot lattice cooling, whose high-temperature rate constant is taken from the bleach recovery time extracted in Figure 6.4a, and becomes slower at low temperature due to phonon deactivation. At low temperature,

Parameter			Low T	High T
Pump carrier density	N_{pump}	($\times 10^{17}$ cm^{-3})	1.0	1.0
Free carrier push absorption	I_{c}	(ps^{-1})	0.3	0.3
Exciton push absorption	I_{x}	(ps^{-1})	0.1	0.1
Intraband relaxation	k_{cool}	(ps^{-1})	3.3	3.3
Hot lattice cooling	k_{l}	(ps^{-1})	0.6	0.9
Exciton dissociation	k_{d}	(ps^{-1})	0.4	0.8
Exciton formation	k_{f}	(ps^{-1})	0.4	0.3
Hot carrier mobility	μ_{HC}	(cm^2/Vs)	40	25
Cold carrier mobility	μ_{CC}	(cm^2/Vs)	50	30
Hot lattice mobility	μ_{HL}	(cm^2/Vs)	10	10
Exciton mobility	μ_{X}	(cm^2/Vs)	0	0

Table 6.1 – Kinetic model parameters for temperature-dependent PPP-THz simulations.

exciton formation is still slower than hot lattice decay, leading to the additional post-push rise and decay in photoconductivity. Adding band-to-band recombination would facilitate directly fitting the PPP-THz transients, and may allow extraction of physically meaningful hot lattice cooling constants as a function of temperature. However, the difference in absorption cross-sections, I_{x} and I_{c}, would need to be known *a priori*; the temperature-dependence of the intraband relaxation rate calculated, possibly from PPP-NIR experiments; and the balance of k_{d} and k_{f} quantitatively related to T and E_{b}, perhaps by the Saha equation described in Chapter 4.

6.5 Conclusions

In this Chapter, THz radiation was used as a non-contact probe of the hot carrier mobility dynamics in $CsPbBr_3$ single-crystals. The high-quality film morphology yields a strong response due to the high average mobility of carriers. The push-induced bleach recovery was shown to be density-independent, and consistently longer than when probed in the near-infrared. This implies the existence of a hot local lattice state, which temporarily suppresses carrier mobility even after intraband relaxation has occurred. At larger initial excess carrier energy, the recovery

is faster – potentially due to strong scattering with the reservoir of cold carriers. To confirm this, the temperature-dependence of the response was assessed, however this was complicated by overlapping excitonic features at low temperature, as confirmed by the kinetic model developed.

7 Summary and Outlook

In this thesis, novel ultrafast spectroscopic tools have been employed to elucidate the underlying photophysics of lead halide perovskites (LHPs), which have recently emerged as forerunners for next-generation optoelectronic devices. Specifically, the investigations targeted the mechanisms through which energy is dissipated following the absorption of light with energy in excess of the band gap. This "hot carrier cooling" imposes a limit on solar cell efficiency, and thus demands comprehensive interrogation. Hot carrier dynamics have been shown to depend on their interaction with the lattice via phonons and trap states, as well as with other carriers. Therefore, these investigations present vital insight for the rational design of devices that directly depend on hot carriers, such as hot carrier solar cells and lasers; while the fundamental insight into coupling between photophysical species is more broadly relevant for any application.

The vast majority of transient spectroscopies employed elsewhere use a two-pulse pump-probe (PP) scheme. Therein, the pump pulse transits the system to an excited state, and its evolution is then monitored by the probe. Hot carrier cooling has been shown to slow at higher excitation densities due to the "hot phonon bottleneck effect", however this can be obscured by many-body Auger recombination which is also strongly density-dependent. The hallmark of this thesis has been the application of multi-pulse pump-*push*-probe (PPP) spectroscopy to isolate hot carrier dynamics from the various other processes occurring on similar timescales. Herein, the push pulse optically re-excites carriers from the band-edge, modulating the transient signal, whereafter its recovery is dependent on hot carrier dynamics. As a result, many-body recombination can be excluded by judicious choice of pump intensity; and the hot phonon bottleneck isolated through controlling the push intensity. Compared to two-pulse methods, an additional benefit of PPP lies in the ability to form hot carriers in an environment containing a background of

cold carriers, and therefore elucidate the role of hot-cold carrier scattering. Furthermore, by investigating the response of hot carriers across a wide range of the electromagnetic spectrum (ultraviolet-terahertz), various aspects of their dynamics are divulged.

In **Chapter 4**, the effect of confinement on the hot carrier cooling dynamics of LHP nanomaterials was assessed using a near-infrared probe. Ostensibly, the discretisation of band continua due to confinement ought to slow hot carrier cooling if the energy spacing is greater than that of the coupled phonons. This *phonon bottleneck* would presumably then lead to a more pronounced hot phonon bottleneck. In the results presented, the hot phonon bottleneck was instead shown to be suppressed in more confined systems characterised by a larger exciton binding energy. This suppression was attributed to an alternative cooling pathway mediated by energy transfer to cold carriers, which becomes enhanced upon further confinement of charges. Through the developed kinetic model, this could be quantitatively related to the exciton binding energy. This work therefore also highlights the importance of studying the density-dependence of hot carrier cooling when comparing different systems. Discrepancies between works elsewhere may well be due to the use of only a single excitation regime to study an intrinsically density-dependent phenomenon. While this study used a sample of nanomaterial classes spanning weak to strong confinement regimes, the 'resolution' could be improved in **future work** by studying a larger sample set with smaller step changes in confinement. Work is currently underway in the group in studying the hot phonon bottleneck behaviour in a range of 2D nanoplatelet systems with monolayer-fidelity over their thickness. In principle, any inflection point in the hot phonon bottleneck dependence on exciton binding energy could also be assigned tentatively to the 2D-3D transition of optoelectronic behaviour in these systems.

In **Chapter 5**, the role of defects in LHP nanocrystals (NCs) was extended to their impact on hot carrier dynamics. Antisolvent washing steps were used to systematically introduce further defects by stripping halide ions from the NC surface. This was then surveyed over a range of compositions: $CsPbBr_3$, $CsPb(Br/I)_3$ and $CsPbI_3$. In this case, a broadband visible probe was employed, and the hot carrier lifetime was shown to be quenched in washed Br-containing NCs, while no effect was observed in washed I-pure NCs. At the highest hot carrier densities, the effect of trap states was diminished due to saturation. The composition-related

trends were in keeping with the relative photoluminescence quantum yields of each system, suggesting that both hot and cold carriers are defect tolerant in $CsPbI_3$, yet defect intolerant in the wider-gap Br analogues. A potential avenue for **future work** is in determining the size-dependence of the defect tolerance of $CsPbI_3$. If the hot carrier defect tolerance were sustained in smaller NCs, this may be a promising pathway for blue-shifting the emission, particularly in lasing applications where hot carrier dynamics are key. In analogy to other studies employing hole scavengers as CdSe NC capping layers,[193,196] it remains a possibility that a confinement regime exists wherein trapping reduces carrier-carrier scattering and thus prolongs hot carrier lifetime and/or the amplifies the hot phonon bottleneck effect. Finally, the interpretation of broadband visible transient absorption data for both two- and three-pulse approaches should be systematically compared for the current system, which may help explain current discrepancies in the literature.[239]

In **Chapter 6**, a variant of the three-pulse technique was employed using THz radiation as a non-contact probe of the hot carrier mobility dynamics. Here, the push-induced bleach recovery was prolonged and independent of fluence, suggesting a separate state was dominating the response over that observed in Chapters 4 and 5. This was assigned to the formation of a hot local lattice formed by the initial deposition of excess carrier energy, which lowered carrier mobility until further dissipation had occurred. The excess energy-dependence was investigated, which pointed to the influence of cold carriers. Temperature-dependent measurements were performed to confirm this, however this was obscured by the additional contributions of excitons at lower temperatures. The key limitation of this work was high noise levels, which meant experiments needed to be averaged over extended time periods. To this end, the setup is currently being upgraded with a new laser source (Pharos, Light Conversion) which should offer better shot-to-shot stability and higher peak power in **future work**. The sample region of the optical setup will also be increased in size, permitting the inclusion of bulky apparatus such as the cryogenic stage to be positioned more ideally at the beam focal point. As a result, signal convergence will be attained in shorter time periods, facilitating the extension of measurements into the frequency domain, and hitherto inaccessible materials with intrinsically lower THz response (carrier mobility), such as organics.

References

Note to digital readers: where available, the URL for each source cited herein can be accessed by clicking the relevant title displayed in violet text.

[1] Foote, E. ART. XXXI.–Circumstances Affecting the Heat of the Sun's Rays. *Am. J. Sci. Arts* **1856**, *22*, 382–383.

[2] Arrhenius, S. XXXI. On the influence of carbonic acid in the air upon the temperature of the ground. *London, Edinburgh, Dublin Philos. Mag. J. Sci.* **1896**, *41*, 237–276.

[3] Callendar, G. S. The artificial production of carbon dioxide and its influence on temperature. *Q. J. R. Meteorol. Soc.* **1938**, *64*, 223–240.

[4] Callendar, G. S. Can Carbon Dioxide Influence Climate? *Weather* **1949**, *4*, 310–314.

[5] IPCC In *Climate change 2001: impacts, adaptation, and vulnerability*; McCarthy, J. J., Canziani, O. F., Leary, N. A., Dokken, D. J., White, K. S., Eds.; Cambridge University Press: Cambridge, United Kingdom, 2001.

[6] Oreskes, N. The Scientific Consensus on Climate Change. *Science* **2004**, *306*, 1686–1686.

[7] International Energy Agency (IEA) World Energy Balances: Overview. 2021; https://www.iea.org/reports/world-energy-balances-overview, accessed 07-07-2022.

[8] Ritchie, H.; Roser, M.; Rosado, P. Energy Mix, Our World in Data. 2022; https://ourworldindata.org/energy-mix, accessed 13-07-2023.

[9] Our World in Data Global primary energy consumption by source. 2022; https://ourworldindata.org/grapher/global-energy-consumption-source, accessed 03-09-2023.

[10] United Nations Environment Programme (UNEP) Emissions Gap Report. 2022; https://www.unep.org/resources/emissions-gap-report-2022, accessed 13-07-2023.

[11] International Renewable Energy Agency (IRENA) Renewable Power Generation Costs in 2021. 2021; https://www.irena.org/publications/2022/Jul/Renewable-Power-Generation-Costs-in-2021, accessed 14-07-2023.

[12] Thirugnanasambandam, M.; Iniyan, S.; Goic, R. A review of solar thermal technologies. *Renew. Sustain. Energy Rev.* **2010**, *14*, 312–322.

[13] Bello, S.; Urwick, A.; Bastianini, F.; Nedoma, A. J.; Dunbar, A. An introduction to perovskites for solar cells and their characterisation. *Energy Reports* **2022**, *8*, 89–106.

[14] Ballif, C.; Haug, F.-J.; Boccard, M.; Verlinden, P. J.; Hahn, G. Status and perspectives of crystalline silicon photovoltaics in research and industry. *Nat. Rev. Mater.* **2022**, *7*, 597–616.

[15] Peng, J.; Lu, L.; Yang, H. Review on life cycle assessment of energy payback and greenhouse gas emission of solar photovoltaic systems. *Renew. Sustain. Energy Rev.* **2013**, *19*, 255–274.

[16] Jean, J.; Brown, P. R.; Jaffe, R. L.; Buonassisi, T.; Bulović, V. Pathways for solar photovoltaics. *Energy Environ. Sci.* **2015**, *8*, 1200–1219.

[17] Green, M. A. Third generation photovoltaics: Ultra-high conversion efficiency at low cost. *Prog. Photovolt.: Res. Appl.* **2001**, *9*, 123–135.

[18] Lewis, N. S. Toward Cost-Effective Solar Energy Use. *Science* **2007**, *315*, 798–801.

[19] Hestand, N. J.; Spano, F. C. Expanded Theory of H- and J-Molecular Aggregates: The Effects of Vibronic Coupling and Intermolecular Charge Transfer. *Chem. Rev.* **2018**, *118*, 7069–7163.

[20] Baldo, M. A.; O'Brien, D. F.; You, Y.; Shoustikov, A.; Sibley, S.; Thompson, M. E.; Forrest, S. R. Highly efficient phosphorescent emission from organic electroluminescent devices. *Nature* **1998**, *395*, 151–154.

[21] Friend, R, H.; Gymer, R, W.; Holmes, A, B.; Burrouges, J, H.; Marks, R, N.; Taliani, C.; Bradley, D, D, C.; Dos Santos, D, A.; Brédas, J, L.; Lögdlund, M.; Salaneck, W, R. Electroluminescence in conjugated polymers. *Nat. Chem.* **1999**, *397*, 121–128.

[22] Zhu, L. et al. Single-junction organic solar cells with over 19% efficiency enabled by a refined double-fibril network morphology. *Nat. Mater.* **2022**, *21*, 656–663.

[23] Green, M. A.; Ho-Baillie, A.; Snaith, H. J. The emergence of perovskite solar cells. *Nat. Photonics* **2014**, *8*, 506–514.

[24] Rose, G. *De novis quibusdam fossilibus quae in Montibus Uraliis inveniuntur*; AG Schade: Berlin, Germany, 1839; pp 3–5.

[25] Chakhmouradian, A. R.; Woodward, P. M. Celebrating 175 years of perovskite research: a tribute to Roger H. Mitchell. *Phys. Chem. Miner.* **2014**, *41*, 387–391.

[26] Goldschmidt, V. M. Die Gesetze der Krystallochemie. *Naturwissenschaften* **1926**, *14*, 477–485.

[27] Tschauner, O.; Huang, S.; Yang, S.; Humayun, M.; Liu, W.; Gilbert Corder, S. N.; Bechtel, H. A.; Tischler, J.; Rossman, G. R. Discovery of davemaoite, $CaSiO_3$-perovskite, as a mineral from the lower mantle. *Science* **2021**, *374*, 891–894.

[28] Attfield, J. P.; Lightfoot, P.; Morris, R. E. Perovskites. *Dalt. Trans.* **2015**, *44*, 10541–10542.

[29] Talley, K. R.; Perkins, C. L.; Diercks, D. R.; Brennecka, G. L.; Zakutayev, A. Synthesis of $LaWN_3$ nitride perovskite with polar symmetry. *Science* **2021**, *374*, 1488–1491.

[30] Ye, H.-Y.; Tang, Y.-Y.; Li, P.-F.; Liao, W.-Q.; Gao, J.-X.; Hua, X.-N.; Cai, H.; Shi, P.-P.; You, Y.-M.; Xiong, R.-G. Metal-free three-dimensional perovskite ferroelectrics. *Science* **2018**, *361*, 151–155.

[31] Wells, H. L. Über die Cäsium- und Kalium-Bleihalogenide. *Zeitschrift für Anorg. Chemie* **1893**, *3*, 195–210.

[32] Møller, C. K. Crystal Structure and Photoconductivity of Cæsium Plumbohalides. *Nature* **1958**, *182*, 1436–1436.

[33] Mitzi, D. B.; Feild, C. A.; Harrison, W. T. A.; Guloy, A. M. Conducting tin halides with a layered organic-based perovskite structure. *Nature* **1994**, *369*, 467–469.

[34] Mitzi, D.; Feild, C.; Schlesinger, Z.; Laibowitz, R. Transport, Optical, and Magnetic Properties of the Conducting Halide Perovskite $CH_3NH_3SnI_3$. *J. Solid State Chem.* **1995**, *114*, 159–163.

[35] Kojima, A.; Teshima, K.; Shirai, Y.; Miyasaka, T. Organometal Halide Perovskites as Visible-Light Sensitizers for Photovoltaic Cells. *J. Am. Chem. Soc.* **2009**, *131*, 6050–6051.

[36] O'Regan, B.; Grätzel, M. A low-cost, high-efficiency solar cell based on dye-sensitized colloidal TiO_2 films. *Nature* **1991**, *353*, 737–740.

[37] Im, J.-H.; Lee, C.-R.; Lee, J.-W.; Park, S.-W.; Park, N.-G. 6.5% efficient perovskite quantum-dot-sensitized solar cell. *Nanoscale* **2011**, *3*, 4088.

[38] Lee, M. M.; Teuscher, J.; Miyasaka, T.; Murakami, T. N.; Snaith, H. J. Efficient Hybrid Solar Cells Based on Meso-Superstructured Organometal Halide Perovskites. *Science* **2012**, *338*, 643–647.

[39] Kim, H.-S.; Lee, C.-R.; Im, J.-H.; Lee, K.-B.; Moehl, T.; Marchioro, A.; Moon, S.-J.; Humphry-Baker, R.; Yum, J.-H.; Moser, J. E.; Grätzel, M.; Park, N.-G. Lead Iodide Perovskite Sensitized All-Solid-State Submicron Thin Film Mesoscopic Solar Cell with Efficiency Exceeding 9%. *Sci. Rep.* **2012**, *2*, 591.

[40] Umari, P.; Mosconi, E.; De Angelis, F. Relativistic GW calculations on $CH_3NH_3PbI_3$ and $CH_3NH_3SnI_3$ Perovskites for Solar Cell Applications. *Sci. Rep.* **2014**, *4*, 4467.

[41] Even, J.; Pedesseau, L.; Jancu, J.-M.; Katan, C. Importance of Spin-Orbit Coupling in Hybrid Organic/Inorganic Perovskites for Photovoltaic Applications. *J. Phys. Chem. Lett.* **2013**, *4*, 2999–3005.

[42] Tanaka, K.; Takahashi, T.; Ban, T.; Kondo, T.; Uchida, K.; Miura, N. Comparative study on the excitons in lead-halide-based perovskite-type crystals $CH_3NH_3PbBr_3$ CH3NH_3PbI_3. *Solid State Commun.* **2003**, *127*, 619–623.

[43] Yang, Z.; Surrente, A.; Galkowski, K.; Miyata, A.; Portugall, O.; Sutton, R. J.; Haghighirad, A. A.; Snaith, H. J.; Maude, D. K.; Plochocka, P.; Nicholas, R. J. Impact of the Halide Cage on the Electronic Properties of Fully Inorganic Cesium Lead Halide Perovskites. *ACS Energy Lett.* **2017**, *2*, 1621–1627.

[44] Wehrenfennig, C.; Eperon, G. E.; Johnston, M. B.; Snaith, H. J.; Herz, L. M. High Charge Carrier Mobilities and Lifetimes in Organolead Trihalide Perovskites. *Adv. Mater.* **2014**, *26*, 1584–1589.

[45] Brenner, T. M.; Egger, D. A.; Rappe, A. M.; Kronik, L.; Hodes, G.; Cahen, D. Are Mobilities in Hybrid Organic-Inorganic Halide Perovskites Actually "High"? *J. Phys. Chem. Lett.* **2015**, *6*, 4754–4757.

[46] Stranks, S. D.; Eperon, G. E.; Grancini, G.; Menelaou, C.; Alcocer, M. J. P.; Leijtens, T.; Herz, L. M.; Petrozza, A.; Snaith, H. J. Electron-Hole Diffusion Lengths Exceeding 1 Micrometer in an Organometal Trihalide Perovskite Absorber. *Science* **2013**, *342*, 341–344.

[47] Xing, G.; Mathews, N.; Sun, S.; Lim, S. S.; Lam, Y. M.; Grätzel, M.; Mhaisalkar, S.; Sum, T. C. Long-Range Balanced Electron- and Hole-Transport Lengths in Organic-Inorganic $CH_3NH_3PbI_3$. *Science* **2013**, *342*, 344–347.

[48] National Renewable Energy Laboratory Best Research-Cell Efficiency Chart. accessed 03-09-2023.

[49] Giustino, F.; Snaith, H. J. Toward Lead-Free Perovskite Solar Cells. *ACS Energy Lett.* **2016**, *1*, 1233–1240.

[50] Babayigit, A.; Ethirajan, A.; Muller, M.; Conings, B. Toxicity of organometal halide perovskite solar cells. *Nat. Mater.* **2016**, *15*, 247–251.

[51] Zhang, H.; Lee, J.-w.; Nasti, G.; Handy, R.; Abate, A.; Grätzel, M.; Park, N.-G. Lead immobilization for environmentally sustainable perovskite solar cells. *Nature* **2023**, *617*, 687–695.

[52] Kovalenko, M. V.; Protesescu, L.; Bodnarchuk, M. I. Properties and potential optoelectronic applications of lead halide perovskite nanocrystals. *Science* **2017**, *358*, 745–750.

[53] Hutter, E. M.; Sangster, R.; Testerink, C.; Ehrler, B.; Gommers, C. M. Metal halide perovskite toxicity effects on Arabidopsis thaliana plants are caused by iodide ions. *iScience* **2022**, *25*, 103583.

[54] Ganose, A. M.; Savory, C. N.; Scanlon, D. O. Beyond methylammonium lead iodide: prospects for the emergent field of ns^2 containing solar absorbers. *Chem. Commun.* **2017**, *53*, 20–44.

[55] Lanzetta, L.; Webb, T.; Zibouche, N.; Liang, X.; Ding, D.; Min, G.; Westbrook, R. J. E.; Gaggio, B.; Macdonald, T. J.; Islam, M. S.; Haque, S. A. Degradation mechanism of hybrid tin-based perovskite solar cells and the critical role of tin (IV) iodide. *Nat. Commun.* **2021**, *12*, 2853.

[56] Bartesaghi, D.; Slavney, A. H.; Gélvez-Rueda, M. C.; Connor, B. A.; Grozema, F. C.; Karunadasa, H. I.; Savenije, T. J. Charge Carrier Dynamics in $Cs_2AgBiBr_6$ Double Perovskite. *J. Phys. Chem. C* **2018**, *122*, 4809–4816.

[57] Ke, W.; Kanatzidis, M. G. Prospects for low-toxicity lead-free perovskite solar cells. *Nat. Commun.* **2019**, *10*, 965.

[58] Ekimov, A. I.; Onushchenko, A. A. Quantum size effect in the optical spectra of semiconductor microcrystals. *Sov. Phys. Semicond.* **1982**, *16*, 775–778.

[59] Efros, A. L.; Efros, A. L. Interband absorption of light in a semiconductor sphere. *Sov. Phys. Semicond.* **1982**, *16*, 772–775.

[60] Rossetti, R.; Nakahara, S.; Brus, L. E. Quantum size effects in the redox potentials, resonance Raman spectra, and electronic spectra of CdS crystallites in aqueous solution. *J. Chem. Phys.* **1983**, *79*, 1086–1088.

[61] Fojtik, A.; Weller, H.; Koch, U.; Henglein, A. Photo-Physics of Extremely Small CdS Particles: Q-State CdS and Magic Agglomeration Numbers. *Ber. Bunsenges. Phys. Chem.* **1984**, *88*, 969–997.

[62] Steigerwald, M. L.; Alivisatos, A. P.; Gibson, J. M.; Harris, T. D.; Kortan, R.; Muller, A. J.; Thayer, A. M.; Duncan, T. M.; Douglass, D. C.; Brus, L. E. Surface Derivatization and Isolation of Semiconductor Cluster Molecules. *J. Am. Chem. Soc.* **1988**, *110*, 3046–3050.

[63] Reed, M.; Randall, J.; Aggarwal, R.; Matyi, R.; Moore, T.; Wetsel, A. Observation of discrete electronic states in a zero-dimensional semiconductor nanostructure. *Phys. Rev. Lett.* **1988**, *60*, 535–537.

[64] Murray, C. B.; Norris, D. J.; Bawendi, M. G. Synthesis and Characterization of Nearly Monodisperse CdE (E = S, Se, Te) Semiconductor Nanocrystallites. *J. Am. Chem. Soc.* **1993**, *115*, 8706–8715.

[65] Pietryga, J. M.; Park, Y.-S.; Lim, J.; Fidler, A. F.; Bae, W. K.; Brovelli, S.; Klimov, V. I. Spectroscopic and Device Aspects of Nanocrystal Quantum Dots. *Chem. Rev.* **2016**, *116*, 10513–10622.

[66] Hines, M. A.; Guyot-Sionnest, P. Synthesis and Characterization of Strongly Luminescing ZnS-Capped CdSe Nanocrystals. *J. Phys. Chem.* **1996**, *100*, 468–471.

[67] Danek, M.; Jensen, K. F.; Murray, C. B.; Bawendi, M. G. Synthesis of Luminescent Thin-Film CdSe/ZnSe Quantum Dot Composites Using CdSe Quantum Dots Passivated with an Overlayer of ZnSe. *Chem. Mater.* **1996**, *8*, 173–180.

[68] Ghosh Chaudhuri, R.; Paria, S. Core/Shell Nanoparticles: Classes, Properties, Synthesis Mechanisms, Characterization, and Applications. *Chem. Rev.* **2012**, *112*, 2373–2433.

[69] Shirasaki, Y.; Supran, G. J.; Bawendi, M. G.; Bulović, V. Emergence of colloidal quantum-dot light-emitting technologies. *Nat. Photonics* **2013**, *7*, 13–23.

[70] Zheng, Y.; Zheng, L.; Zhan, Y.; Lin, X.; Zheng, Q.; Wei, K. Ag/ZnO Heterostructure Nanocrystals: Synthesis, Characterization, and Photocatalysis. *Inorg. Chem.* **2007**, *46*, 6980–6986.

[71] Alivisatos, P. The use of nanocrystals in biological detection. *Nat. Biotechnol.* **2004**, *22*, 47–52.

[72] Medintz, I. L.; Uyeda, H. T.; Goldman, E. R.; Mattoussi, H. Quantum dot bioconjugates for imaging, labelling and sensing. *Nat. Mater.* **2005**, *4*, 435–446.

[73] Soetaert, F.; Korangath, P.; Serantes, D.; Fiering, S.; Ivkov, R. Cancer therapy with iron oxide nanoparticles: Agents of thermal and immune therapies. *Adv. Drug Deliv. Rev.* **2020**, *163-164*, 65–83.

[74] Gonzalez-Carrero, S.; Galian, R. E.; Pérez-Prieto, J. Maximizing the emissive properties of $CH_3NH_3PbBr_3$ perovskite nanoparticles. *J. Mater. Chem. A* **2015**, *3*, 9187–9193.

[75] Zhang, F.; Zhong, H.; Chen, C.; Wu, X.-g.; Hu, X.; Huang, H.; Han, J.; Zou, B.; Dong, Y. Brightly Luminescent and Color-Tunable Colloidal $CH_3NH_3PbX_3$ (X = Br, I, Cl) Quantum Dots: Potential Alternatives for Display Technology. *ACS Nano* **2015**, *9*, 4533–4542.

[76] Protesescu, L.; Yakunin, S.; Bodnarchuk, M. I.; Krieg, F.; Caputo, R.; Hendon, C. H.; Yang, R. X.; Walsh, A.; Kovalenko, M. V. Nanocrystals of Cesium Lead Halide Perovskites ($CsPbX_3$, X = Cl, Br, and I): Novel Optoelectronic Materials Showing Bright Emission with Wide Color Gamut. *Nano Lett.* **2015**, *15*, 3692–3696.

[77] Nedelcu, G.; Protesescu, L.; Yakunin, S.; Bodnarchuk, M. I.; Grotevent, M. J.; Kovalenko, M. V. Fast Anion-Exchange in Highly Luminescent Nanocrystals of Cesium Lead Halide Perovskites ($CsPbX_3$, X = Cl, Br, I). *Nano Lett.* **2015**, *15*, 5635–5640.

[78] Akkerman, Q. A.; D'Innocenzo, V.; Accornero, S.; Scarpellini, A.; Petrozza, A.; Prato, M.;

Manna, L. Tuning the Optical Properties of Cesium Lead Halide Perovskite Nanocrystals by Anion Exchange Reactions. *J. Am. Chem. Soc.* **2015**, *137*, 10276–10281.

[79] Yakunin, S.; Protesescu, L.; Krieg, F.; Bodnarchuk, M. I.; Nedelcu, G.; Humer, M.; De Luca, G.; Fiebig, M.; Heiss, W.; Kovalenko, M. V. Low-threshold amplified spontaneous emission and lasing from colloidal nanocrystals of caesium lead halide perovskites. *Nat. Commun.* **2015**, *6*, 8056.

[80] Xu, Y.; Chen, Q.; Zhang, C.; Wang, R.; Wu, H.; Zhang, X.; Xing, G.; Yu, W. W.; Wang, X.; Zhang, Y.; Xiao, M. Two-Photon-Pumped Perovskite Semiconductor Nanocrystal Lasers. *J. Am. Chem. Soc.* **2016**, *138*, 3761–3768.

[81] Swarnkar, A.; Marshall, A. R.; Sanehira, E. M.; Chernomordik, B. D.; Moore, D. T.; Christians, J. A.; Chakrabarti, T.; Luther, J. M. Quantum dot-induced phase stabilization of α-$CsPbI_3$ perovskite for high-efficiency photovoltaics. *Science* **2016**, *354*, 92–95.

[82] Akkerman, Q. A.; Rainò, G.; Kovalenko, M. V.; Manna, L. Genesis, challenges and opportunities for colloidal lead halide perovskite nanocrystals. *Nat. Mater.* **2018**, *17*, 394–405.

[83] De Roo, J.; Ibáñez, M.; Geiregat, P.; Nedelcu, G.; Walravens, W.; Maes, J.; Martins, J. C.; Van Driessche, I.; Kovalenko, M. V.; Hens, Z. Highly Dynamic Ligand Binding and Light Absorption Coefficient of Cesium Lead Bromide Perovskite Nanocrystals. *ACS Nano* **2016**, *10*, 2071–2081.

[84] Huang, Y.; Yin, W.-J.; He, Y. Intrinsic Point Defects in Inorganic Cesium Lead Iodide Perovskite $CsPbI_3$. *J. Phys. Chem. C* **2018**, *122*, 1345–1350.

[85] Protesescu, L.; Yakunin, S.; Kumar, S.; Bär, J.; Bertolotti, F.; Masciocchi, N.; Guagliardi, A.; Grotevent, M.; Shorubalko, I.; Bodnarchuk, M. I.; Shih, C.-J.; Kovalenko, M. V. Dismantling the "Red Wall" of Colloidal Perovskites: Highly Luminescent Formamidinium and Formamidinium-Cesium Lead Iodide Nanocrystals. *ACS Nano* **2017**, *11*, 3119–3134.

[86] Li, X.; Wu, Y.; Zhang, S.; Cai, B.; Gu, Y.; Song, J.; Zeng, H. $CsPbX_3$ Quantum Dots for Lighting and Displays: Room-Temperature Synthesis, Photoluminescence Superiorities, Underlying Origins and White Light-Emitting Diodes. *Adv. Funct. Mater.* **2016**, *26*, 2435–2445.

[87] Tan, Y.; Zou, Y.; Wu, L.; Huang, Q.; Yang, D.; Chen, M.; Ban, M.; Wu, C.; Wu, T.; Bai, S.; Song, T.; Zhang, Q.; Sun, B. Highly Luminescent and Stable Perovskite Nanocrystals with Octylphosphonic Acid as a Ligand for Efficient Light-Emitting Diodes. *ACS Appl. Mater. Interfaces* **2018**, *10*, 3784–3792.

[88] Seth, S.; Ahmed, T.; De, A.; Samanta, A. Tackling the Defects, Stability, and Photoluminescence of $CsPbX_3$ Perovskite Nanocrystals. *ACS Energy Lett.* **2019**, *4*, 1610–1618.

[89] Shynkarenko, Y.; Bodnarchuk, M. I.; Bernasconi, C.; Berezovska, Y.; Verteletskyi, V.; Ochsenbein, S. T.; Kovalenko, M. V. Direct Synthesis of Quaternary Alkylammonium-Capped Perovskite Nanocrystals for Efficient Blue and Green Light-Emitting Diodes. *ACS Energy Lett.* **2019**, *4*, 2703–2711.

[90] Zhang, B.; Goldoni, L.; Zito, J.; Dang, Z.; Almeida, G.; Zaccaria, F.; de Wit, J.; Infante, I.; De Trizio, L.; Manna, L. Alkyl Phosphonic Acids Deliver $CsPbBr_3$ Nanocrystals with High Photoluminescence Quantum Yield and Truncated Octahedron Shape. *Chem. Mater.* **2019**, *31*, 9140–9147.

[91] Koscher, B. A.; Swabeck, J. K.; Bronstein, N. D.; Alivisatos, A. P. Essentially Trap-Free $CsPbBr_3$ Colloidal Nanocrystals by Postsynthetic Thiocyanate Surface Treatment. *J. Am. Chem. Soc.* **2017**, *139*, 6566–6569.

[92] Liu, F.; Zhang, Y.; Ding, C.; Kobayashi, S.; Izuishi, T.; Nakazawa, N.; Toyoda, T.; Ohta, T.; Hayase, S.; Minemoto, T.; Yoshino, K.; Dai, S.; Shen, Q. Highly Luminescent Phase-Stable $CsPbI_3$ Perovskite Quantum Dots Achieving Near 100% Absolute Photoluminescence Quantum Yield. *ACS Nano* **2017**, *11*, 10373–10383.

[93] Krieg, F.; Ochsenbein, S. T.; Yakunin, S.; ten Brinck, S.; Aellen, P.; Süess, A.; Clerc, B.; Guggisberg, D.; Nazarenko, O.; Shynkarenko, Y.; Kumar, S.; Shih, C.-J.; Infante, I.; Ko-

valenko, M. V. Colloidal $CsPbX_3$ (X = Cl, Br, I) Nanocrystals 2.0: Zwitterionic Capping Ligands for Improved Durability and Stability. *ACS Energy Lett.* **2018**, *3*, 641–646.

[94] Wang, S.; Du, L.; Jin, Z.; Xin, Y.; Mattoussi, H. Enhanced Stabilization and Easy Phase Transfer of $CsPbBr_3$ Perovskite Quantum Dots Promoted by High-Affinity Polyzwitterionic Ligands. *J. Am. Chem. Soc.* **2020**, *142*, 12669–12680.

[95] Peng, X.; Manna, L.; Yang, W.; Wickham, J.; Scher, E.; Kadavanich, A.; Alivisatos, A. P. Shape control of CdSe nanocrystals. *Nature* **2000**, *404*, 59–61.

[96] Esaki, L.; Tsu, R. Superlattice and Negative Differential Conductivity in Semiconductors. *IBM J. Res. Dev.* **1970**, *14*, 61–65.

[97] Schmidt, L. C.; Pertegás, A.; González-Carrero, S.; Malinkiewicz, O.; Agouram, S.; Mínguez Espallargas, G.; Bolink, H. J.; Galian, R. E.; Pérez-Prieto, J. Nontemplate Synthesis of $CH_3NH_3PbBr_3$ Perovskite Nanoparticles. *J. Am. Chem. Soc.* **2014**, *136*, 850–853.

[98] Tyagi, P.; Arveson, S. M.; Tisdale, W. A. Colloidal Organohalide Perovskite Nanoplatelets Exhibiting Quantum Confinement. *J. Phys. Chem. Lett.* **2015**, *6*, 1911–1916.

[99] Stoumpos, C. C.; Cao, D. H.; Clark, D. J.; Young, J.; Rondinelli, J. M.; Jang, J. I.; Hupp, J. T.; Kanatzidis, M. G. Ruddlesden-Popper Hybrid Lead Iodide Perovskite 2D Homologous Semiconductors. *Chem. Mater.* **2016**, *28*, 2852–2867.

[100] Righetto, M.; Giovanni, D.; Lim, S. S.; Sum, T. C. The photophysics of Ruddlesden-Popper perovskites: A tale of energy, charges, and spins. *Appl. Phys. Rev.* **2021**, *8*.

[101] Liang, C. et al. Two-dimensional Ruddlesden-Popper layered perovskite solar cells based on phase-pure thin films. *Nat. Energy* **2021**, *6*, 38–45.

[102] Weidman, M. C.; Seitz, M.; Stranks, S. D.; Tisdale, W. A. Highly Tunable Colloidal Perovskite Nanoplatelets through Variable Cation, Metal, and Halide Composition. *ACS Nano* **2016**, *10*, 7830–7839.

[103] Hong, X.; Ishihara, T.; Nurmikko, A. V. Dielectric confinement effect on excitons in PbI_4-based layered semiconductors. *Phys. Rev. B* **1992**, *45*, 6961–6964.

[104] Smith, I. C.; Hoke, E. T.; Solis-Ibarra, D.; McGehee, M. D.; Karunadasa, H. I. A Layered Hybrid Perovskite Solar-Cell Absorber with Enhanced Moisture Stability. *Angew. Chem. Int. Ed.* **2014**, *53*, 11232–11235.

[105] Milot, R. L.; Sutton, R. J.; Eperon, G. E.; Haghighirad, A. A.; Martinez Hardigree, J.; Miranda, L.; Snaith, H. J.; Johnston, M. B.; Herz, L. M. Charge-Carrier Dynamics in 2D Hybrid Metal-Halide Perovskites. *Nano Lett.* **2016**, *16*, 7001–7007.

[106] Grancini, G.; Roldán-Carmona, C.; Zimmermann, I.; Mosconi, E.; Lee, X.; Martineau, D.; Narbey, S.; Oswald, F.; De Angelis, F.; Graetzel, M.; Nazeeruddin, M. K. One-Year stable perovskite solar cells by 2D/3D interface engineering. *Nat. Commun.* **2017**, *8*, 15684.

[107] Yu, S.; Yan, Y.; Chen, Y.; Chábera, P.; Zheng, K.; Liang, Z. Enabling room-temperature processed highly efficient and stable 2D Ruddlesden-Popper perovskite solar cells with eliminated hysteresis by synergistic exploitation of additives and solvents. *J. Mater. Chem. A* **2019**, *7*, 2015–2021.

[108] Albaladejo-Siguan, M.; Becker-Koch, D.; Baird, E. C.; Hofstetter, Y. J.; Carwithen, B. P.; Kirch, A.; Reineke, S.; Bakulin, A. A.; Paulus, F.; Vaynzof, Y. Interdot Lead Halide Excess Management in PbS Quantum Dot Solar Cells. *Adv. Energy Mater.* **2022**, *12*, 1–10.

[109] Norrish, R. G. W.; Porter, G. Chemical Reactions Produced by Very High Light Intensities. *Nature* **1949**, *164*, 658.

[110] Porter, G. Flash photolysis and spectroscopy. A new method for the study of free radical reactions. *Proc. R. Soc. London. Ser. A. Math. Phys. Sci.* **1950**, *200*, 284–300.

[111] Scherer, N. F.; Knee, J. L.; Smith, D. D.; Zewail, A. H. Femtosecond Photofragment Spectroscopy: The Reaction ICN → CN + I. *J. Phys. Chem.* **1985**, *89*, 5141–5143.

[112] Rosker, M. J.; Dantus, M.; Zewail, A. H. Femtosecond Clocking of the Chemical Bond. *Science* **1988**, *241*, 1200–1202.

[113] Zewail, A. H. Laser Femtochemistry. *Science* **1988**, *242*, 1645–1653.

[114] Maiuri, M.; Garavelli, M.; Cerullo, G. Ultrafast Spectroscopy: State of the Art and Open Challenges. *J. Am. Chem. Soc.* **2020**, *142*, 3–15.

[115] Atkins, P.; de Paula, J. *Atkins' Physical Chemistry*, 10th ed.; Oxford University Press: Oxford, United Kingdom, 2014.

[116] Eperon, G. E.; Stranks, S. D.; Menelaou, C.; Johnston, M. B.; Herz, L. M.; Snaith, H. J. Formamidinium lead trihalide: a broadly tunable perovskite for efficient planar heterojunction solar cells. *Energy Environ. Sci.* **2014**, *7*, 982.

[117] Albero, J.; Asiri, A. M.; García, H. Influence of the composition of hybrid perovskites on their performance in solar cells. *J. Mater. Chem. A* **2016**, *4*, 4353–4364.

[118] Prasanna, R.; Gold-Parker, A.; Leijtens, T.; Conings, B.; Babayigit, A.; Boyen, H.-G.; Toney, M. F.; McGehee, M. D. Band Gap Tuning via Lattice Contraction and Octahedral Tilting in Perovskite Materials for Photovoltaics. *J. Am. Chem. Soc.* **2017**, *139*, 11117–11124.

[119] Tanaka, K.; Takahashi, T.; Ban, T.; Kondo, T.; Uchida, K.; Miura, N. Comparative study on the excitons in lead-halide-based perovskite-type crystals $CH_3NH_3PbBr_3$ $CH_3NH_3PbI_3$. *Solid State Commun.* **2003**, *127*, 619–623.

[120] Noh, J. H.; Im, S. H.; Heo, J. H.; Mandal, T. N.; Seok, S. I. Chemical Management for Colorful, Efficient, and Stable Inorganic-Organic Hybrid Nanostructured Solar Cells. *Nano Lett.* **2013**, *13*, 1764–1769.

[121] Tao, S. X.; Cao, X.; Bobbert, P. A. Accurate and efficient band gap predictions of metal halide perovskites using the DFT-1/2 method: GW accuracy with DFT expense. *Sci. Rep.* **2017**, *7*, 14386.

[122] Li, Y.; Lu, Y.; Huo, X.; Wei, D.; Meng, J.; Dong, J.; Qiao, B.; Zhao, S.; Xu, Z.; Song, D. Bandgap tuning strategy by cations and halide ions of lead halide perovskites learned from machine learning. *RSC Adv.* **2021**, *11*, 15688–15694.

[123] Euvrard, J.; Yan, Y.; Mitzi, D. B. Electrical doping in halide perovskites. *Nat. Rev. Mater.* **2021**, *6*, 531–549.

[124] Nelson, J. *The Physics of Solar Cells*; Imperial College Press: London, United Kingdom, 2003.

[125] Stoumpos, C. C.; Malliakas, C. D.; Kanatzidis, M. G. Semiconducting Tin and Lead Iodide Perovskites with Organic Cations: Phase Transitions, High Mobilities, and Near-Infrared Photoluminescent Properties. *Inorg. Chem.* **2013**, *52*, 9019–9038.

[126] Stoumpos, C. C.; Malliakas, C. D.; Peters, J. A.; Liu, Z.; Sebastian, M.; Im, J.; Chasapis, T. C.; Wibowo, A. C.; Chung, D. Y.; Freeman, A. J.; Wessels, B. W.; Kanatzidis, M. G. Crystal Growth of the Perovskite Semiconductor $CsPbBr_3$: A New Material for High-Energy Radiation Detection. *Cryst. Growth Des.* **2013**, *13*, 2722–2727.

[127] Hutter, E. M.; Gélvez-Rueda, M. C.; Osherov, A.; Bulović, V.; Grozema, F. C.; Stranks, S. D.; Savenije, T. J. Direct-indirect character of the bandgap in methylammonium lead iodide perovskite. *Nat. Mater.* **2017**, *16*, 115–120.

[128] Haynes, J. R.; Westphal, W. C. Radiation Resulting from Recombination of Holes and Electrons in Silicon. *Phys. Rev.* **1956**, *101*, 1676–1678.

[129] Cullis, A. G.; Canham, L. T. Visible light emission due to quantum size effects in highly porous crystalline silicon. *Nature* **1991**, *353*, 335–338.

[130] Priolo, F.; Gregorkiewicz, T.; Galli, M.; Krauss, T. F. Silicon nanostructures for photonics and photovoltaics. *Nat. Nanotechnol.* **2014**, *9*, 19–32.

[131] Efros, A. L.; Brus, L. E. Nanocrystal Quantum Dots: From Discovery to Modern Development. *ACS Nano* **2021**, *15*, 6192–6210.

[132] Saha, M. N. LIII. Ionization in the solar chromosphere. *London, Edinburgh, Dublin Philos. Mag. J. Sci.* **1920**, *40*, 472–488.

[133] Saha, M. N. On a physical theory of stellar spectra. *Proc. R. Soc. London. Ser. A* **1921**, *99*, 135–153.

[134] Landau, L. On the Motion of Electrons in a Crystal Lattice. *Phys. Z. Sowjetunion* **1933**, *3*, 664–665.

[135] Feynman, R. P. Slow Electrons in a Polar Crystal. *Phys. Rev.* **1955**, *97*, 660–665.

[136] DeQuilettes, D. W.; Frohna, K.; Emin, D.; Kirchartz, T.; Bulovic, V.; Ginger, D. S.; Stranks, S. D. Charge-Carrier Recombination in Halide Perovskites. *Chem. Rev.* **2019**, *119*, 11007–11019.

[137] Miyata, K.; Atallah, T. L.; Zhu, X.-Y. Lead halide perovskites: Crystal-liquid duality, phonon glass electron crystals, and large polaron formation. *Sci. Adv.* **2017**, *3*, 1–11.

[138] Cinquanta, E.; Meggiolaro, D.; Motti, S. G.; Gandini, M.; Alcocer, M. J.; Akkerman, Q. A.; Vozzi, C.; Manna, L.; De Angelis, F.; Petrozza, A.; Stagira, S. Ultrafast THz Probe of Photoinduced Polarons in Lead-Halide Perovskites. *Phys. Rev. Lett.* **2019**, *122*, 166601.

[139] Guzelturk, B. et al. Visualization of dynamic polaronic strain fields in hybrid lead halide perovskites. *Nat. Mater.* **2021**, *20*, 618–623.

[140] Frost, J. M. Calculating polaron mobility in halide perovskites. *Phys. Rev. B* **2017**, *96*, 195202.

[141] Ghosh, D.; Welch, E.; Neukirch, A. J.; Zakhidov, A.; Tretiak, S. Polarons in Halide Perovskites: A Perspective. *J. Phys. Chem. Lett.* **2020**, *11*, 3271–3286.

[142] Richter, J. M.; Branchi, F.; Valduga de Almeida Camargo, F.; Zhao, B.; Friend, R. H.; Cerullo, G.; Deschler, F. Ultrafast carrier thermalization in lead iodide perovskite probed with two-dimensional electronic spectroscopy. *Nat. Commun.* **2017**, *8*, 376.

[143] Seitz, F. On the Theory of Electron Multiplication in Crystals. *Phys. Rev.* **1949**, *76*, 1376–1393.

[144] Fröhlich, H.; Seitz, F. Notes on the Theory of Dielectric Breakdown in Ionic Crystals. *Phys. Rev.* **1950**, *79*, 526–527.

[145] Fröhlich, H. Electrons in lattice fields. *Adv. Phys.* **1954**, *3*, 325–361.

[146] Rota, L.; Lugli, P.; Elsaesser, T.; Shah, J. Ultrafast thermalization of photoexcited carriers in polar semiconductors. *Phys. Rev. B* **1993**, *47*, 4226–4237.

[147] Shockley, W.; Queisser, H. J. Detailed balance limit of efficiency of p-n junction solar cells. *J. Appl. Phys.* **1961**, *32*, 510–519.

[148] Mariotti, S. et al. Interface engineering for high-performance, triple-halide perovskite-silicon tandem solar cells. *Science* **2023**, *381*, 63–69.

[149] Chin, X. Y. et al. Interface passivation for 31.25%-efficient perovskite/silicon tandem solar cells. *Science* **2023**, *381*, 59–63.

[150] Schulze, T. F.; Schmidt, T. W. Photochemical upconversion: present status and prospects for its application to solar energy conversion. *Energy Environ. Sci.* **2015**, *8*, 103–125.

[151] Ross, R. T.; Nozik, A. J. Efficiency of hot-carrier solar energy converters. *J. Appl. Phys.* **1982**, *53*, 3813–3818.

[152] Nozik, A. J. Spectroscopy and hot electron relaxation dynamics in semiconductor quantum wells and quantum dots. *Annu. Rev. Phys. Chem.* **2001**, *52*, 193–231.

[153] Nozik, A. J. Quantum dot solar cells. *Phys. E* **2002**, *14*, 115–120.

[154] Beard, M. C. Multiple Exciton Generation in Semiconductor Quantum Dots. *J. Phys. Chem. Lett.* **2011**, *2*, 1282–1288.

[155] Aerts, M.; Suchand Sandeep, C. S.; Gao, Y.; Savenije, T. J.; Schins, J. M.; Houtepen, A. J.; Kinge, S.; Siebbeles, L. D. A. Free Charges Produced by Carrier Multiplication in Strongly Coupled PbSe Quantum Dot Films. *Nano Lett.* **2011**, *11*, 4485–4489.

[156] Böhm, M. L.; Jellicoe, T. C.; Tabachnyk, M.; Davis, N. J. L. K.; Wisnivesky-Rocca-Rivarola, F.; Ducati, C.; Ehrler, B.; Bakulin, A. A.; Greenham, N. C. Lead Telluride Quantum Dot Solar Cells Displaying External Quantum Efficiencies Exceeding 120%. *Nano Lett.* **2015**, *15*, 7987–7993.

[157] Smith, M. B.; Michl, J. Singlet Fission. *Chem. Rev.* **2010**, *110*, 6891–6936.

[158] Baldacchino, A. J.; Collins, M. I.; Nielsen, M. P.; Schmidt, T. W.; McCamey, D. R.; Tayebjee, M. J. Y. Singlet fission photovoltaics: Progress and promising pathways. *Chem. Phys. Rev.* **2022**, *3*, 021304.

[159] König, D.; Casalenuovo, K.; Takeda, Y.; Conibeer, G.; Guillemoles, J.; Patterson, R.; Huang, L.; Green, M. Hot carrier solar cells: Principles, materials and design. *Phys. E Low-dimensional Syst. Nanostructures* **2010**, *42*, 2862–2866.

[160] Kahmann, S.; Loi, M. A. Hot carrier solar cells and the potential of perovskites for breaking the Shockley-Queisser limit. *J. Mater. Chem. C* **2019**, *7*, 2471–2486.

[161] Takeda, Y.; Motohiro, T.; König, D.; Aliberti, P.; Feng, Y.; Shrestha, S.; Conibeer, G. Practical Factors Lowering Conversion Efficiency of Hot Carrier Solar Cells. *Appl. Phys. Express* **2010**, *3*, 104301.

[162] König, D.; Takeda, Y.; Puthen-Veettil, B.; Conibeer, G. Lattice-Matched Hot Carrier Solar Cell with Energy Selectivity Integrated into Hot Carrier Absorber. *Jpn. J. Appl. Phys.* **2012**, *51*, 10ND02.

[163] Osman, M. A.; Ferry, D. K. Monte Carlo investigation of the electron-hole-interaction effects on the ultrafast relaxation of hot photoexcited carriers in GaAs. *Phys. Rev. B* **1987**, *36*, 6018–6032.

[164] Shah, J.; Leite, R. C. C. Radiative Recombination from Photoexcited Hot Carriers in GaAs. *Phys. Rev. Lett.* **1969**, *22*, 1304–1307.

[165] Ippen, E.; Shank, C.; Dienes, A. Passive mode locking of the cw dye laser. *Appl. Phys. Lett.* **1972**, *21*, 348–350.

[166] Shank, C.; Auston, D.; Ippen, E.; Teschke, O. Picosecond time resolved reflectivity of direct gap semiconductors. *Solid State Commun.* **1978**, *26*, 567–570.

[167] von der Linde, D.; Lambrich, R. Direct Measurement of Hot-Electron Relaxation by Picosecond Spectroscopy. *Phys. Rev. Lett.* **1979**, *42*, 1090–1093.

[168] Leheny, R.; Shah, J.; Fork, R.; Shank, C.; Migus, A. Dynamics of hot carrier cooling in photo-excited GaAs. *Solid State Commun.* **1979**, *31*, 809–813.

[169] Shank, C.; Fork, R.; Yen, R.; Shah, J.; Greene, B.; Gossard, A.; Weisbuch, C. Picosecond dynamics of hot carrier relaxation in highly excited multi-quantum well structures. *Solid State Commun.* **1983**, *47*, 981–983.

[170] Pötz, W.; Kocevar, P. Electronic power transfer in pulsed laser excitation of polar semiconductors. *Phys. Rev. B* **1983**, *28*, 7040–7047.

[171] Xu, Z. Y.; Tang, C. L. Picosecond relaxation of hot carriers in highly photoexcited bulk GaAs and GaAs-AlGaAs multiple quantum wells. *Appl. Phys. Lett.* **1984**, *44*, 692–694.

[172] Ryan, J. F.; Taylor, R. A.; Turberfield, A. J.; Maciel, A.; Worlock, J. M.; Gossard, A. C.; Wiegmann, W. Time-Resolved Photoluminescence of Two-Dimensional Hot Carriers in GaAs-AlGaAs Heterostructures. *Phys. Rev. Lett.* **1984**, *53*, 1841–1844.

[173] Cai, W.; Marchetti, M. C.; Lax, M. Nonequilibrium electron-phonon scattering in semiconductor heterojunctions. *Phys. Rev. B* **1986**, *34*, 8573–8580.

[174] Cai, W.; Marchetti, M.; Lax, M. Nonequilibrium phonon effect on time-dependent relaxation of hot electrons in semiconductor heterojunctions. *Phys. Rev. B* **1987**, *35*, 1369–1372.

[175] Ge, W.; Xu, Z.; Li, Y.; Xu, Z.; Xu, J.; Zheng, B.; Zhuang, W. Hot carrier relaxation processes and nonequilibrium phonon effect in multiple quantum well structures. *J. Lumin.* **1990**, *46*, 137–145.

[176] Shah, J.; Pinczuk, A.; Gossard, A. C.; Wiegmann, W. Energy-Loss Rates for Hot Electrons and Holes in GaAs Quantum Wells. *Phys. Rev. Lett.* **1985**, *54*, 2045–2048.

[177] Shah, J.; Pinczuk, A.; Gossard, A.; Wiegmann, W.; Kash, K. Steady-state and picosecond investigation of hot carrier-phonon interactions in 2D systems. *Surf. Sci.* **1986**, *174*, 363–374.

[178] Collet, J.; Cornet, A.; Pugnet, M.; Amand, T. Cooling of high density electron-hole plasma. *Solid State Commun.* **1982**, *42*, 883–887.

[179] Shah, J. Photoexcited hot carriers: From cw to 6 fs in 20 years. *Solid. State. Electron.* **1989**, *32*, 1051–1056.

[180] Price, M. B.; Butkus, J.; Jellicoe, T. C.; Sadhanala, A.; Briane, A.; Halpert, J. E.; Broch, K.; Hodgkiss, J. M.; Friend, R. H.; Deschler, F. Hot-carrier cooling and photoinduced refractive index changes in organic-inorganic lead halide perovskites. *Nat. Commun.* **2015**, *6*, 8420.

[181] Yang, Y.; Ostrowski, D. P.; France, R. M.; Zhu, K.; van de Lagemaat, J.; Luther, J. M.; Beard, M. C. Observation of a hot-phonon bottleneck in lead-iodide perovskites. *Nat. Photonics* **2016**, *10*, 53–59.

[182] Zhu, H.; Miyata, K.; Fu, Y.; Wang, J.; Joshi, P. P.; Niesner, D.; Williams, K. W.; Jin, S.; Zhu, X. Y. Screening in crystalline liquids protects energetic carriers in hybrid perovskites. *Science* **2016**, *353*, 1409–1413.

[183] Klemens, P. G. Anharmonic decay of optical phonon in diamond. *Phys. Rev.* **1966**, *148*, 845–848.

[184] Fu, J.; Xu, Q.; Han, G.; Wu, B.; Huan, C. H. A.; Leek, M. L.; Sum, T. C. Hot carrier cooling mechanisms in halide perovskites. *Nat. Commun.* **2017**, *8*, 1300.

[185] Yang, J. et al. Acoustic-optical phonon up-conversion and hot-phonon bottleneck in lead-halide perovskites. *Nat. Commun.* **2017**, *8*, 14120.

[186] Sekiguchi, F.; Hirori, H.; Yumoto, G.; Shimazaki, A.; Nakamura, T.; Wakamiya, A.; Kanemitsu, Y. Enhancing the Hot-Phonon Bottleneck Effect in a Metal Halide Perovskite by Terahertz Phonon Excitation. *Phys. Rev. Lett.* **2021**, *126*, 077401.

[187] Fang, H.-H.; Adjokatse, S.; Shao, S.; Even, J.; Loi, M. A. Long-lived hot-carrier light emission and large blue shift in formamidinium tin triiodide perovskites. *Nat. Commun.* **2018**, *9*, 243.

[188] Boudreaux, D. S.; Williams, F.; Nozik, A. J. Hot carrier injection at semiconductor-electrolyte junctions. *J. Appl. Phys.* **1980**, *51*, 2158–2163.

[189] Bockelmann, U.; Bastard, G. Phonon scattering and energy relaxation in two-, one-, and zero-dimensional electron gases. *Phys. Rev. B* **1990**, *42*, 8947–8951.

[190] Efros, A. L.; Kharchenko, V.; Rosen, M. Breaking the phonon bottleneck in nanometer quantum dots: Role of Auger-like processes. *Solid State Commun.* **1995**, *93*, 281–284.

[191] Klimov, V. I.; McBranch, D. W. Femtosecond 1P-to-1S electron relaxation in strongly confined semiconductor nanocrystals. *Phys. Rev. Lett.* **1998**, *80*, 4028–4031.

[192] Klimov, V. I.; McBranch, D. W.; Leatherdale, C. A.; Bawendi, M. G. Electron and hole relaxation pathways in semiconductor quantum dots. *Phys. Rev. B* **1999**, *60*, 13740–13749.

[193] Guyot-Sionnest, P.; Shim, M.; Matranga, C.; Hines, M. Intraband relaxation in CdSe quantum dots. *Phys. Rev. B - Condens. Matter Mater. Phys.* **1999**, *60*, R2181–R2184.

[194] Blackburn, J. L.; Ellingson, R. J.; Mićić, O. I.; Nozik, A. J. Electron Relaxation in Colloidal InP Quantum Dots with Photogenerated Excitons or Chemically Injected Electrons. *J. Phys. Chem. B* **2003**, *107*, 102–109.

[195] Guyot-Sionnest, P.; Wehrenberg, B.; Yu, D. Intraband relaxation in CdSe nanocrystals and the strong influence of the surface ligands. *J. Chem. Phys.* **2005**, *123*, 074709.

[196] Pandey, A.; Guyot-Sionnest, P. Slow Electron Cooling in Colloidal Quantum Dots. *Science* **2008**, *322*, 929–932.

[197] Stranks, S. D.; Burlakov, V. M.; Leijtens, T.; Ball, J. M.; Goriely, A.; Snaith, H. J. Recombination Kinetics in Organic-Inorganic Perovskites: Excitons, Free Charge, and Subgap States. *Phys. Rev. Appl.* **2014**, *2*, 034007.

[198] Sum, T. C.; Mathews, N.; Xing, G.; Lim, S. S.; Chong, W. K.; Giovanni, D.; Dewi, H. A. Spectral Features and Charge Dynamics of Lead Halide Perovskites: Origins and Interpretations. *Acc. Chem. Res.* **2016**, *49*, 294–302.

[199] Emin, D. Barrier to recombination of oppositely charged large polarons. *J. Appl. Phys.* **2018**, *123*, 055105.

[200] Ball, J. M.; Petrozza, A. Defects in perovskite-halides and their effects in solar cells. *Nat. Energy* **2016**, *1*, 16149.

[201] Queisser, H. J.; Haller, E. E. Defects in Semiconductors: Some Fatal, Some Vital. *Science* **1998**, *281*, 945–950.

[202] Brandt, R. E.; Stevanović, V.; Ginley, D. S.; Buonassisi, T. Identifying defect-tolerant semiconductors with high minority-carrier lifetimes: beyond hybrid lead halide perovskites. *MRS Commun.* **2015**, *5*, 265–275.

[203] Buin, A.; Pietsch, P.; Xu, J.; Voznyy, O.; Ip, A. H.; Comin, R.; Sargent, E. H. Materials Processing Routes to Trap-Free Halide Perovskites. *Nano Lett.* **2014**, *14*, 6281–6286.

[204] Yin, W.-J.; Shi, T.; Yan, Y. Unusual defect physics in $CH_3NH_3PbI_3$ perovskite solar cell absorber. *Appl. Phys. Lett.* **2014**, *104*, 063903.

[205] Huang, H.; Bodnarchuk, M. I.; Kershaw, S. V.; Kovalenko, M. V.; Rogach, A. L. Lead Halide Perovskite Nanocrystals in the Research Spotlight: Stability and Defect Tolerance. *ACS Energy Lett.* **2017**, *2*, 2071–2083.

[206] ten Brinck, S.; Zaccaria, F.; Infante, I. Defects in Lead Halide Perovskite Nanocrystals: Analogies and (Many) Differences with the Bulk. *ACS Energy Lett.* **2019**, *4*, 2739–2747.

[207] du Fossé, I.; Mulder, J. T.; Almeida, G.; Spruit, A. G. M.; Infante, I.; Grozema, F. C.; Houtepen, A. J. Limits of Defect Tolerance in Perovskite Nanocrystals: Effect of Local Electrostatic Potential on Trap States. *J. Am. Chem. Soc.* **2022**, *144*, 11059–11063.

[208] Abramczyk, H. *Introduction to Laser Spectroscopy*; Elsevier: Boston, United States, 2005.

[209] Maiman, T. H. Stimulated Optical Radiation in Ruby. *Nature* **1960**, *187*, 493–494.

[210] Svelto, O. *Principles of Lasers*, 5th ed.; Springer: New York, United States, 2010.

[211] Strickland, D.; Mourou, G. Compression of amplified chirped optical pulses. *Opt. Commun.* **1985**, *55*, 447–449.

[212] Kasha, M. Characterization of electronic transitions in complex molecules. *Discuss. Faraday Soc.* **1950**, *9*, 14.

[213] Guo, Y.; Yaffe, O.; Hull, T. D.; Owen, J. S.; Reichman, D. R.; Brus, L. E. Dynamic emission Stokes shift and liquid-like dielectric solvation of band edge carriers in lead-halide perovskites. *Nat. Commun.* **2019**, *10*, 1–8.

[214] Marini, A.; Muñoz-Losa, A.; Biancardi, A.; Mennucci, B. What is Solvatochromism? *J. Phys. Chem. B* **2010**, *114*, 17128–17135.

[215] Mondal, N.; Samanta, A. Complete ultrafast charge carrier dynamics in photo-excited all-inorganic perovskite nanocrystals ($CsPbX_3$). *Nanoscale* **2017**, *9*, 1878–1885.

[216] Manser, J. S.; Kamat, P. V. Band filling with free charge carriers in organometal halide perovskites. *Nat. Photonics* **2014**, *8*, 737–743.

[217] Ghosh, T.; Aharon, S.; Shpatz, A.; Etgar, L.; Ruhman, S. Reflectivity Effects on Pump-Probe Spectra of Lead Halide Perovskites: Comparing Thin Films versus Nanocrystals. *ACS Nano* **2018**, *12*, 5719–5725.

[218] Chen, J.; Messing, M. E.; Zheng, K.; Pullerits, T. Cation-Dependent Hot Carrier Cooling in Halide Perovskite Nanocrystals. *J. Am. Chem. Soc.* **2019**, *141*, 3532–3540.

[219] Papagiorgis, P.; Protesescu, L.; Kovalenko, M. V.; Othonos, A.; Itskos, G. Long-Lived Hot Carriers in Formamidinium Lead Iodide Nanocrystals. *J. Phys. Chem. C* **2017**, *121*, 12434–12440.

[220] Deng, X.; Wen, X.; Huang, S.; Sheng, R.; Harada, T.; Kee, T. W.; Green, M.; Ho-Baillie, A. Ultrafast Carrier Dynamics in Methylammonium Lead Bromide Perovskite. *J. Phys. Chem. C* **2016**, *120*, 2542–2547.

[221] Butkus, J.; Vashishtha, P.; Chen, K.; Gallaher, J. K.; Prasad, S. K. K.; Metin, D. Z.; Laufersky, G.; Gaston, N.; Halpert, J. E.; Hodgkiss, J. M. The Evolution of Quantum Confinement in $CsPbBr_3$ Perovskite Nanocrystals. *Chem. Mater.* **2017**, *29*, 3644–3652.

[222] Shen, Q.; Ripolles, T. S.; Even, J.; Ogomi, Y.; Nishinaka, K.; Izuishi, T.; Nakazawa, N.; Zhang, Y.; Ding, C.; Liu, F.; Toyoda, T.; Yoshino, K.; Minemoto, T.; Katayama, K.; Hayase, S. Slow hot carrier cooling in cesium lead iodide perovskites. *Appl. Phys. Lett.* **2017**, *111*, 153903.

[223] Kaur, G.; Justice Babu, K.; Ghorai, N.; Goswami, T.; Maiti, S.; Ghosh, H. N. Polaron-Mediated Slow Carrier Cooling in a Type-1 3D/0D $CsPbBr_3$@Cs_4PbBr_6 Core-Shell Perovskite System. *J. Phys. Chem. Lett.* **2019**, *10*, 5302–5311.

[224] Muscarella, L. A.; Hutter, E. M.; Frost, J. M.; Grimaldi, G. G.; Versluis, J.; Bakker, H. J.; Ehrler, B. Accelerated Hot-Carrier Cooling in $MAPbI_3$ Perovskite by Pressure-Induced Lattice Compression. *J. Phys. Chem. Lett.* **2021**, *12*, 4118–4124.

[225] Dai, L.; Ye, J.; Greenham, N. C. Thermalization and relaxation mediated by phonon management in tin-lead perovskites. *Light Sci. Appl.* **2023**, *12*, 208.

[226] Lim, J. W. M.; Giovanni, D.; Righetto, M.; Feng, M.; Mhaisalkar, S. G.; Mathews, N.; Sum, T. C. Hot Carriers in Halide Perovskites: How Hot Truly? *J. Phys. Chem. Lett.* **2020**, *11*, 2743–2750.

[227] Esipov, S.; Levinson, Y. The temperature and energy distribution of photoexcited hot electrons. *Adv. Phys.* **1987**, *36*, 331–383.

[228] Villamil Franco, C.; Trippé-Allard, G.; Mahler, B.; Cornaggia, C.; Lauret, J.-S.; Gustavsson, T.; Cassette, E. Exciton Cooling in 2D Perovskite Nanoplatelets: Rationalized Carrier-Induced Stark and Phonon Bottleneck Effects. *J. Phys. Chem. Lett.* **2022**, *13*, 393–399.

[229] Klimov, V. I.; Mikhailovsky, A. A.; McBranch, D. W.; Leatherdale, C. A.; Bawendi, M. G. Mechanisms for intraband energy relaxation in semiconductor quantum dots: The role of electron-hole interactions. *Phys. Rev. B* **2000**, *61*, R13349–R13352.

[230] Wehrenberg, B. L.; Wang, C.; Guyot-Sionnest, P. Interband and Intraband Optical Studies of PbSe Colloidal Quantum Dots. *J. Phys. Chem. B* **2002**, *106*, 10634–10640.

[231] Hopper, T. R.; Gorodetsky, A.; Frost, J. M.; Müller, C.; Lovrincic, R.; Bakulin, A. A. Ultrafast Intraband Spectroscopy of Hot-Carrier Cooling in Lead-Halide Perovskites. *ACS Energy Lett.* **2018**, *3*, 2199–2205.

[232] Hopper, T. R.; Gorodetsky, A.; Jeong, A.; Krieg, F.; Bodnarchuk, M. I.; Maimaris, M.; Chaplain, M.; Macdonald, T. J.; Huang, X.; Lovrincic, R.; Kovalenko, M. V.; Bakulin, A. A. Hot Carrier Dynamics in Perovskite Nanocrystal Solids: Role of the Cold Carriers, Nanoconfinement, and the Surface. *Nano Lett.* **2020**, *20*, 2271–2278.

[233] Zheng, X.; Hopper, T. R.; Gorodetsky, A.; Maimaris, M.; Xu, W.; Martin, B. A. A.; Frost, J. M.; Bakulin, A. A. Multipulse Terahertz Spectroscopy Unveils Hot Polaron Photoconductivity Dynamics in Metal-Halide Perovskites. *J. Phys. Chem. Lett.* **2021**, *12*, 8732–8739.

[234] Carwithen, B. P. et al. Confinement and Exciton Binding Energy Effects on Hot Carrier Cooling in Lead Halide Perovskite Nanomaterials. *ACS Nano* **2023**, *17*, 6638–6648.

[235] Ulatowski, A. M.; Farrar, M. D.; Snaith, H. J.; Johnston, M. B.; Herz, L. M. Revealing Ultrafast Charge-Carrier Thermalization in Tin-Iodide Perovskites through Novel Pump-Push-Probe Terahertz Spectroscopy. *ACS Photonics* **2021**, *8*, 2509–2518.

[236] Righetto, M.; Lim, S. S.; Giovanni, D.; Lim, J. W. M.; Zhang, Q.; Ramesh, S.; Tay, Y. K. E.; Sum, T. C. Hot carriers perspective on the nature of traps in perovskites. *Nat. Commun.* **2020**, *11*, 2712.

[237] Lim, S. S.; Giovanni, D.; Zhang, Q.; Solanki, A.; Jamaludin, N. F.; Lim, J. W. M.; Mathews, N.; Mhaisalkar, S.; Pshenichnikov, M. S.; Sum, T. C. Hot carrier extraction in $CH_3NH_3PbI_3$ unveiled by pump-push-probe spectroscopy. *Sci. Adv.* **2019**, *5*, eaax3620.

[238] Dana, J.; Binyamin, T.; Etgar, L.; Ruhman, S. Unusually Strong Biexciton Repulsion Detected in Quantum Confined $CsPbBr_3$ Nanocrystals with Two and Three Pulse Femtosecond Spectroscopy. *ACS Nano* **2021**, *15*, 9039–9047.

[239] Feng, M.; Ye, S.; Lim, J. W. M.; Guo, Y.; Cai, R.; Zhang, Q.; He, H.; Sum, T. C. Insights to Carrier-Phonon Interactions in Lead Halide Perovskites via Multi-Pulse Manipulation. *Small* **2023**, *2301831*, 1–8.

[240] Weinstein, E. W. "Fourier Series" from *MathWorld* – A Wolfram Web Resource. accessed 31-08-2023.

[241] Weinstein, E. W. "Fourier Transform" from *MathWorld* – A Wolfram Web Resource. accessed 31-08-2023.

[242] Wu, K.; Bera, A.; Ma, C.; Du, Y.; Yang, Y.; Li, L.; Wu, T. Temperature-dependent excitonic photoluminescence of hybrid organometal halide perovskite films. *Phys. Chem. Chem. Phys.* **2014**, *16*, 22476–22481.

[243] Savenije, T. J.; Ponseca, C. S.; Kunneman, L.; Abdellah, M.; Zheng, K.; Tian, Y.; Zhu, Q.; Canton, S. E.; Scheblykin, I. G.; Pullerits, T.; Yartsev, A.; Sundström, V. Thermally Activated Exciton Dissociation and Recombination Control the Carrier Dynamics in Organometal Halide Perovskite. *J. Phys. Chem. Lett.* **2014**, *5*, 2189–2194.

[244] Sun, S.; Salim, T.; Mathews, N.; Duchamp, M.; Boothroyd, C.; Xing, G.; Sum, T. C.; Lam, Y. M. The origin of high efficiency in low-temperature solution-processable bilayer organometal halide hybrid solar cells. *Energy Environ. Sci.* **2014**, *7*, 399–407.

[245] Galkowski, K.; Mitioglu, A.; Miyata, A.; Plochocka, P.; Portugall, O.; Eperon, G. E.; Wang, J. T. W.; Stergiopoulos, T.; Stranks, S. D.; Snaith, H. J.; Nicholas, R. J. Determination of the exciton binding energy and effective masses for methylammonium and formamidinium lead tri-halide perovskite semiconductors. *Energy Environ. Sci.* **2016**, *9*, 962–970.

[246] Hirasawa, M.; Ishihara, T.; Goto, T.; Uchida, K.; Miura, N. Magnetoabsorption of the lowest exciton in perovskite-type compound (CH_3NH_3)PbI_3. *Phys. B Condens. Matter* **1994**, *201*, 427–430.

[247] Lin, Q.; Armin, A.; Nagiri, R. C. R.; Burn, P. L.; Meredith, P. Electro-optics of perovskite solar cells. *Nat. Photonics* **2015**, *9*, 106–112.

[248] Menéndez-Proupin, E.; Palacios, P.; Wahnón, P.; Conesa, J. C. Self-consistent relativistic band structure of the $CH_3NH_3PbI_3$ perovskite. *Phys. Rev. B* **2014**, *90*, 045207.

[249] Elliott, R. J. Intensity of optical absorption by excitons. *Phys. Rev.* **1957**, *108*, 1384–1389.

[250] Chen, X.; Lu, H.; Yang, Y.; Beard, M. C. Excitonic Effects in Methylammonium Lead Halide Perovskites. *J. Phys. Chem. Lett.* **2018**, *9*, 2595–2603.

[251] Wright, A. D.; Volonakis, G.; Borchert, J.; Davies, C. L.; Giustino, F.; Johnston, M. B.; Herz, L. M. Intrinsic quantum confinement in formamidinium lead triiodide perovskite. *Nat. Mater.* **2020**, *19*, 1201–1206.

[252] Ruf, F.; Aygüler, M. F.; Giesbrecht, N.; Rendenbach, B.; Magin, A.; Docampo, P.; Kalt, H.; Hetterich, M. Temperature-dependent studies of exciton binding energy and phase-transition suppression in (Cs,FA,MA)Pb(I,Br)$_3$ perovskites. *APL Mater.* **2019**, *7*, 031113.

[253] Uchiki, H.; Arakawa, Y.; Sakaki, H.; Kobayashi, T. Hot photoluminescence of GaAs-AlGaAs multiple quantum well structures under high excitation by a single shot of 30 ps, 532 nm laser. *Solid State Commun.* **1985**, *55*, 311–315.

[254] Lyon, S. Spectroscopy of hot carriers in semiconductors. *J. Lumin.* **1986**, *35*, 121–154.

[255] Leo, K.; Rühle, W. W.; Ploog, K. Hot-carrier energy-loss rates in GaAs/$Al_xGa_{1-x}As$ quantum wells. *Phys. Rev. B* **1988**, *38*, 1947–1957.

[256] Leo, K.; Rühle, W. W.; Queisser, H. J.; Ploog, K. Reduced dimensionality of hot-carrier relaxation in GaAs quantum wells. *Phys. Rev. B* **1988**, *37*, 7121–7124.

[257] Pelouch, W. S.; Ellingson, R. J.; Powers, P. E.; Tang, C. L.; Szmyd, D. M.; Nozik, A. J. Comparison of hot-carrier relaxation in quantum wells and bulk GaAs at high carrier densities. *Phys. Rev. B* **1992**, *45*, 1450–1453.

[258] Rosenwaks, Y.; Hanna, M. C.; Levi, D. H.; Szmyd, D. M.; Ahrenkiel, R. K.; Nozik, A. J. Hot-carrier cooling in GaAs: Quantum wells versus bulk. *Phys. Rev. B* **1993**, *48*, 14675–14678.

[259] Li, M.; Bhaumik, S.; Goh, T. W.; Kumar, M. S.; Yantara, N.; Grätzel, M.; Mhaisalkar, S.; Mathews, N.; Sum, T. C. Slow cooling and highly efficient extraction of hot carriers in colloidal perovskite nanocrystals. *Nat. Commun.* **2017**, *8*, 14350.

[260] Li, Y.; Lai, R.; Luo, X.; Liu, X.; Ding, T.; Lu, X.; Wu, K. On the absence of a phonon bottleneck in strongly confined $CsPbBr_3$ perovskite nanocrystals. *Chem. Sci.* **2019**, *10*, 5983–5989.

[261] Boehme, S. C.; Brinck, S. T.; Maes, J.; Yazdani, N.; Zapata, F.; Chen, K.; Wood, V.; Hodgkiss, J. M.; Hens, Z.; Geiregat, P.; Infante, I. Phonon-Mediated and Weakly Size-Dependent Electron and Hole Cooling in $CsPbBr_3$ Nanocrystals Revealed by Atomistic Simulations and Ultrafast Spectroscopy. *Nano Lett.* **2020**, *20*, 1819–1829.

[262] Diroll, B. T.; Schaller, R. D. Intraband Cooling in All-Inorganic and Hybrid Organic-Inorganic Perovskite Nanocrystals. *Adv. Funct. Mater.* **2019**, *29*, 1–8.

[263] Hintermayr, V. A.; Polavarapu, L.; Urban, A. S.; Feldmann, J. Accelerated Carrier Relaxation through Reduced Coulomb Screening in Two-Dimensional Halide Perovskite Nanoplatelets. *ACS Nano* **2018**, *12*, 10151–10158.

[264] Shukla, A.; Kaur, G.; Babu, K. J.; Ghorai, N.; Goswami, T.; Kaur, A.; Ghosh, H. N. Effect of Confinement on the Exciton and Biexciton Dynamics in Perovskite 2D-Nanosheets and 3D-Nanocrystals. *J. Phys. Chem. Lett.* **2020**, *11*, 6344–6352.

[265] Yin, J.; Maity, P.; Naphade, R.; Cheng, B.; He, J.-H.; Bakr, O. M.; Brédas, J.-L.; Mohammed, O. F. Tuning Hot Carrier Cooling Dynamics by Dielectric Confinement in Two-Dimensional Hybrid Perovskite Crystals. *ACS Nano* **2019**, *13*, 12621–12629.

[266] Maity, P.; Yin, J.; Cheng, B.; He, J. H.; Bakr, O. M.; Mohammed, O. F. Layer-Dependent Coherent Acoustic Phonons in Two-Dimensional Ruddlesden-Popper Perovskite Crystals. *J. Phys. Chem. Lett.* **2019**, *10*, 5259–5264.

[267] Jia, X.; Jiang, J.; Zhang, Y.; Qiu, J.; Wang, S.; Chen, Z.; Yuan, N.; Ding, J. Observation of enhanced hot phonon bottleneck effect in 2D perovskites. *Appl. Phys. Lett.* **2018**, *112*, 143903.

[268] Lee, K. J. et al. Perovskite-Based Artificial Multiple Quantum Wells. *Nano Lett.* **2019**, *19*, 3535–3542.

[269] Li, H. et al. Enhanced Hot-Phonon Bottleneck Effect on Slowing Hot Carrier Cooling in Metal Halide Perovskite Quantum Dots with Alloyed A-Site. *Adv. Mater.* **2023**, *2301834*, 1–13.

[270] Narra, S.; Chung, C.-c.; Diau, E. W.-g.; Shigeto, S. Simultaneous Observation of an Intraband Transition and Distinct Transient Species in the Infrared Region for Perovskite Solar Cells. *J. Phys. Chem. Lett.* **2016**, *7*, 2450–2455.

[271] Munson, K. T.; Grieco, C.; Kennehan, E. R.; Stewart, R. J.; Asbury, J. B. Time-Resolved Infrared Spectroscopy Directly Probes Free and Trapped Carriers in Organo-Halide Perovskites. *ACS Energy Lett.* **2017**, *2*, 651–658.

[272] Giorgi, G.; Fujisawa, J.-I.; Segawa, H.; Yamashita, K. Small Photocarrier Effective Masses Featuring Ambipolar Transport in Methylammonium Lead Iodide Perovskite: A Density Functional Analysis. *J. Phys. Chem. Lett.* **2013**, *4*, 4213–4216.

[273] Hopper, T. R. Ultrafast photophysics and energy losses in emerging photovoltaic materials and devices. Ph.D. thesis, Imperial College London, 2020.

[274] Dahod, N. S.; France-Lanord, A.; Paritmongkol, W.; Grossman, J. C.; Tisdale, W. A. Low-frequency Raman spectrum of 2D layered perovskites: Local atomistic motion or superlattice modes? *J. Chem. Phys.* **2020**, *153*, 044710.

[275] Zhang, X.; Shi, H.; Cai, R.; Zhang, W.; Liu, H.; Yang, Y.; Dai, H.; Zhang, X.; Wang, K.; Sun, X. W. Formamidinium-Based Quasi-2D Perovskite Nanoplates With Dimensionally Tuned Optical Properties. *IEEE Trans. Nanotechnol.* **2018**, *17*, 1165–1170.

[276] Gramlich, M.; Lampe, C.; Drewniok, J.; Urban, A. S. How Exciton-Phonon Coupling Impacts Photoluminescence in Halide Perovskite Nanoplatelets. *J. Phys. Chem. Lett.* **2021**, *12*, 11371–11377.

[277] Zeng, P.; Ren, X.; Wei, L.; Zhao, H.; Liu, X.; Zhang, X.; Xu, Y.; Yan, L.; Boldt, K.; Smith, T. A.; Liu, M. Control of Hot Carrier Relaxation in $CsPbBr_3$ Nanocrystals Using Damping Ligands. *Angew. Chem.* **2022**, *134*, e202111443.

[278] Kahmann, S.; Shao, S.; Loi, M. A. Cooling, Scattering, and Recombination – The Role of the Material Quality for the Physics of Tin Halide Perovskites. *Adv. Funct. Mater.* **2019**, *29*.

[279] Dana, J.; Ghosh, T.; Gdor, I.; Shapiro, A.; Lifshitz, E.; Ruhman, S. Spectator Exciton Effects on Nanocrystal Photophysics II: PbS. *J. Phys. Chem. C* **2022**, *126*, 19304–19310.

[280] Hendry, E.; Koeberg, M.; Wang, F.; Zhang, H.; de Mello Donegá, C.; Vanmaekelbergh, D.; Bonn, M. Direct Observation of Electron-to-Hole Energy Transfer in CdSe Quantum Dots. *Phys. Rev. Lett.* **2006**, *96*, 057408.

[281] Xu, J.; Guo, Z.; Zhou, Q.; Wang, Y.; Xue, Z.; Han, Y.; Yang, W.; Ma, X. Exciton-Phonon Coupling and Vibronic Emission Structure in 2D Perovskite Thin Films with Naphthylmethylamine Spacers. *J. Phys. Chem. C* **2023**, 10.1021/acs.jpcc.3c02743.

[282] Sun, Q.; Gong, J.; Yan, X.; Wu, Y.; Cui, R.; Tian, W.; Jin, S.; Wang, Y. Elucidating the Unique Hot Carrier Cooling in Two-Dimensional Inorganic Halide Perovskites: The Role of Out-of-Plane Carrier-Phonon Coupling. *Nano Lett.* **2022**, *22*, 2995–3002.

[283] Gao, Y.; Talgorn, E.; Aerts, M.; Trinh, M. T.; Schins, J. M.; Houtepen, A. J.; Siebbeles, L. D. A. Enhanced Hot-Carrier Cooling and Ultrafast Spectral Diffusion in Strongly Coupled PbSe Quantum-Dot Solids. *Nano Lett.* **2011**, *11*, 5471–5476.

[284] Cao, W.; Yuan, L.; Patterson, R.; Wen, X.; Tapping, P. C.; Kee, T.; Veetil, B. P.; Zhang, P.; Zhang, Z.; Zhang, Q.; Reece, P.; Bremner, S.; Shrestha, S.; Conibeer, G.; Huang, S. Difference in hot carrier cooling rate between Langmuir-Blodgett and drop cast PbS QD films due to strong electron-phonon coupling. *Nanoscale* **2017**, *9*, 17133–17142.

[285] Delor, M.; Weaver, H. L.; Yu, Q.; Ginsberg, N. S. Imaging material functionality through three-dimensional nanoscale tracking of energy flow. *Nat. Mater.* **2020**, *19*, 56–62.

[286] Elbaz, G. A.; Ong, W.-L.; Doud, E. A.; Kim, P.; Paley, D. W.; Roy, X.; Malen, J. A. Phonon Speed, Not Scattering, Differentiates Thermal Transport in Lead Halide Perovskites. *Nano Lett.* **2017**, *17*, 5734–5739.

[287] Giri, A.; Chen, A. Z.; Mattoni, A.; Aryana, K.; Zhang, D.; Hu, X.; Lee, S.-H.; Choi, J. J.; Hopkins, P. E. Ultralow Thermal Conductivity of Two-Dimensional Metal Halide Perovskites. *Nano Lett.* **2020**, *20*, 3331–3337.

[288] Cingolani, R.; Calcagnile, L.; Colí, G.; Rinaldi, R.; Lomoscolo, M.; DiDio, M.; Franciosi, A.; Vanzetti, L.; LaRocca, G. C.; Campi, D. Radiative recombination processes in wide-band-gap II-VI quantum wells: the interplay between excitons and free carriers. *J. Opt. Soc. Am. B* **1996**, *13*, 1268.

[289] D'Innocenzo, V.; Grancini, G.; Alcocer, M. J. P.; Kandada, A. R. S.; Stranks, S. D.; Lee, M. M.; Lanzani, G.; Snaith, H. J.; Petrozza, A. Excitons versus free charges in organo-lead tri-halide perovskites. *Nat. Commun.* **2014**, *5*, 3586.

[290] Gélvez-Rueda, M. C.; Hutter, E. M.; Cao, D. H.; Renaud, N.; Stoumpos, C. C.; Hupp, J. T.; Savenije, T. J.; Kanatzidis, M. G.; Grozema, F. C. Interconversion between Free Charges and Bound Excitons in 2D Hybrid Lead Halide Perovskites. *J. Phys. Chem. C* **2017**, *121*, 26566–26574.

[291] Li, J.; Yuan, X.; Jing, P.; Li, J.; Wei, M.; Hua, J.; Zhao, J.; Tian, L. Temperature-dependent photoluminescence of inorganic perovskite nanocrystal films. *RSC Adv.* **2016**, *6*, 78311–78316.

[292] Li, J.; Luo, L.; Huang, H.; Ma, C.; Ye, Z.; Zeng, J.; He, H. 2D Behaviors of Excitons in Cesium Lead Halide Perovskite Nanoplatelets. *J. Phys. Chem. Lett.* **2017**, *8*, 1161–1168.

[293] Grancini, G.; Srimath Kandada, A. R.; Frost, J. M.; Barker, A. J.; De Bastiani, M.; Gandini, M.; Marras, S.; Lanzani, G.; Walsh, A.; Petrozza, A. Role of microstructure in the electron-hole interaction of hybrid lead halide perovskites. *Nat. Photonics* **2015**, *9*, 695–701.

[294] Elmestekawy, K. A.; Wright, A. D.; Lohmann, K. B.; Borchert, J.; Johnston, M. B.; Herz, L. M. Controlling Intrinsic Quantum Confinement in Formamidinium Lead Triiodide Perovskite through Cs Substitution. *ACS Nano* **2022**, *16*, 9640–9650.

[295] Hopper, T. R.; Jeong, A.; Gorodetsky, A. A.; Krieg, F.; Bodnarchuk, M. I.; Huang, X.; Lovrincic, R.; Kovalenko, M. V.; Bakulin, A. A. Kinetic modelling of intraband carrier relaxation in bulk and nanocrystalline lead-halide perovskites. *Phys. Chem. Chem. Phys.* **2020**, *22*, 17605–17611.

[296] Faber, T.; Filipovic, L.; Koster, L. J. A. The Role of Thermalization in the Cooling Dynamics of Hot Carrier Solar Cells. *Sol. RRL* **2023**, *7*, 2300140.

[297] Kim, J.; Chung, C.-H.; Hong, K.-H. Understanding of the formation of shallow level defects from the intrinsic defects of lead tri-halide perovskites. *Phys. Chem. Chem. Phys.* **2016**, *18*, 27143–27147.

[298] Buin, A.; Comin, R.; Xu, J.; Ip, A. H.; Sargent, E. H. Halide-Dependent Electronic Structure of Organolead Perovskite Materials. *Chem. Mater.* **2015**, *27*, 4405–4412.

[299] Nenon, D. P.; Pressler, K.; Kang, J.; Koscher, B. A.; Olshansky, J. H.; Osowiecki, W. T.; Koc, M. A.; Wang, L.-W.; Alivisatos, A. P. Design Principles for Trap-Free $CsPbX_3$ Nanocrystals: Enumerating and Eliminating Surface Halide Vacancies with Softer Lewis Bases. *J. Am. Chem. Soc.* **2018**, *140*, 17760–17772.

[300] McMeekin, D. P.; Sadoughi, G.; Rehman, W.; Eperon, G. E.; Saliba, M.; Hörantner, M. T.; Haghighirad, A.; Sakai, N.; Korte, L.; Rech, B.; Johnston, M. B.; Herz, L. M.; Snaith, H. J. A mixed-cation lead mixed-halide perovskite absorber for tandem solar cells. *Science* **2016**, *351*, 151–155.

[301] Ganose, A. M.; Scanlon, D. O.; Walsh, A.; Hoye, R. L. Z. The defect challenge of wide-bandgap semiconductors for photovoltaics and beyond. *Nat. Commun.* **2022**, *13*, 4715.

[302] Guo, D.; Bartesaghi, D.; Wei, H.; Hutter, E. M.; Huang, J.; Savenije, T. J. Photoluminescence from Radiative Surface States and Excitons in Methylammonium Lead Bromide Perovskites. *J. Phys. Chem. Lett.* **2017**, *8*, 4258–4263.

[303] Abdi-Jalebi, M. et al. Maximizing and stabilizing luminescence from halide perovskites with potassium passivation. *Nature* **2018**, *555*, 497–501.

[304] Hu, Y. et al. Understanding the Role of Cesium and Rubidium Additives in Perovskite Solar Cells: Trap States, Charge Transport, and Recombination. *Adv. Energy Mater.* **2018**, *8*, 1–11.

[305] Qiao, L.; Fang, W.; Long, R.; Prezhdo, O. V. Extending Carrier Lifetimes in Lead Halide Perovskites with Alkali Metals by Passivating and Eliminating Halide Interstitial Defects. *Angew. Chem.* **2020**, *132*, 4714–4720.

[306] Ye, J.; Byranvand, M. M.; Martínez, C. O.; Hoye, R. L. Z.; Saliba, M.; Polavarapu, L. Defect Passivation in Lead-Halide Perovskite Nanocrystals and Thin Films: Toward Efficient LEDs and Solar Cells. *Angew. Chem. Int. Ed.* **2021**, *60*, 21636–21660.

[307] Shen, W.; Wu, Z.; Yang, G.; Kong, Y.; Li, W.; Liang, G.; Huang, F.; Cheng, Y.-B.; Zhong, J. Differentiated Functions of Potassium Interface Passivation and Doping on Charge-Carrier Dynamics in Perovskite Solar Cells. *J. Phys. Chem. Lett.* **2022**, *13*, 3188–3196.

[308] Bretschneider, S. A.; Laquai, F.; Bonn, M. Trap-Free Hot Carrier Relaxation in Lead-Halide Perovskite Films. *J. Phys. Chem. C* **2017**, *121*, 11201–11206.

[309] Jiang, X.; Hoffman, J.; Stoumpos, C. C.; Kanatzidis, M. G.; Harel, E. Transient Sub-Band-Gap States at Grain Boundaries of $CH_3NH_3PbI_3$ Perovskite Act as Fast Temperature Relaxation Centers. *ACS Energy Lett.* **2019**, *4*, 1741–1747.

[310] Zheng, K.; Žídek, K.; Abdellah, M.; Chen, J.; Chábera, P.; Zhang, W.; Al-Marri, M. J.; Pullerits, T. High Excitation Intensity Opens a New Trapping Channel in Organic-Inorganic Hybrid Perovskite Nanoparticles. *ACS Energy Lett.* **2016**, *1*, 1154–1161.

[311] Wang, X.; Huo, D.; Wang, X.; Li, M.; Wang, Y.; Wan, Y. Hot Carrier Dynamics and Charge Trapping in Surface Passivated β-$CsPbI_3$ Inorganic Perovskite. *J. Phys. Chem. Lett.* **2021**, *12*, 6907–6913.

[312] Zhu, L.; Zhao, R.; Zhuang, R.; Wu, T.; Xie, L.; Hua, Y. Slowing the hot-carrier cooling by an organic small molecule in perovskite solar cells. *EcoMat* **2023**, *5*, 1–8.

[313] Zhuang, R.; Wang, L.; Qiu, J.; Xie, L.; Miao, X.; Zhang, X.; Hua, Y. Effect of molecular configuration of additives on perovskite crystallization and hot carriers behavior in perovskite solar cells. *Chem. Eng. J.* **2023**, *463*, 142449.

[314] Zhou, Z.; He, J.; Frauenheim, T.; Prezhdo, O. V.; Wang, J. Control of Hot Carrier Cooling in Lead Halide Perovskites by Point Defects. *J. Am. Chem. Soc.* **2022**, *144*, 18126–18134.

[315] Das, A.; Marjit, K.; Ghosh, S.; Ghosh, D.; Patra, A. Slowing Down the Hot Carrier Relaxation Dynamics of $CsPbX_3$ Nanocrystals by the Surface Passivation Strategy. *J. Phys. Chem. C* **2023**, *127*, 15385–15394.

[316] Wang, T.; Jin, L.; Hidalgo, J.; Chu, W.; Snaider, J. M.; Deng, S.; Zhu, T.; Lai, B.; Prezhdo, O.; Correa-Baena, J.-P.; Huang, L. Protecting hot carriers by tuning hybrid perovskite structures with alkali cations. *Sci. Adv.* **2020**, *6*.

[317] Ye, J. et al. Elucidating the Role of Antisolvents on the Surface Chemistry and Optoelectronic Properties of $CsPbBr_xI_{3-x}$ Perovskite Nanocrystals. *J. Am. Chem. Soc.* **2022**, *144*, 12102–12115.

[318] Otero-Martínez, C.; Imran, M.; Schrenker, N. J.; Ye, J.; Ji, K.; Rao, A.; Stranks, S. D.; Hoye, R. L. Z.; Bals, S.; Manna, L.; Pérez-Juste, J.; Polavarapu, L. Fast A-Site Cation Cross-Exchange at Room Temperature: Single- to Double- and Triple-Cation Halide Perovskite Nanocrystals. *Angew. Chem. Int. Ed.* **2022**, *61*, e202205617.

[319] Pan, A.; He, B.; Fan, X.; Liu, Z.; Urban, J. J.; Alivisatos, A. P.; He, L.; Liu, Y. Insight into the Ligand-Mediated Synthesis of Colloidal $CsPbBr_3$ Perovskite Nanocrystals: The Role of Organic Acid, Base, and Cesium Precursors. *ACS Nano* **2016**, *10*, 7943–7954.

[320] ten Brinck, S.; Infante, I. Surface Termination, Morphology, and Bright Photoluminescence of Cesium Lead Halide Perovskite Nanocrystals. *ACS Energy Lett.* **2016**, *1*, 1266–1272.

[321] Caselli, V. M.; Thieme, J.; Jöbsis, H. J.; Phadke, S. A.; Zhao, J.; Hutter, E. M.; Savenije, T. J. Traps in the spotlight: How traps affect the charge carrier dynamics in $Cs_2AgBiBr_6$ perovskite. *Cell Reports Phys. Sci.* **2022**, *3*, 101055.

[322] Kokil, A.; Yang, K.; Kumar, J. Techniques for characterization of charge carrier mobility in organic semiconductors. *J. Polym. Sci. Part B Polym. Phys.* **2012**, *50*, 1130–1144.

[323] Maculan, G.; Sheikh, A. D.; Abdelhady, A. L.; Saidaminov, M. I.; Haque, M. A.; Murali, B.; Alarousu, E.; Mohammed, O. F.; Wu, T.; Bakr, O. M. $CH_3NH_3PbCl_3$ Single Crystals: Inverse Temperature Crystallization and Visible-Blind UV-Photodetector. *J. Phys. Chem. Lett.* **2015**, *6*, 3781–3786.

[324] Zhumekenov, A. A.; Saidaminov, M. I.; Haque, M. A.; Alarousu, E.; Sarmah, S. P.; Murali, B.; Dursun, I.; Miao, X.-H.; Abdelhady, A. L.; Wu, T.; Mohammed, O. F.; Bakr, O. M. Formamidinium Lead Halide Perovskite Crystals with Unprecedented Long Carrier Dynamics and Diffusion Length. *ACS Energy Lett.* **2016**, *1*, 32–37.

[325] Saidaminov, M. I.; Abdelhady, A. L.; Murali, B.; Alarousu, E.; Burlakov, V. M.; Peng, W.; Dursun, I.; Wang, L.; He, Y.; Maculan, G.; Goriely, A.; Wu, T.; Mohammed, O. F.; Bakr, O. M. High-quality bulk hybrid perovskite single crystals within minutes by inverse temperature crystallization. *Nat. Commun.* **2015**, *6*, 7586.

[326] Takahashi, Y.; Hasegawa, H.; Takahashi, Y.; Inabe, T. Hall mobility in tin iodide perovskite $CH_3NH_3SnI_3$: Evidence for a doped semiconductor. *J. Solid State Chem.* **2013**, *205*, 39–43.

[327] Dong, Q.; Fang, Y.; Shao, Y.; Mulligan, P.; Qiu, J.; Cao, L.; Huang, J. Electron-hole diffusion lengths >175 µm in solution-grown $CH_3NH_3PbI_3$ single crystals. *Science* **2015**, *347*, 967–970.

[328] Shi, D. et al. Low trap-state density and long carrier diffusion in organolead trihalide perovskite single crystals. *Science* **2015**, *347*, 519–522.

[329] Matsushima, T.; Hwang, S.; Sandanayaka, A. S.; Qin, C.; Terakawa, S.; Fujihara, T.;

Yahiro, M.; Adachi, C. Solution-Processed Organic-Inorganic Perovskite Field-Effect Transistors with High Hole Mobilities. *Adv. Mater.* **2016**, *28*, 10275–10281.

[330] Kagan, C. R.; Mitzi, D. B.; Dimitrakopoulos, C. D. Organic-Inorganic Hybrid Materials as Semiconducting Channels in Thin-Film Field-Effect Transistors. *Science* **1999**, *286*, 945–947.

[331] Herz, L. M. Charge-Carrier Mobilities in Metal Halide Perovskites: Fundamental Mechanisms and Limits. *ACS Energy Lett.* **2017**, *2*, 1539–1548.

[332] Muscarella, L. A.; Hutter, E. M.; Sanchez, S.; Dieleman, C. D.; Savenije, T. J.; Hagfeldt, A.; Saliba, M.; Ehrler, B. Crystal Orientation and Grain Size: Do They Determine Optoelectronic Properties of $MAPbI_3$ Perovskite? *J. Phys. Chem. Lett.* **2019**, *10*, 6010–6018.

[333] Beard, M. C.; Turner, G. M.; Schmuttenmaer, C. A. Terahertz Spectroscopy. *J. Phys. Chem. B* **2002**, *106*, 7146–7159.

[334] Ulbricht, R.; Hendry, E.; Shan, J.; Heinz, T. F.; Bonn, M. Carrier dynamics in semiconductors studied with time-resolved terahertz spectroscopy. *Rev. Mod. Phys.* **2011**, *83*, 543–586.

[335] Baxter, J. B.; Guglietta, G. W. Terahertz Spectroscopy. *Anal. Chem.* **2011**, *83*, 4342–4368.

[336] Neu, J.; Schmuttenmaer, C. A. Tutorial: An introduction to terahertz time domain spectroscopy (THz-TDS). *J. Appl. Phys.* **2018**, *124*, 231101.

[337] Nienhuys, H.-K.; Sundström, V. Intrinsic complications in the analysis of optical-pump, terahertz probe experiments. *Phys. Rev. B* **2005**, *71*, 235110.

[338] Tiwana, P.; Parkinson, P.; Johnston, M. B.; Snaith, H. J.; Herz, L. M. Ultrafast Terahertz Conductivity Dynamics in Mesoporous TiO_2: Influence of Dye Sensitization and Surface Treatment in Solid-State Dye-Sensitized Solar Cells. *J. Phys. Chem. C* **2010**, *114*, 1365–1371.

[339] Savenije, T. J.; Guo, D.; Caselli, V. M.; Hutter, E. M. Quantifying Charge-Carrier Mobilities and Recombination Rates in Metal Halide Perovskites from Time-Resolved Microwave Photoconductivity Measurements. *Adv. Energy Mater.* **2020**, *10*, 1–12.

[340] Hempel, H. et al. Predicting Solar Cell Performance from Terahertz and Microwave Spectroscopy. *Adv. Energy Mater.* **2022**, *12*.

[341] Lim, J.; Kober-Czerny, M.; Lin, Y.-H.; Ball, J. M.; Sakai, N.; Duijnstee, E. A.; Hong, M. J.; Labram, J. G.; Wenger, B.; Snaith, H. J. Long-range charge carrier mobility in metal halide perovskite thin-films and single crystals via transient photo-conductivity. *Nat. Commun.* **2022**, *13*, 4201.

[342] Ponseca, C. S.; Savenije, T. J.; Abdellah, M.; Zheng, K.; Yartsev, A.; Pascher, T.; Harlang, T.; Chabera, P.; Pullerits, T.; Stepanov, A.; Wolf, J.-P.; Sundström, V. Organometal Halide Perovskite Solar Cell Materials Rationalized: Ultrafast Charge Generation, High and Microsecond-Long Balanced Mobilities, and Slow Recombination. *J. Am. Chem. Soc.* **2014**, *136*, 5189–5192.

[343] Zhao, D.; Hu, H.; Haselsberger, R.; Marcus, R. A.; Michel-Beyerle, M.-E.; Lam, Y. M.; Zhu, J.-X.; La-o vorakiat, C.; Beard, M. C.; Chia, E. E. M. Monitoring Electron-Phonon Interactions in Lead Halide Perovskites Using Time-Resolved THz Spectroscopy. *ACS Nano* **2019**, *13*, 8826–8835.

[344] Iaru, C. M.; Brodu, A.; van Hoof, N. J. J.; ter Huurne, S. E. T.; Buhot, J.; Montanarella, F.; Buhbut, S.; Christianen, P. C. M.; Vanmaekelbergh, D.; de Mello Donega, C.; Rivas, J. G.; Koenraad, P. M.; Silov, A. Y. Fröhlich interaction dominated by a single phonon mode in $CsPbBr_3$. *Nat. Commun.* **2021**, *12*, 5844.

[345] Xia, C. Q.; Poncé, S.; Peng, J.; Ulatowski, A. M.; Patel, J. B.; Wright, A. D.; Milot, R. L.; Kraus, H.; Lin, Q.; Herz, L. M.; Giustino, F.; Johnston, M. B. Ultrafast photo-induced phonon hardening due to Pauli blocking in $MAPbI_3$ single-crystal and polycrystalline perovskites. *J. Phys. Mater.* **2021**, *4*, 044017.

[346] Guzelturk, B.; Belisle, R. A.; Smith, M. D.; Bruening, K.; Prasanna, R.; Yuan, Y.; Gopalan, V.; Tassone, C. J.; Karunadasa, H. I.; McGehee, M. D.; Lindenberg, A. M. Terahertz Emission from Hybrid Perovskites Driven by Ultrafast Charge Separation and Strong Electron-Phonon Coupling. *Adv. Mater.* **2018**, *30*, 1704737.

[347] Bretschneider, S. A.; Ivanov, I.; Wang, H. I.; Miyata, K.; Zhu, X.; Bonn, M. Quantifying Polaron Formation and Charge Carrier Cooling in Lead-Iodide Perovskites. *Adv. Mater.* **2018**, *30*, 1–8.

[348] Lan, Y.; Dringoli, B. J.; Valverde-Chávez, D. A.; Ponseca, C. S.; Sutton, M.; He, Y.; Kanatzidis, M. G.; Cooke, D. G. Ultrafast correlated charge and lattice motion in a hybrid metal halide perovskite. *Sci. Adv.* **2019**, *5*, eaaw5558.

[349] Burgos-Caminal, A.; Moreno-Naranjo, J. M.; Willauer, A. R.; Paraecattil, A. A.; Ajdarzadeh, A.; Moser, J.-E. Hot Carrier Mobility Dynamics Unravel Competing Subpicosecond Processes in Lead Halide Perovskites. *J. Phys. Chem. C* **2021**, *125*, 98–106.

[350] Monti, M.; Jayawardena, K. D. G. I.; Butler-Caddle, E.; Bandara, R. M. I.; Woolley, J. M.; Staniforth, M.; Silva, S. R. P.; Lloyd-Hughes, J. Hot carriers in mixed Pb-Sn halide perovskite semiconductors cool slowly while retaining their electrical mobility. *Phys. Rev. B* **2020**, *102*, 245204.

[351] Karakus, M.; Jensen, S. A.; D'Angelo, F.; Turchinovich, D.; Bonn, M.; Cánovas, E. Phonon-Electron Scattering Limits Free Charge Mobility in Methylammonium Lead Iodide Perovskites. *J. Phys. Chem. Lett.* **2015**, *6*, 4991–4996.

[352] Zhang, H.; Debroye, E.; Zheng, W.; Fu, S.; Virgilio, L. D.; Kumar, P.; Bonn, M.; Wang, H. I. Highly mobile hot holes in $Cs_2AgBiBr_6$ double perovskite. *Sci. Adv.* **2021**, *7*, 1–9.

[353] Bruevich, V.; Kasaei, L.; Rangan, S.; Hijazi, H.; Zhang, Z.; Emge, T.; Andrei, E. Y.; Bartynski, R. A.; Feldman, L. C.; Podzorov, V. Intrinsic (Trap-Free) Transistors Based on Epitaxial Single-Crystal Perovskites. *Adv. Mater.* **2022**, *34*, 2205055.

[354] Hutter, E. M.; Sutton, R. J.; Chandrashekar, S.; Abdi-Jalebi, M.; Stranks, S. D.; Snaith, H. J.; Savenije, T. J. Vapour-Deposited Cesium Lead Iodide Perovskites: Microsecond Charge Carrier Lifetimes and Enhanced Photovoltaic Performance. *ACS Energy Lett.* **2017**, *2*, 1901–1908.

[355] Lai, R.; Yang, Z.; Zhi, C.; Cao, X.; Li, Z.; Di, D.; Yang, Y. Transient Suppression of Carrier Mobility Due to Hot Optical Phonons in Lead Bromide Perovskites. *J. Phys. Chem. Lett.* **2022**, *13*, 5488–5494.

[356] Milot, R. L.; Eperon, G. E.; Snaith, H. J.; Johnston, M. B.; Herz, L. M. Temperature-Dependent Charge-Carrier Dynamics in $CH_3NH_3PbI_3$ Perovskite Thin Films. *Adv. Funct. Mater.* **2015**, *25*, 6218–6227.

[357] Mannino, G.; Deretzis, I.; Smecca, E.; La Magna, A.; Alberti, A.; Ceratti, D.; Cahen, D. Temperature-Dependent Optical Band Gap in $CsPbBr_3$, $MAPbBr_3$, and $FAPbBr_3$ Single Crystals. *J. Phys. Chem. Lett.* **2020**, *11*, 2490–2496.

[358] Gadermaier, C.; Cerullo, G.; Sansone, G.; Leising, G.; Scherf, U.; Lanzani, G. Time-Resolved Charge Carrier Generation from Higher Lying Excited States in Conjugated Polymers. *Phys. Rev. Lett.* **2002**, *89*, 117402.

[359] Bakulin, A. A.; Rao, A.; Pavelyev, V. G.; Van Loosdrecht, P. H.; Pshenichnikov, M. S.; Niedzialek, D.; Cornil, J.; Beljonne, D.; Friend, R. H. The role of driving energy and delocalized states for charge separation in organic semiconductors. *Science* **2012**, *335*, 1340–1344.

[360] Tapping, P. C.; Kee, T. W. Optical Pumping of Poly(3-hexylthiophene) Singlet Excitons Induces Charge Carrier Generation. *J. Phys. Chem. Lett.* **2014**, *5*, 1040–1047.

[361] Kee, T. W. Femtosecond Pump-Push-Probe and Pump-Dump-Probe Spectroscopy of Conjugated Polymers: New Insight and Opportunities. *J. Phys. Chem. Lett.* **2014**, *5*, 3231–3240.